UNIVERSITÉ DE LILLE

ÉCOLE DOCTORALE SCIENCES POUR L'INGENIEUR – ED SPI n°72

LABORATOIRE DE GENIE CIVIL ET GEO-ENVIRONNEMENT – LGCgE ULR4515

Amélioration des propriétés du ciment par insertion des nanoparticules nano-Fe_2O_3.

Enhancing the properties of cement based materials by inserting Fe_2O_3 nanoparticles.

Thèse préparée et soutenue publiquement par

Majdouline LAANAIYA

pour obtenir le grade de

DOCTEUR en GÉNIE CIVIL de L'UNIVERSITÉ DE LILLE

Thèse soutenue le *26 Mai 2020* devant le jury composé de :

Président :	**Andrey G.KALINICHEV**, Directeur de Recherche HDR, Université de Nantes, France.
Rapporteurs :	**Anatoly BELONOSHKO**, Professeur,Royal Institute of Technology, Suède.
	Matt PROBERT, Professeur, University of York, Royaume-Uni.
Examinateurs :	**Siham KAMALI-BERNARD**, Maître de Conférences HDR, INSA-Rennes, France.
	Amine BOUIBES, Docteur Chercheur, Nagoya University, Japon.
Directeur de thèse :	**Ali ZAOUI,** Professeur, Université de Lille, France.

Acknowledgements

I would like to take the opportunity to thank all the people, without whom this thesis work would not have been completed.

I am especially indebted to my supervisor, Professor Ali ZAOUI, who made this work possible. Your precious advice and friendly guidance greatly contributed to the finalization of this work. Your spirit of dedication to research and love for science have been a great source of inspiration. Your door was always open, and I enjoyed the precious discussions that, not only helped shape my work, but most importantly, motivated me to work harder and continue to move forward in my research.

My sincere thanks go to Pr. Isam SHAHROUR for his time, generosity and constant encouragement.

I would also like to acknowledge the help of the committee members who agreed to review my thesis. Special thanks to the reporters Pr. Anatoly BELONOSHKO and Pr. Matt PROBERT for taking the time to carefully read and comment my work. Thank you all for your time and for the valuable feedbacks.

During my journey, I have been fortunate to meet excellent colleagues who have been a great help and support on many occasions, providing me with an excellent work environment. I am especially grateful to Amine, Nawal, YwanYwan, Zhu…. Thank you for the joyful moments, the little talks and the great laughs.

Special words of gratitude go to my colleagues in Polytech'Lille for the nice meetings and discussions: Thomas, Marie-Laure, Laurent, Issam, Wanqing, Bian, Romaric, Qier, Fabrice and Gilles. Thank you for making me realize what a rewarding and enjoyable profession teaching is.

My heartfelt gratitude must go to my family, to my dear parents, to my sister and my brother, for their endless love, support and inspiration. To the person who believed in me and helped me get back on my feet throughout the tough times, to my mother, Thank you for being always there for me.

Last but not least, I would like to acknowledge with gratitude the continuous support, stoic patience and understanding of my dear husband. His love and guidance are always with me in whatever I pursue.

Abstract

Nano-engineering of cement through adding nanosized particles such as nanofibers, nanotubes and nanoparticles offers a great potential for developing new generations of cement based materials with ultra-high performance, superior strength and novel functionalities for smart and durable structural materials. The hybridization of hydrated cement phases by incorporating nano-structured materials in a bottom-up approach allows the manipulation of structural features of cement at the nano-scale that ultimately affects the performance and durability properties at the macro-scale. In particular, the addition of Fe_2O_3 nanoparticles has been shown to provide cement-based materials with intrinsic self-sensing properties. The thesis presents an atomic scale study of nano-modified Calcium-Silicate-Hydrate (C-S-H), the primary binding material in cement based materials, by embedding Fe_2O_3 nanoparticles. In order to get more insights into the Portland cement main phases (alite and belite) that react with water to form C-S-H, *ab initio* calculations were performed to investigate the structural, mechanical and electronic properties along with the reactive sites of alite and belite. After examining the C-S-H structure at the atomic scale using molecular dynamics methods, Fe_2O_3 nanoparticles were inserted and the resulting hybrid material was studied. Different insertion modes of nanoparticles inside the C-S-H matrix were considered in order to elucidate how nanoparticles distribution affects the mechanical response of the hybrid composite Fe_2O_3/C-S-H. The structure with "well-dispersed" nanoparticles exhibits enhanced mechanical performance in both elastic and plastic regimes. Mechanical properties were enhanced with at least 24% increase compared to pure C-S-H. In addition, the "group effect" of inserted nanoparticles gives rise to remarkable ductility and great resistance to the crack propagation in response to tensile loading. The necking phenomenon and structural hardening were both observed in response to tensile loading, indicating a ductile failure mode of Fe_2O_3-reinforced C-S-H. Ultimately, this work reveals the striking potential of Fe_2O_3 nanoparticles for developing high performance cement-based materials with superior mechanical properties and self-sensing abilities.

Résumé

La nanotechnologie ouvre la voie au développement de nouvelles générations de matériaux cimentaires grâce à l'ajout de nanomatériaux (nanofibres, nanotubes et nanoparticules) leur conférant une haute performance et des fonctionnalités nouvelles, permettant ainsi la synthèse de matériaux de construction intelligents et durables. L'hybridation des phases du ciment hydraté par incorporation des nanomatériaux dans une approche ascendante permet la manipulation des caractéristiques structurales du ciment à l'échelle nanométrique affectant ultimement la performance et les propriétés de durabilité à l'échelle macro. En particulier, il a été démontré que l'ajout de nanoparticules Fe_2O_3 confère aux matériaux cimentaires des propriétés intrinsèques d' « auto-détection » des déformations et des contraintes mécaniques. Dans ce contexte, cette thèse présente une étude à l'échelle atomique du Silicate-Calcium-Hydraté (C-S-H), le principal agent liant du béton, nano-modifié par insertion des nanoparticules Fe_2O_3. Afin de comprendre le comportement des phases principales du ciment Portland (alite et belite) qui réagissent avec l'eau pour former le C-S-H, on s'est basé sur des méthodes du premier principe (*ab intio*) pour déterminer les propriétés structurales, mécaniques et électroniques ainsi que les sites réactifs de l'alite et de la belite. Ensuite, la structure du C-S-H a fait l'objet d'une analyse approfondie à l'échelle atomique en utilisant les techniques de la dynamique moléculaire avant de procéder à l'insertion des nanoparticules Fe_2O_3. Différents modes d'insertion de nanoparticules ont été considérés afin d'élucider l'impact de la distribution des nanoparticules sur la réponse mécanique du composite hybride Fe_2O_3 / C-S-H. La structure avec des nanoparticules «bien dispersées» présente une performance mécanique exceptionnelle dans les régimes élastique et plastique. En effet, les propriétés mécaniques ont été améliorées avec une augmentation de plus de 24% par rapport au C-S-H pur. En outre, l '«effet de groupe» des nanoparticules insérées donne lieu à une ductilité remarquable et une grande résistance à la propagation des fissures en réponse aux efforts de traction. Le phénomène de rétrécissement et du durcissement structurel ont été observés en réponse aux chargements, indiquant un mode de rupture ductile du C-S-H renforcé par les nano- Fe_2O_3. Enfin, ce travail révèle l'immense potentiel des nanoparticules Fe_2O_3 à développer des matériaux cimentaires à haute performance avec des propriétés mécaniques supérieures et des capacités de détection autonome des déformations/fissurations.

Contents

List of figures

List of Tables

General introduction

Concrete is considered as the first most used construction material and the second most consumed substance after water on earth. The annual production of cement, the binding agent of concrete, has significantly increased in the last decades with over 4 billion metric tons of cement produced worldwide in 2019 [1]. Unfortunately, cement industry accounts for 5% of global CO_2 emissions. In fact, the manufacture of every metric ton of cement releases up to 0.99t of CO_2 as a result of the calcination reaction during the manufacture of clinker, an intermediate product in the cement production process. The increasing demand on cement has trigged a great need of improving the concrete sustainability and reducing its environmental footprint. An attractive approach is to improve the concrete durability for long-lasting and sustainable concrete structures. The low tensile strength, extensive crack propagation and brittle failure are among the principle deficiencies of cement which adversely affect the durability of concrete structures. Many investigations have been conducted to improve the properties of cement/concrete in order to provide concrete structures with long durability and high sustainability benefits. Over the past few decades, incorporating industrial byproducts and mineral admixtures has provided improved properties of Portland concrete. For instance, fly ash is the most well-known industrial waste that is not only used to reduce the environmental footprint of cement production, but also to enhance the rheological properties as well as the long-term strength of concrete. Further, the high pozzolanic reactivity of fly ash helps to reduce the shrinkage cracking, and thus enhances the durability characteristics of concrete structures. However, various drawbacks of fly ash utilization in concrete formulations were reported; including slow set, low early strength and poor freeze-thaw durability. More recently, the insertion of nanoparticles in cementitious materials have proven their great ability for both accelerating the hydration reaction of cement and enhancing the short and long term strengths of concrete. Manipulating the cement material at the nano-scale is one of the most promising and effective approaches to provide concrete with ultra-high performance and enhanced durability properties. Nanotechnology is an emerging field that involves understanding, manipulating and controlling matter at the nanometer scale, providing novel functionalities and characteristics of materials. Historically, the concept of nanotechnology was theoretically introduced by the Nobel Prize winning physicist Richard Feynman during his famous lecture in 1959:"*There's Plenty of Room at the Bottom*". He pointed out that laws of physics don't hold us back from rearranging atoms in one way or

another [2]. He described an iterative process of using machines to construct smaller machines suitable for constructing even smaller machines and so on down to the molecular level, referring to the so-called "top-down" approach. In 1974, Taniguchi was the first to use the term "nanotechnology" in his paper "On the basic concept of Nano-Technology" published in *proceedings of the International Conference on Production Engineering,* to describe precise semiconductor processes such as ultra-precision film deposition and electron beam lithography, which require a characteristic tolerance on the order of few nanometers at most [3]. In the 1980s, Drexler published the first book on nanotechnology "*Engines of Creation: The Coming Era of Nanotechnology*" [4]. Drexler was the pioneer of "molecular engineering" theory by introducing the "bottom up" approach in which materials are build-up from atoms and molecules through a "self-assembly" process. Subsequently, the two main pathways have been developed in nanotechnology application fields: First, the "top-down" approach that consists on size reducing large bulk materials into nano-sized parts using advanced techniques such as precision engineering. Second, the "bottom-up" approach, that implies a controlled manipulation of the assembly of atoms/molecules using chemical and physical methods for a "molecular manufacturing" of materials and structures.

In the early 1990s, the tremendous potential of nanotechnology in influencing the construction industry has led to the emergence of many applications including understanding phenomena (hydration, damage, shrinkage…) at the nano-scale, engineering high performance building materials and developing the performance monitoring and the self-sensing capabilities of smart concrete structures.

Understanding Portland cement at the nano-scale:

The fundamental study of the major phases of cement, their hydration mechanism and the cement hydration products at the nanoscale is crucial to understand the degradation mechanism of cement in order to control the performance and enhance the structures durability at the macro-scale. The degradation of cement based materials is a complex mechanism that encompasses multiple length scales (nano→micro→macro) where every phenomenon in a given scale can be understood through looking at the scale below. The atoms positioning and the bonding mechanism at the nano-scale define the interactions inside and between cement phases at the micro-scale that characterize the material response to external mechanical loading and to chemical/physical attacks from the outside environment at the macro-scale.

Adopting a "bottom-up" view, Portland cement can be seen as a composition of many phases that react with water to form the main hydrated product: Calcium-Silicate-Hydrate (C-S-H) that is strongly responsible for the main mechanical properties of concrete. C-S-H is a nanoscale material that is still so far not well-understood considering its complex nature. Understanding the structural features of C-S-H as well as its formation mechanism at the nano-scale is necessary to develop new generations of cement with superior mechanical performance and novel smart properties such as "self-sensing" using nano-engineering techniques.

Nano-modification of cement:

Nano-engineering of cement through adding nanosized particles such as nanofibers, nanotubes and nanoparticles offers a striking potential for developing new generations of concrete with ultra-high performance, superior strength and novel functionalities for smart and durable structural materials. The hybridization of hydrated cement phases by incorporating nano-structured materials in a bottom-up approach allows the manipulation of structural features of cement at the nano-scale that ultimately affect the performance properties at the macro-scale.

Because of their unique mechanical properties, carbon nanotubes (CNTs) and carbon nanofibers (CNFs) have been studied as reinforcements of cement based matrix. Experimentally, the measured mechanical properties of CNFs and CNTs have been found to be much higher than those of steel: the elasticity modulus is about 400GPa and 1TPa for CNFs and CNTs respectively against only 200GPa for steel; and the tensile strength is approximately 7GPa and 60GPa respectively which is 20 to 150 times stronger than steel [5,6]. Consequently, CNTs/CNFs are classified among the most promising candidates to offer superior alternatives of traditional steel and fibers reinforcements of concrete. However, the high mechanical performance of CNTs/CNFs does not necessarily imply mechanically superior nanomodified cement. The strong self-attraction of CNTs/CNFs is likely to cause local agglomerations in the cement matrix which may cause dispersion problems. A number of techniques have been used to produce a good dispersion of CNTs/CNFs inside the cement matrix through special treatments with surfactants admixtures and physical blending using ultrasonic mixers. Studies on cement nanocomposites with CNTs/CNFs are quite controversial, mechanical enhancement can be observed in some cases [7] whereas no significant changes were observed in other cases [8] depending on the CNTs/CNFs content and the used treatment methods related to dispersion issues.

Nanoparticles have also shown a great potential in both enhancing concrete sustainability and producing environmentally-friendly building materials. Nanoparticles have the particularity of having a very high specific surface area SSA in the range of 10 ─1000 m^2/g depending on the nanoparticles sizes and types, and therefore offering a high potential of chemical reactivity. As a result of their high reactivity and finer scale, nanoparticles can both promote the cement hydration and optimize the cement microstructure by reducing its porosity, which enhances the strength and durability properties. The majority of studies related to the nanoparticles incorporation in cement based matrix was conducted on nano-TiO_2 (nano-titanium oxide) and nano-SiO_2 (nano-slica). Nano-SiO_2 not only improves the compressive and flexural strengths of cement based materials, but also promotes the pozzolanic reactions. Further, nano-silica was proven to be more efficient than silica fume in improving mechanical strength of cement/concrete. On the other hand, nano-TiO_2 was found to provide cement based materials with self-cleaning ability by generating the photocatalytic activity responsible for the pollutants degradation.

However, in spite of being excellent candidates for strengthening and providing cementitious materials with improved and/or novel properties, very few studies have dealt with the embedding of nano-Al_2O_3 (nano-alumina) and nano-Fe_2O_3 (nano-iron) in cement based matrix.

Self-sensing and performance monitoring:

Nanotechnology also offers the opportunity of developing smart construction materials with "self-sensing" capabilities through incorporating functional nanofillers, enabling a continuous monitoring of concrete structures performance. The functional nanofillers are distributed in the cement matrix to constitute a conductive network with a highly sensitive electric behavior to external loading or deformations. Therefore, strains, stresses and cracks can be detected through measuring the electrical indicators of the nanomodified composite. Real-time data tracking of the detected strain can then be used for making effective maintenance decisions as well as preventing the ultimate stages of structures damage, resulting in long-life service buildings/structures. The addition of Fe_2O_3 nanoparticles have been shown to provide cement based materials with intrinsic self-sensing properties due to their electrical conductivity under compressive loading. The nano-modified cement by Fe_2O_3 nanoparticles have shown a significant change in resistance ($\Delta R/R_0$) with a linear decreasing as the compressive loading increases whereas $\Delta R/R_0$ is almost unchanged in plain cement [9]. The fractional change in resistance is an indicator of self-sensing ability of the nano-

Fe_2O_3/cement composite. This indicator is 125% higher for cement mortar with 5% nano-Fe_2O_3 content against only 3% content. Moreover, a strengthening effect has been observed in modified cement mortars by nano-Fe_2O_3 due to the nanoparticles capacity to fill the pores of cement paste, improving the microstructure and thus enhancing the durability properties.

Computational materials science:

Recent advances in computational materials science were made to provide researchers with powerful tools for modeling, simulating and predicting the properties of materials at the nanoscale. Considering the enormous progress in computational technology with continuously increasing computational resources and parallel computing, one can model, test, and manipulate materials using computer simulations without having to physically synthesize the material of interest in laboratories. Atomic scale modeling through Molecular Dynamics (MD), Monte Carlo (MC) and Density Theory functional (DFT) methods provide the most powerful tools for computational materials science. Recently, atomic scale modeling methods have been intensively used to understand the C-S-H structural properties at the nano-scale such as atoms positioning, internal interactions between atoms, water molecules dynamics, hydrogen bonds network and many other structural features that cannot be obtained by empirical methods. Characterizing the structure of C-S-H at the nano-scale is not only important to predict the chemical, physical and mechanical behaviors but also to efficiently manipulate the composition of the material in order to develop new functionalities and to enhance the performance of cement based materials at the macro scale.

Thesis organization:

Given the few experimental studies on modified cement by embedding Fe_2O_3 nanoparticles, nano-iron was found to be likely efficient in both enhancing the mechanical properties of cement based materials and developing the "self-sensing" ability that is considered as an outstanding functionality for smart health monitoring of concrete structures, providing thus a new approach for maintaining sustainable concrete structures with enhanced durability performance. Nevertheless, the molecular structure and the mechanical response to external loading of modified cement by nano-Fe_2O_3 are still not well defined. Exploring the striking potential of nanotechnology bottom-up approach in characterizing the cement based materials behavior and enhancing their durability performance, we provide in the present thesis an atomic scale study of nanomodified Calcium-Silicate-Hydrate (C-S-H), the primary binding material in cement based materials, by embedding Fe_2O_3 nanoparticles. A fundamental study

of the main Portland cement phases (Alite and Belite) that react with water and form C-S-H is primarily important for a deeper understanding of the C-S-H complex structure. Then, an analysis of the structural details of C-S-H at the atomic scale must be given in order to efficiently reinforce the nanostructure by inserting Fe_2O_3 nanoparticles. Subsequently, investigations of interactions between the inserted nanoparticles and C-S-H matrix are of paramount importance for a fuller understanding of the mechanical behavior and the strengthening mechanism of the hybrid nanocomposite.

- In chapter 1, we introduce the used computational methods based on both molecular dynamics (MD) simulations and *ab initio* calculations including the main numerical schemes, approximations and calculation parameters.
- In chapter 2, we first attempt to capture the complex multi-scale morphology of the C-S-H material through existing experimental data and atomic scale models. Then, we report the main results of recent investigations from the literature on nano-modifications of cement based materials.
- Chapter 3 is an *ab initio* study of tricalcium silicate C_3S (or alite), the major phase of Portland cement. Being highly reactive, alite reacts quickly with water to form Calcium-Silicate-Hydrate (C-S-H). Further, alite is responsible for developing early age strength of hardened cement.
- In Chapter 4, we provide an *ab initio* study of dicalcium silicate C_2S (or belite) the second main phase of Portland cement, after alite. Although both alite and belite react with water to form C-S-H, belite has a much slower hydration mechanism, and hence is responsible for developing later age strength of cement.
- Chapter 5 is a molecular dynamics study of C-S-H based on an atomic "realistic model" that greatly agrees with the structural information from experimental measurements. First, we analyze the structural properties and the local coordination geometries of atoms with a view to get a fuller understanding of C-S-H composition at the nanoscale. Then, we study the mechanical response to external tensile loading in both linear and non-linear modes in order to characterize the mechanical behavior and the failure mechanism of C-S-H.
- In chapter 6, we provide an atomic scale study of the modified C-S-H by inserting Fe_2O_3 nanoparticles. Based on the adopted model of C-S-H from the previous chapter, Fe_2O_3 nanoparticles are placed in the nano-pores of the C-S-H structure. To start, we give a full description of the insertion method and the molecular dynamics simulation

details. Then, we analyze the structural properties, the bonding mechanism between Fe_2O_3 nanoparticles and C-S-H matrix and the atoms dynamics of the hybridized nanocomposite. We consider six different structures in order to study the size effect of the inserted nanoparticles on the interaction energy, the local atoms coordination in the interphase region and the mechanical properties of nano-Fe_2O_3/C-S-H composite. In the last part of this chapter, we examine the molecular evolution of the nanocomposite in response to tensile loading in order to understand the corresponding mechanical response and the fracture mechanism of nanomodifed C-S-H.

- In Chapter 7, we study the dispersion uniformity impact on the strengthening mechanism of nano-Fe_2O_3/C-S-H by considering two distribution modes of the Fe_2O_3 nanoparticles inside the C-S-H matrix. In the first part of chapter 7, we give details about the model construction describing the two distribution modes of nano-Fe_2O_3 inside C-S-H. Then, we compare the corresponding mechanical behaviors to tensile loading through analyzing the stress-strain relationship and the molecular structure evolutions in response to external loading in both elastic and plastic phases. And last but not least, we compare side to side the differences between the two considered structures in the crack initiation and propagation modes resulting in the ultimate failure.

Chapter 1: Theoretical methods

1.1. Molecular dynamics method

All things are made of atoms—little particles that move around in perpetual motion,
attracting each other when they are a little distance apart,
but repelling upon being squeezed into one another.
—Richard P. Feynman. Six Easy Pieces

1.1.1. Introduction:

Molecular dynamics is a powerful tool for providing detailed time-dependent information at the atomic level for different systems. Molecular dynamics emerged in the late 1950s in order to study a phase transition problem in a liquid using of a system of hard spheres [10,11]. Due to advances in computational capacities, MD has become an indispensable tool in simulating larger and more complex systems such as proteins, polymers, non-equilibrium and condensed matter systems with a variety of physical and chemical conditions. The computational coast of a MD simulation depends on the size of the system and complexity of the interactions between particles. Progress in computer technology allows to model systems containing up to few millions of atoms. In a MD simulation, the time evolution of a system is predicted, thus diverse properties and conformational information are extracted. Before studying the properties of a given system, an appropriate model needs to be built depending on the detail level, length and time scales we aim to explore as well as the type of properties to be studied. Developing a model with atomic details that takes into account quantum effects and the mechanisms occurring at the atomic level such as formation and breakage of bonds is a challenging task that requires great efforts and adequate computational resources. In the last 20 years, molecular dynamics has become one of the most promising tools for revealing unreachable details by experimental studies. Moreover, MD gives insights for designing new nanomaterials and nanocomposites and predicting their properties before choosing to conduct the manufacturing process.

1.1.2. Physical principle:

A classical MD simulation consists of solving the Newton's equations in order to compute the trajectories of N atoms considered as point masses. The forces acting on each atom are set by

the derivatives of a prescribed potential. The initial atomic positions are generally obtained from X-ray or NMR experimental data. Molecular modeling is alternatively used to generate the initial structural data if the experimental data are not available. The simulation boxes can have different shapes as long as they can perfectly tile into a three dimensional crystal. Normally, the cubic, rectangular prism and the truncated octahedron are the most used geometries.

1.1.3. Periodic boundary conditions:

Usually, only systems with relatively small number of atoms (in the 10^3-10^6 range) are simulated leading to the problem of surfaces effect. In addition, the behavior of a finite system is quite different from the real massive system that has "bulk properties". In order to remediate the "surface effects problem" and to simulate the bulk conditions, periodic boundary conditions (PBC) are imposed. The chosen simulation box with the atoms configuration is replicated in the three dimensions via rigid translations to form an infinite lattice. When an atom crosses the boundary of the simulation box, one of its periodic images moves in through the opposite boundary to replace it. This principle is illustrated ion Fig 1 for the case of a 2-D cubic box. In this example, the image atom is brought in the box to replace the leaving atom which corresponds to readjust the coordinate x of the leaving by subtracting the box size L if x >L (right boundary) or adding L if x<0 (left boundary).

Cut-off distance:

Using PBC, a particle not only interacts with the other particles of the main simulation box, but also with their periodic images which tremendously increases the number of the interacting pairs. To overcome this problem, a "cut-off" distance Rcut is used such as the interaction between two particles with an inter-distance exceeding the Rcut is ignored. The "minimum image criterion" consists of considering a particle i to be interacting with the closest image of a particle j and neglect the other images. This can be expressed with a Rcut smaller than half the box size: $Rcut \leq \frac{L}{2}$

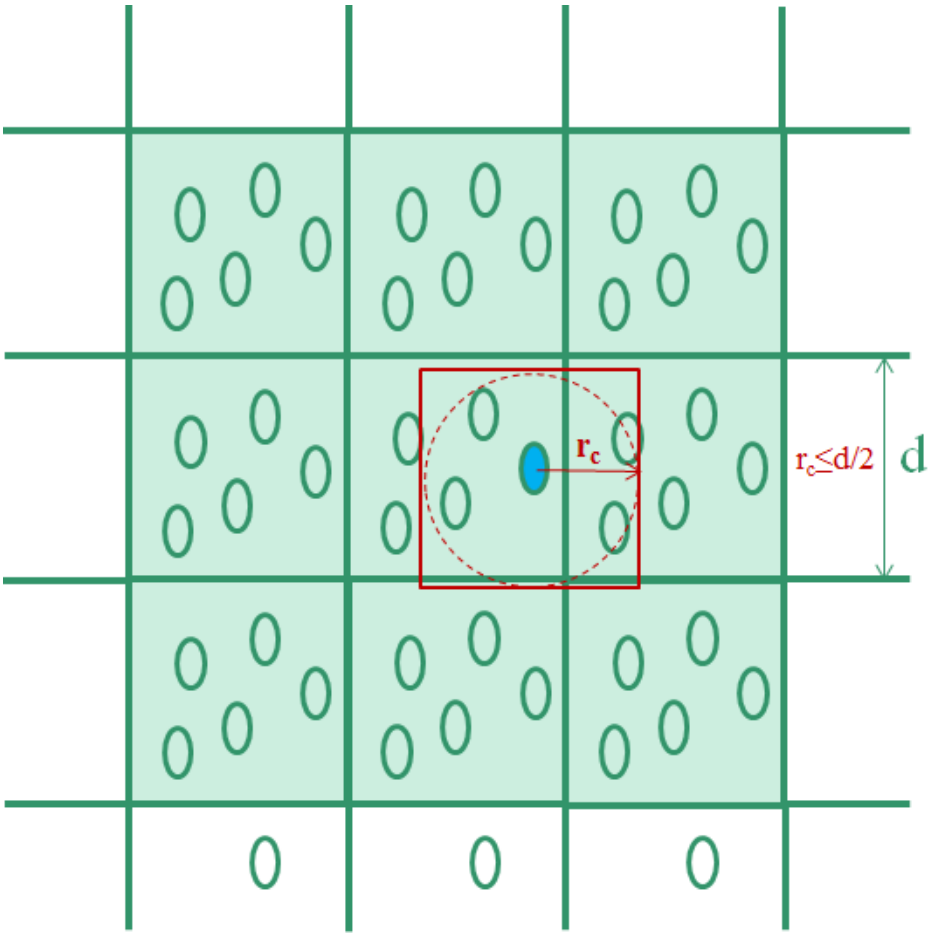

Fig.1. 1: first periodic images of the central cell. The red circle defined by the cut-off radius rcut shows the neighboring atoms that interact with the blue atom.

1.1.4. Equations of motion:

The equations of motion of N particles are written based on the well-known equations of classical mechanics:

$$m_i \frac{d^2 r_i(t)}{d^2 t} = F_i(t) \text{ , } i \in \{1,..,N\} \quad (1.1)$$

Where m_i and r_i are respectively the mass and the position vector of the particle i. F_i is the force on particle i that depends on the positions of other particles j and can be derived from the interatomic potential function $\Phi(r_{ij})$:

$$F_i(t) = -\sum_{j \neq i} \frac{\partial \Phi(r_{ij}(t))}{\partial r_{ij}(t)} \quad (1.2)$$

Where $r_{ij}(t) = |r_i(t) - r_j(t)|$.

1.1.5. Time integration:

The (1.1) second-order differential equations cannot be analytically solved for systems of more than two atoms. Several integration algorithms have been proposed consisting on stepwise solving the equations at a specific timestep and thereby calculating positions and velocities at the next timestep. The simplest and most commonly used algorithm is the Verlet algorithm [12,13]. There are a number of Verlet algorithm versions, the original Verlet algorithm is based on the Taylor expansions of positions and velocities:

$$\begin{cases} r_i(t+\Delta t) = r_i(t) + v_i(t).\Delta t + \frac{1}{2}\ddot{r}_i(t).\Delta t^2 + \frac{1}{3!}\dddot{r}_i(t).\Delta t^3 + O(\Delta t^4) & (1.3) \\ r_i(t-\Delta t) = r_i(t) - v_i(t).\Delta t + \frac{1}{2}\ddot{r}_i(t).\Delta t^2 - \frac{1}{3!}\dddot{r}_i(t).\Delta t^3 + O(\Delta t^4) & (1.4) \end{cases}$$

Adding (1.3) and (1.4) combined with (1.2) equations we get an approximation of the position of particle i at the $t + \Delta t$ timesetp from the two previous positions with a local error of the fourth order:

$$r_i(t+\Delta t) \approx 2r_i(t) - r_i(t-\Delta t) + \frac{F_i(t)}{m}\Delta t^2 \quad (1.5)$$

Similarly subtracting the two Taylor equations, we obtain the velocity at time t with a second order error:

$$v_i(t) \approx \frac{r_i(t+\Delta t) - r_i(t-\Delta t)}{2\Delta t} \quad (1.6)$$

However, equations (1.5) and (1.6) require storage of accelerations at two different time steps. Therefore, the so-called "Velocity Verlet" form avoids this problem by using the following equations:

$$r_i(t+2\Delta t) = r_i(t+\Delta t) + v_i(t+\Delta t).\Delta t + \frac{1}{2}\ddot{r}_i(t+\Delta t).\Delta t^2 + O(\Delta t^3) \quad (1.7)$$

By adding (1.7) to (1.3) we get:

$$r_i(t+2\Delta t) = r_i(t) + (v_i(t+\Delta t) + v_i(t))\Delta t + \frac{1}{2}\left(\ddot{r}_i(t) + \ddot{r}_i(t+\Delta t)\right)\Delta t^2 + O(\Delta t^3) \quad (1.8)$$

We also have:

$$v_i(t) \approx \frac{r_i(t+2\Delta t)-r_i(t)}{2\Delta t} \quad (1.9)$$

Combining (1.8), (1.9) and the motion equation of particle i we get:

$$v_i(t+\Delta t) \approx v_i(t) + \frac{F_i(t+\Delta t)+F_i(t)}{2m}.\Delta t \qquad (1.10)$$

Finally, the "velocity Verlet algorithm" uses (1.3) and (1.10) equations and is implemented as follows:

$$\begin{cases} r_i(t+\Delta t) = r_i(t) + v_i(t).\Delta t + \frac{F_i(t)}{2m_i}.\Delta t^2 \\ v_i\left(t+\frac{\Delta t}{2}\right) = v_i(t) + \frac{F_i(t)}{2m_i}.\Delta t \\ F_i(t+\Delta t) = F_i\left(r_i(t+\Delta t)\right) \\ v_i(t+\Delta t) = v_i\left(t+\frac{\Delta t}{2}\right) + \frac{F_i(t+\Delta t)}{2m_i}.\Delta t \end{cases} \quad (1.11)$$

From a known configuration at time t: ($r_i(t)$, $v_i(t)$) and deriving the force $F_i(t)$ from the prescribed potential, positions $r_i(t+\Delta t)$ are first updated by (1.3). The Force $F_i(t+\Delta t)$ is then calculated and velocity $v_i(t+\Delta t)$ is deduced from (1.10). Because of its simplicity, precision and having the advantage of minimizing the roundoff error, the velocity-verlet algorithm is preferred for time integration of the equations of motion.

The timestep magnitude should be carefully chosen. A large timestep may cause a prompt motion of a particle that "jumps" and ends up with an unphysical position leading to simulation instability. In the other hand, a very short timestep extremely slows down the simulation speed. Generally, the choice of timestep depends on the fastest motions that correspond to the weight lightest atoms.

1.1.6. Energy minimization:

Initial structures from experimental data (NMR, X-ray…) are more likely to have high energy interactions. This is mainly due to experimental artifacts or to Pauli repulsion between atoms lying too close from each other, which lead to unstable simulations. This energy excess can be relieved by minimizing the energy of the structure and therefore preventing the simulation from blowing-up. Thus, the problem is to find a system's configuration for which the derivate

of potential energy V ($r_1,\ldots r_N$) with respect to any coordinate (x,y and z) of any atom in the system is zero:

$\frac{\partial V}{\partial r_i}$=0 for r=x,y or z and i=1,…,N (1.12)

Several methods are used in order to find a local minimum of the potential energy of a system made by N atoms. Energy derivatives provide information about the energy landscape and are usually used to find a minimum. The "Steepest decent" method uses the first derivative information for minimization process. The main idea is to move along a negative gradient of a starting point downward the energy landscape Fig.1.2. The length of the step in each move is determined by a line search in the direction of the gradient. This method leads to directions that are orthogonal to each other which results in a"zig-zag" pattern towards the solution.

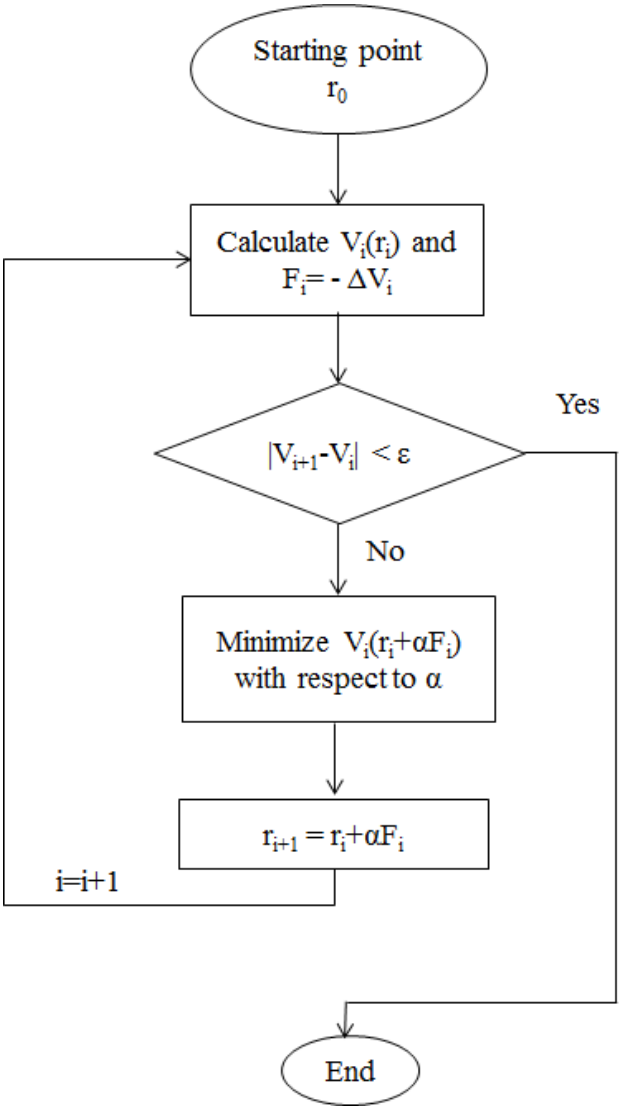

Fig. 1. 2: The steepest-descent algorithm

In some cases, the steepest-Descent method is very slow near the minimum. Another method called "the conjugate-gradient" increases the efficiency of the minimum search by controlling the new direction rather than having orthogonal successive directions. In the conjugate-gradient method, a "conjugate" direction is computed as a linear combination of the previous direction and the current gradient. Other methods can be used to minimize energy in molecular dynamics such as the Newton-Raphson technique that uses both first and second derivatives information which makes it very time-consuming compared to first-derivative minimization methods, especially for large systems.

The minimization process results in a structure with the lowest possible energy. In this configuration, no force acts on any atom and the temperature of the system is near 0 K. Therefore, no motion should be seen inside a system of a minimized structure.

1.1.7. Ensembles:

Without imposing any constraints, a MD simulation generates the (NVE) ensemble, also called the microcanonical ensemble, with a constant number of atoms N, constant box's volume V and where the energy is maintained constant as the Verlet integration of the equations of motion conserves the Hamiltonian. However, if one needs to perform a simulation at a given temperature, the desired temperature cannot be obtained with a fixed energy and with no temperature control constraints.

1.1.7.1. Constant temperature:

To reach the (NVT) ensemble or the "canonical ensemble" with fixed number of atoms, fixed volume and fixed temperature, the simulation is usually coupled with a heat bath (themostat) that imposes the desired temperature. The most popular thermostats to control temperature include the Nosé-Hoover thermostat [14], Berendsen thermostat [15], Anderson thermostat [16] and Langevin thermostat [17]. For instance, the Nosé-Hoover thermostat considers a friction force that slows down or accelerates particles until the desired temperature is reached. The equations of motion are modified as follows:

$$m_i \frac{d^2 r_i(t)}{d^2 t} = F_i(t) - \zeta(t) m_i \frac{dr_i(t)}{dt} \qquad (1.13)$$

$$\frac{d\zeta(t)}{dt} = \frac{1}{Q}\left(\sum_i m_i \frac{{v_i}^2}{2} - \frac{3N+1}{2}.k_B T_{target}\right) \qquad (1.14)$$

Where ζ is the fictitious dynamic variable whose physical meaning is friction and Q is the eligible damping parameter. Note here that $\sum_i m_i \frac{{v_i}^2}{2}$ corresponds to the kinetic energy of the system setting at the temperature T, $\frac{3N+1}{2}.k_B T_{target}$ is the average kinetic energy corresponding to the target temperature of the thermostat (3N+1 is used instead of 3N because of the added degree of freedom ζ). One can see here that the temperature is not fixed in time but tends to the target temperature value. The Nosé-Hoover thermostat is also called the extended-Lagrangian approach as it introduces an "extended" Lagrangian that adds artificial coordinates and velocities. The Nosé-Hoover conserves the extended Hamiltonian and thus the energy of the extended system.

The Nosé-Hoover thermostat is implemented by modifying the velocity Verlet algorithm equations (1.12) becoming the Nosé-Hoover-Verlet algorithm:

$$\begin{cases} \mathrm{r_i(t+\Delta t) = r_i(t) + v_i(t).\Delta t + \left(\frac{F_i(t)}{m_i} - \zeta(t)v_i(t)\right)\frac{\Delta t^2}{2}} \\ \mathrm{v_i\left(t+\frac{\Delta t}{2}\right) = v_i(t) + \left(\frac{F_i(t)}{m_i} - \zeta(t)v_i(t)\right)\frac{\Delta t}{2}} \\ \mathrm{F_i(t+\Delta t) = F_i\left(r_i(t+\Delta t)\right)} \\ \mathrm{\zeta\left(t+\frac{\Delta t}{2}\right) = \zeta(t) + \left(\sum_{i=1}^{N} m_i \frac{v_i(t)^2}{2} - \frac{3N+1}{2}k_B T_{target}\right)\frac{\Delta t}{2Q}} \\ \mathrm{v_i(t+\Delta t) = \frac{v_i\left(t+\frac{\Delta t}{2}\right) + \frac{F_i(t+\Delta t)}{2m_i}\Delta t}{1+\zeta(t+\Delta t)\frac{\Delta t}{2}}} \end{cases} \quad (1.15)$$

1.1.7.2. Constant Pressure:

In some cases, one needs to simulate a system at a constant pressure. The NPT ensemble allows keeping both temperature and pressure constant. In addition to a thermostat, a barostat in needed to control pressure by acting on volume variation. The most common techniques for controlling pressure are the simple volume rescaling, Berendsen barostat, Anderson barostat and Parrinello-Rahman barostat [18]. In the NPT ensemble, the enthalpy is the conserved quantity instead of the system's energy.

1.1.8. Force fields:

1.1.8.1. Traditional force fields:

In traditional force fields formalism, the total potential energy of a system can be decomposed into the bonding and the non-bonding interactions:

$$U = U_{bonded} + U_{non-bonded} \quad (1.16)$$

The bonded interactions, also called the intermolecular interactions, can be seen as the contribution of four terms: the bond-stretching potential U_{bond}, the angle bending potential U_{ang}, the torsional or dihedral potential U_{tors} and the improper dihedrals term U_{imp}. In the other hand, the non-bonded interactions, or intramolecular interactions include the coulombic interactions U_{coul} and Van-der-Waals interactions U_{vdw}:

$$U_{bonded} = U_{bond} + U_{val} + U_{tors} + U_{imp} \quad (1.17)$$

$$U_{non-bonded} = U_{coul} + U_{vdw} \quad (3.18)$$

Other terms can be added to the conventional force fields also called Class I force fields to form other generations of force fields. Class II and III force fields for instance contain a cross term that describes couplings between adjacent bonds, angles and dihedrals.

1.1.8.1.1. Bonded interactions:

1.1.8.1.1.1. Bond-stretching energy:

The bond stretching of two atoms is approximated as harmonic oscillator as a function of the bond length r using two parameters: the force constant k_b and the equilibrium distance r_0. The bond stretching contribution of all bonded pairs is computed as follows:

$$\boldsymbol{U_{bond} = \sum_i \frac{1}{2} k_{b,i} (r_i - r_{0,i})^2} \quad (1.19)$$

1.1.8.1.1.2. Valence angle energy:

Similarly, the angle bending contribution can be described by a harmonic approximation as a function of the valence angle θ between 3 atoms. The two needed parameters are the force constant k_θ and the equilibrium valence angle $\theta_{0:}$

$$U_{ang} = \sum_i \frac{1}{2} k_{\theta,i} (\theta_i - \theta_{0,i})^2 \quad (1.20)$$

1.1.8.1.1.3. Dihedral energy:

The torsional angle is defined by four consecutive bonded atoms i,j,k and l as the angle between the plane formed by the three atoms i,j and k and the plane through j,k and l. The torsional energy is computed as a sum of cosines with multiplicities n =1,2,3,… which indicates the number of minima as the bond is rotated through 360° , amplitudes k and reference angles ϕ^0:

$$U_{tors} = \sum_i \sum_{n=1}^{5} \frac{1}{2} k_{i,n}(1 + \cos(n\phi_i - \phi_{i,n}^0) \quad (1.21)$$

Generally, only three cosines are sufficient (n=1,2,3). For example, only 3-fold cosine (n=1) is suitable for the H-C-C-H dihedral in ethane. Other special cases require higher periodicity numbers such as ferrocene with n=5.

1.1.8.1.1.4. Improper dihedral energy:

The improper dihedral energy is also defined for a quartet of atoms i,j,k and l. The improper dihedral angle is given by three atoms j,k,l centered around a forth atom i instead of being one of the ends of the dihedral chain in the case of a proper dihedral. Improper angles are mainly used to keep planar groups such as aromatic rings or to describe the chirality of a molecule. The common functional for improper dihedral potential is a harmonic:

$$U_{imp} = \sum_i \frac{1}{2} k_{\phi,i}(\phi_i - \phi_{0,i})^2 \quad (1.22)$$

1.1.8.1.2. Non-bonded interactions:

1.1.8.1.2.1. Coulombic interaction:

Electrostatics are simply described by coulomb interactions between two point charges q_i and q_j assigned to atoms i and j respectively separated by a distance r_{ij}:

$$U_{coul} = \sum_{i>j} \frac{e^2}{4\pi\varepsilon_0} \frac{q_i q_j}{r_{ij}} \quad (1.23)$$

Where $\varepsilon_0 = 8.854 \times 10^{-12}\ C^2N^{-1}m^{-2}$ is the vacuum permittivity.

The atoms charges q_i are generally determined by fitting the electrostatic potential to quantum electron densities for atoms of the systems in their corresponding chemical environment.

The infinite coulombic sum (with periodic boundary conditions) converges very slowly and its convergence depends on the order of the summation (conditionally convergent). Some techniques such as Ewald summation [19,20] are used in order to solve this problem. Ewald method splits the total columbic energy into contributions from real space and those from

reciprocal space and transforms the (1.23) sum to summations that converge rapidly and absolutely.

1.1.8.1.2.2. Van-der-Waals interactions:

There is a large variety of functionals describing the Van-der-Waals interactions. The most commonly used is the Lennard-Jones potential, also called the 12-6 potential that accounts for the repulsive forces with a 12^{th} order term and the attractive forces with a 6^{th} order term:

$$U_{vdw} = \sum_{i>j} 4\varepsilon_{ij}\left[\left(\frac{\sigma_{ij}}{r_{ij}}\right)^{12} - \left(\frac{\sigma_{ij}}{r_{ij}}\right)^{6}\right] \quad (1.24)$$

The Lennard-Jones potential is a function of the separation r_{ij} between two non-bonding atoms parameterized with ε_{ij} the well-depth that measures the strength of the attraction between the two atoms and σ_{ij} the effective distance.

1.1.9. Limitations of traditional force fields:

1.1.9.1. Chemical environment:

An atom has a specific chemical environment that depends on both the element type and the type of surrounding bonding. Traditional force fields parameterization depends only on the atom type and does not take into account the chemical environment of the element. Therefore, it is necessary to specify different atom types for the same element type depending on its functional group. Consequently, the set of parameters of a force field rapidly grows to cover all the atom types and transforms to a large database in order to handle a multitude of systems. However, as chemical reaction occurs, a smooth transition in atom types for a given element is almost impossible. In addition, traditional force fields assume the bonds to be static. This approach presents a severe limitation since it cannot simulate chemical reactions as it corresponds to bond breaking and forming. Thus, traditional force fields are only suitable for cases where atoms don't undergo a chemical reaction and cannot model reactive systems.

1.1.9.2. Polarization:

Traditional force fields are based on the assumption of fixed atomic charges and hence cannot account for polarization effects. Polarizable force fields were developed in order to model the charge transfer in a given system. The most commonly used approaches to achieve polarization are: induced-point dipoles [21], Drude oscillators [22] and charge fluctuation method (Qeq) [23]. The induced-point dipoles consider induced dipole moments at each

polarizable site. The dipole strength is proportional to the local force field. It also creates an electric field and a polarization between the induced dipoles. The drude oscillator method consists on introducing auxiliary massless "drude" particles carrying partial charges connected to the original atoms in the systems "Cores" via a harmonic spring. The electronic charge on the drude particle and the rigidity of the spring characterize the atom's response to a local electrostatic field. Then, the Core-Drude pair creates an oscillating dipole. Finally, the "Qeq" model is the only method that considers variable charges on atoms changing based on the electronegativity equalization principle that give rise to different charge distributions depending on the chemical environment. Although polarizable force fields have attracted much attention due to their accuracy and enhanced transferability compared to traditional force fields, it requires considerable efforts because of the additional parameters. Deriving a large set of accurate parameters and their non-linear interdependencies is a challenging task that faces the development and implementation of polarizable force fields.

1.1.10. Reactive Force fields:

Reactive force fields were specifically developed to overcome the inherent limitations of traditional force fields. A large variety of potentials with the concept of bond orders have been proposed with a dynamic description of bonds based on the local environment of each atom. The most common reactive force fields include the Brenner Reactive Empirical Bond Order (REBO) potential [24] , REBO2 potential [25] , the Adaptive Intermolecular Reactive Emperical Bond Order (AIREBO) potential [26] and REAXFF [27].

ReaxFF is the first reactive force field containing both dynamic bonds and polarization effects. ReaxFF was initially developed by Adri van Duin in 2001 [28] with the core features of a parameterized bond order surface together with a variable charge distribution based on a self-consistent charge equilibration method. This first version was only made for hydrocarbons and was later on extended to include more effects such as the London dispersion and to simulate a variety of other systems.

1.1.10.1. ReaxFF formalism:

In the current REAXFF version by K. Chenoweth et al. (2008) [29], the total energy of a system is the contributions of 14 energy terms:

$$E_{system} = E_{bond} + E_{val} + E_{tors} + E_{vdw} + E_{coul} + E_{over} + E_{under} + E_{h-bond} + E_{lp} + E_{pen} + E_{C2} + E_{triple} + E_{coa} + E_{conj} \quad (1.25)$$

Where the first five terms $E_{bond}, E_{val}, E_{tors}, E_{vdw}$ and E_{coul} have the same meaning as in traditional force fields but with different expressions as it will be discussed in the following section. In contrast with traditional fields, the ReaxFF formalism takes into account overcoordination $E_{over}$and undercoordination E_{under}, hydrogen bonding E_{h-bond} and lone pair contributionE_{lp}. The corrections $E_{pen}, E_{coa}, E_{C2}, E_{triple}$ and E_{conj} are only used for some specific systems. The penalty energy $E_{pen}$is used for allenes stabilization, E_{C2} for behavior correction of C2-molecules, E_{triple} for the triple bond energy correction in carbon monoxide while E_{coa} and E_{conj} are used for capturing the conjugated bonds effects.

1.1.10.2. bond orders:

All the mentioned bonded energy contributions (besides the coulombic and Van-der-Waals interactions) essentially depend on the concept of bond order. Bond order between two atoms refers to the strength of the bonding between them and is computed in terms of the atoms types and the separating distance. The total bond order between two atoms i and j is the summation of contributions of σ-bonds, π-bonds and the double-π-bonds:

$$BO'_{ij} = BO^{\sigma'}_{ij} + BO^{\pi'}_{ij} + BO^{\pi\pi'}_{ij} \quad (1.26)$$

Where each bond order is an exponential function of the distance r_{ij} with three adjustable parameters :

$$\begin{cases} BO^{\sigma'}_{ij} = exp\left(p_{bo1}\left(\frac{r_{ij}}{r^{\sigma}_{0}}\right)^{p_{bo2}}\right) \\ BO^{\pi'}_{ij} = exp\left(p_{bo3}\left(\frac{r_{ij}}{r^{\pi}_{0}}\right)^{p_{bo4}}\right) \\ BO^{\pi\pi'}_{ij} = exp\left(p_{bo4}\left(\frac{r_{ij}}{r^{\pi\pi}_{0}}\right)^{p_{bo5}}\right) \end{cases} \quad (1.27)$$

The bond order of each type is a decreasing function for all values of internuclear distances r_{ij} with $BO^{\alpha'}_{ij}$ in the [0; 1] interval for α=σ, π and ππ.

BO'_{ij} $BO'_{ij}, BO^{\sigma'}_{ij}, BO^{\pi'}_{ij}$and $BO^{\pi\pi'}_{ij}$ are the uncorrected bond order terms since they only account for pair-wise bond order coordination. This suggests necessary corrections in order to account for the total coordination and lone pairs. These corrections are introduced using Eq. (1.28):

$$\begin{cases} BO_{ij}^{\sigma} = BO_{ij}^{\sigma\prime}.f_1(\Delta_i',\Delta_j').f_4(\Delta_i',BO_{ij}').f_5(\Delta_j',BO_{ij}') \\ BO_{ij}^{\pi} = BO_{ij}^{\pi\prime}.f_1(\Delta_i',\Delta_j').f_1(\Delta_i',\Delta_j').f_4(\Delta_i'^{boc},BO_{ij}').f_5(\Delta_j'^{boc},BO_{ij}') \\ BO_{ij}^{\pi\pi} = BO_{ij}^{\pi\pi\prime}.f_1(\Delta_i',\Delta_j').f_1(\Delta_i',\Delta_j').f_4(\Delta_i'^{boc},BO_{ij}').f_5(\Delta_j'^{boc},BO_{ij}') \\ BO_{ij} = BO_{ij}^{\sigma} + BO_{ij}^{\pi} + BO_{ij}^{\pi\pi} \end{cases} \quad (1.28)$$

Overcoordination Δ_i' stands for the difference between the total bond orders around atom i and the number of its bonding electrons Val_i. The second overcoordination $\Delta_i'^{boc}$ is used to soften the correction for atoms bearing lone electrons:

$$\begin{cases} \Delta_i' = -Val_i + \sum_{j=1}^{Neighbors(i)} BO_{ij}' \\ \Delta_i'^{boc} = -Val_i^{boc} + \sum_{j=1}^{Neighbors(i)} BO_{ij}' \end{cases} \quad (1.29)$$

$f_1(\Delta_i',\Delta_j')$ is used for the overcoordination correction while $f_4(\Delta_i'^{boc},BO_{ij}')$ together with $f_5(\Delta_j'^{boc},BO_{ij}')$ account for lone-pairs as follows:

$$\begin{cases} f_1(\Delta_i',\Delta_j') = \frac{1}{2}\left(\frac{Val_i+f_2(\Delta_i',\Delta_j')}{Val_i+f_2(\Delta_i',\Delta_j')+f_3(\Delta_i',\Delta_j')} + \frac{Val_j+f_2(\Delta_i',\Delta_j')}{Val_j+f_2(\Delta_i',\Delta_j')+f_3(\Delta_i',\Delta_j')}\right) \\ Where \quad f_2(\Delta_i',\Delta_j') = \exp(-p_{bo1}.\Delta_i') + \exp(-p_{bo1}.\Delta_j') \\ and \quad f_3(\Delta_i',\Delta_j') = -\frac{1}{p_{bo2}} ln\left(\frac{1}{2}\left(\exp(-p_{bo2}.\Delta_i') + \exp(-p_{bo2}.\Delta_j')\right)\right) \end{cases} \quad (1.30)$$

And:

$$\begin{cases} f_4(\Delta_j'^{boc},BO_{ij}') = \frac{1}{1+\exp\left[-p_{bo3}.\left(p_{bo4}.\left(BO_{ij}'\right)^2-\Delta_i'^{boc}\right)+p_{bo5}\right]} \\ f_5(\Delta_j'^{boc},BO_{ij}') = \frac{1}{1+\exp\left[-p_{bo3}.\left(p_{bo4}.\left(BO_{ij}'\right)^2-\Delta_j'^{boc}\right)+p_{bo5}\right]} \end{cases} \quad (1.31)$$

Then, we can define the corrected overcoordination Δ_i from the corrected bon order:

$$\Delta_i = -Val_i + \sum_{j=1}^{Neighbors(i)} BO_{ij} \quad (1.32)$$

Positive values of Δ_i stands for overcoordinated atoms while negative values are related to undercoordinated atoms.

Now that bond orders are defined, we will describe each interaction type mentioned in Eq. (3.25) and give their energy expressions.

1.1.10.3. Bond energy:

The three bond types (σ, π and double-π) contribute to the bond energy as follows:

$$E_{bond} = -D_e^{\sigma}.BO_{ij}^{\sigma}.exp\left[p_{be1}(1-(BO_{ij}^{p_{be2}})\right] - D_e^{\pi}.BO_{ij}^{\pi} - D_e^{\pi\pi}.BO_{ij}^{\pi\pi} \quad (1.33)$$

As the bond order decays for large internuclear separationr_{ij}, the three energy contributions tend to zero. The σ-bond type energy contribution has an additional exponential term that decays with the σ-bond order. The (1.33) expression meets the condition of a smoothly decaying energy as the bond breaks.

Unlike traditional force field, REAXFF rigorously distinguishes between every bond type contribution. The complexity of REAXFF lies in the number of the adjustable parameters: twelve parameters per bond in REAXFF compared to only two parameters per bond in traditional force fields.

1.1.10.4. Lone-pair energy:

This energy contribution accounts for unpaired electrons, which is not taken into account by traditional force fields. E_{lp} is important for describing atoms with defective bonds. First, equation (3.34) is used for determining the number of lone pairs $n_{lp,i}$around an atom i:

$$n_{lp,i} = int\left(\frac{\Delta_i}{2}\right) + exp\left[-p_{lp1}\left(2+\Delta_i - 2.int\left(\frac{\Delta_i}{2}\right)\right)^2\right] \quad (1.34)$$

Then, we calculate Δ_i^{lp} the deviation of the number of lone pairs from the optimal number of lone pairs (e.g. 2 for oxygen). Δ_i^{lp}corresponds to the number of unpaired electrons:

$$\Delta_i^{lp} = n_{lp,opt} - n_{lp,i} \quad (1.35)$$

Lone pair energy is calculated using the (1.36) equation:

$$E_{lp} = \frac{p_{lp2}.\Delta_i^{lp}}{1+\exp\left(-75.\Delta_i^{lp}\right)} \quad (1.36)$$

1.1.10.5. Overcoordination energy:

The correction in bond order expressions are not sufficient to take into account all the overcoordinations in the system. We add energy penalty terms of overcoordinated atoms as follows:

$$E_{over} = \Delta_i^{lp,corr} \cdot \frac{\sum_{j=1}^{nbond(i)} p_{ovun1}.D_e^{\sigma}.BO_{ij}}{\left(\Delta_i^{lp,corr}+val_i\right)\left(1+\exp\left(p_{ovun2}.\Delta_i^{lp,corr}\right)\right)} \quad (1.37)$$

The corrected overcoordination $\Delta_i^{lp,corr}$ is calculated using the following equation:

$$\Delta_i^{lp,corr} = \Delta_i - \frac{\Delta_i^{lp}}{1+p_{ovun3}.\exp\left[p_{ovun4}\left(\sum_{j=1}^{neigbors(i)}\left(\Delta_j-\Delta_j^{lp}\right)(BO_{ij}^{\pi}+BO_{ij}^{\pi\pi})\right]\right.} \quad (1.38)$$

1.1.10.6. Undercoordination energy:

Undercoordination energy accounts for the resonance of the π-electron between π-bonded atoms i and j:

$$E_{under} = -p_{ovun5}.\frac{1-exp\left(p_{ovun6}.\Delta_i^{lp,corr}\right)}{1+exp\left(-p_{ovun2}.\Delta_i^{lp,corr}\right)}.\frac{1}{1+p_{ovun7}.exp\left[p_{ovun8}.\left[\sum_{j=1}^{neigbors(i)}\left(\Delta_j-\Delta_j^{lp}\right)(BO_{ij}^{\pi}+BO_{ij}^{\pi\pi})\right]\right]}$$

(1.39)

Undercoordination energy contribution is only important if atoms i and j are undercoordinated and the bond between the two atoms partly has a π-bond character.

1.1.10.7. Valence angle energy:

The valence energy contribution is calculated using equation (3.40):

$$E_{val} = p_{val1}.f_7\left(BO_{ij}\right).f_7\left(BO_{jk}\right).f_8\left(\Delta_j\right).\left[1-\exp\left(-p_{val2}\left(\Theta_0(BO)-\Theta_{ijk}\right)^2\right)\right] \quad (1.40)$$

$p_{val1}$is a parameter that defines the depth while p_{val2} is a width-controlling parameter.

Expressions of functions f_7 and f_8 are given by:

$$\begin{cases} f_7\left(BO_{ij}\right) = 1-exp\left(-p_{val3}\left(BO_{ij}\right)^{pval4}\right) \\ f_8\left(\Delta_j\right) = p_{val5} - \frac{(p_{val5}-1).\left(2+\exp\left(p_{val6}.\Delta_j^{boc}\right)\right)}{1+\exp\left(p_{val6}.\Delta_j^{boc}\right)+\exp\left(-p_{val7}.\Delta_j^{boc}\right)} \end{cases} \quad (1.41)$$

The terms introduced by function f_7 allows the valence angle energy to decay as one of the bonds i-j or j-k dissociates. Also, for large deviations of angle Θ_{ijk} from equilibrium angleΘ_0, the valence angle energy goes to zero.

The equilibrium angle $\Theta_0$is calculated depending on the coordination of the involved atoms:

$$\Theta_0(BO) = \pi - \Theta_{0,0}.\left(1 - \exp\left(-p_{val10}.(2 + SBO2)\right)\right) \quad (1.42)$$

Where $\Theta_{0,0}$ is an adjustable parameter .The functional SBO2 is defined from the sum of π-bonds (SBO) around the central atom j as follows:

$$\begin{cases} SBO2 = 0 & if \quad SBO \leq 0 \\ SBO2 = (SBO)^{p_{val9}} & if \quad 0 < SBO \leq 1 \\ SBO2 = 2 - (2 - SBO)^{p_{val9}} & if \quad 1 < SBO \leq 2 \\ SBO2 = 2 & if \quad SBO > 2 \end{cases} \quad (1.43)$$

And :

$$SBO = \sum_{n=1}^{neighbors(j)}\left(BO_{jn}^{\pi} + BO_{jn}^{\pi\pi}\right) + \left[1 - \prod_{n=1}^{neighbors(i)} exp\left(-BO_{jn}{}^{8}\right)\right].\left(-\Delta_j^{boc} - pval8.nlp,j\right) \quad (1.44)$$

p_{val8}, p_{val9} and $p_{val10}$are general adjustable parameters. We can see that SBO includes the effects of π-bonds and double-π-bonds to calculate the equilibrium angle. Effects of overcoordination/undercoordination and lone electrons pairs of the central atom are also included by the equation (1.44).

The stability of three-body structures with a central atom having two double bonds (e.g. allene) requires an additional energy penalty E_{pen}. Moreover, the three body conjugation correction E_{coa} can be added in order to describe the stability of conjugated systems

1.1.10.8. Torsion angle energy:

The energy contribution from a torsional angle ω_{ijkl} formed by a quadruplet of atoms i,j,k and l can be expressed by equation (1.45):

$$E_{tors} = f_{10}\left(BO_{ij}, BO_{jk}, BO_{kl}\right).\sin\Theta_{ijk}.\sin\Theta_{jkl}.\left[\frac{1}{2}V_1.(1 + \cos\omega_{ijkl}) + \frac{1}{2}V_2.(1 - \cos2\omega ijkl).expptor1BOjk\pi - 1 + f11\Delta j,\Delta k2 + 12V3.(1 + \cos3\omega ijkl)\right. \quad (1.45)$$

Where:

$$\begin{cases} f_{10}\left(BO_{ij}, BO_{jk}, BO_{kl}\right) = \left(1 - exp\left(-p_{tor2}.BO_{ij}\right)\right)\left(1 - exp\left(-p_{tor2}.BO_{jk}\right)\right)\left(1 - exp\left(-p_{tor2}.BO_{kl}\right)\right) \\ f_{11}\left(\Delta_j, \Delta_k\right) = \frac{2 + exp\left(-p_{tor3}\left(\Delta_j^{boc} + \Delta_k^{boc}\right)\right)}{1 + exp\left(-p_{tor3}\left(\Delta_j^{boc} + \Delta_k^{boc}\right)\right) + exp\left(p_{tor4}\left(\Delta_j^{boc} + \Delta_k^{boc}\right)\right)} \end{cases}$$

(1.46)

The parameters V_1, V_2 and V_3 have the same meaning as for traditional force fields.

The $f_{10}(BO_{ij}, BO_{jk}, BO_{kl})$ term ensures that the torsion energy vanishes as one of the bonds dissociates. The terms $\sin\Theta_{ijk}$ and $\sin\Theta_{jkl}$ indicate that if one of the valence angles approaches π, the torsion energy goes to zero. The term $f_{11}(\Delta_j, \Delta_k)$ accounts for the overcoordination of atoms j while the π-bonds effects are included in the exponential term in equation (3.45).

A Four-body conjugation term E_{conj} has to be added to describe the conjugations effects of some systems (e.g. benzene and aromatic rings).

1.1.10.9. Hydrogen bond energy:

The energy associated with a hydrogen bond in a X-H─Z is expressed by:

$$E_{h-bond} = p_{hb1} \sin^8\left(\frac{\Theta_{XHZ}}{2}\right).\left(1 - exp(p_{hb2}.BO_{XH})\right).exp\left(p_{hb3}.\left(\frac{r_{hb}^0}{r_{HZ}} + \frac{r_{HZ}}{r_{hb}^0} - 2\right)\right) \quad (1.47)$$

The strong hydrogen bonding is accomplished when all three atoms X, H and Z are aligned as the term $\sin^8\left(\frac{\Theta_{XHZ}}{2}\right)$ is maximized for $\Theta_{XHZ} = \pi$.

1.1.10.10. Non-bonded interactions:

The non-bonded interactions include the repulsive interactions at short distances due to Pauli principle and attractive interactions at long distances due to dispersion. These interactions are described by Van-der-Waals and Coulomb forces respectively, and are calculated for every atom pair in the system.

1.1.10.10.1. Taper functional:

ReaxFF uses a Taper correction to avoid energy discontinuities and singularities of the first order derivative of the potential at the cutoff boundary R_{cut}. The non-bonded energy terms (E_{vdw} and E_{coul}) are multiplied by a 7th order polynomial taper function defined as follows:

$$Tap(r_{ij}) = 20.\left(\frac{r_{ij}}{R_{cut}}\right)^7 - 70.\left(\frac{r_{ij}}{R_{cut}}\right)^6 + 84.\left(\frac{r_{ij}}{R_{cut}}\right)^5 - 35.\left(\frac{r_{ij}}{R_{cut}}\right)^4 + 1 \quad (1.48)$$

1.1.10.10.2. Van-der-Waals interactions:

ReaxFF uses a Morse potential for Van-der-Waals interactions:

$$E_{vdw} = Tap(r_{ij}).D_{ij}\left[exp\left(\alpha_{ij}\left(1-\frac{f_{13}(r_{ij})}{r_{vdw}}\right)\right)-2exp\left(\frac{1}{2}\alpha_{ij}\left(1-\frac{f_{13}(r_{ij})}{r_{vdw}}\right)\right)\right] \quad (1.49)$$

Where D_{ij} , α_{ij} and r_{vdw}as pair-wise adjustable parameters.

The function f_{13} accounts for a shielded interaction using a shielding factor γ_{vdw}. This prevents excessive high repulsions between bonded atoms and atoms forming a valence angle. The expression of f_{13} is given by:

$$f_{13}(r_{ij}) = \left[r_{ij}^{pvdw1} + \left(\frac{1}{\gamma_{vdw}}\right)^{pvdw1}\right]^{\frac{1}{pvdw1}} \quad (1.50)$$

It is important to note here that the van-der-waals interactions are computed not only for the non-bonded pairs as it is the case for traditional force fields, but for all atom pairs (bonded and non-bonded). Bonded atoms are included in order to avoid discontinuities on the potential energy surface when bonds form or dissociate.

1.1.10.10.3. Coulomb interactions:

As for the Van-der-Waals interactions, Taper and shielding terms are also included in the energy expression of the coulomb interactions:

$$E_{coul} = C.Tap(r_{ij}).\frac{q_i.q_j}{\left(r_{ij}{}^3+\gamma_{ij}^{-3}\right)^{\frac{1}{3}}} \quad (1.51)$$

The shielding pair-wise parameter γ_{ij} is the geometric mean of the shielding parameters of the two atoms. It avoids excessively high repulsion between charges that are too close from each other.

1.1.10.10.4. Charge equilibration:

In contrast to traditional force field, partial charges q_i are dynamic and need to be updated at every timestep. The q_i charges are calculated with a self-consistent scheme based on the charge equilibration Qeq approach by Rappe and Goddard [23]. The Qeq problem is to find the charges that minimize the electrostatic energy $E(q_1,\dots,q_N)$ of the system with the constraint of a constant system's net charge $q_{net,}$ which can be formulated as follows:

$$\begin{cases} Minimize\ \ E(q_1,\dots,q_N) = \sum_{i=1}^{N}\left(E_{i0}+\chi_i^0.q_i+\frac{1}{2}J_{ii}^0q_i^2\right)+\sum_{i<j}J_{ij}q_iq_j \\ with\ q_{net} = \sum_{i=1}^{N}q_i \end{cases} \quad (1.52)$$

Where E_{i0} is the energy of an isolated neutral atom i. χ_i^0 and J_{ii}^0 are respectively the electronegativity and the idempotential (or self-coulomb) of atom i, both are calculated from experimental data (Ionization potential IP and electron affinity EA). Jij is the Coulombic interaction between unit charges on atoms i and j.

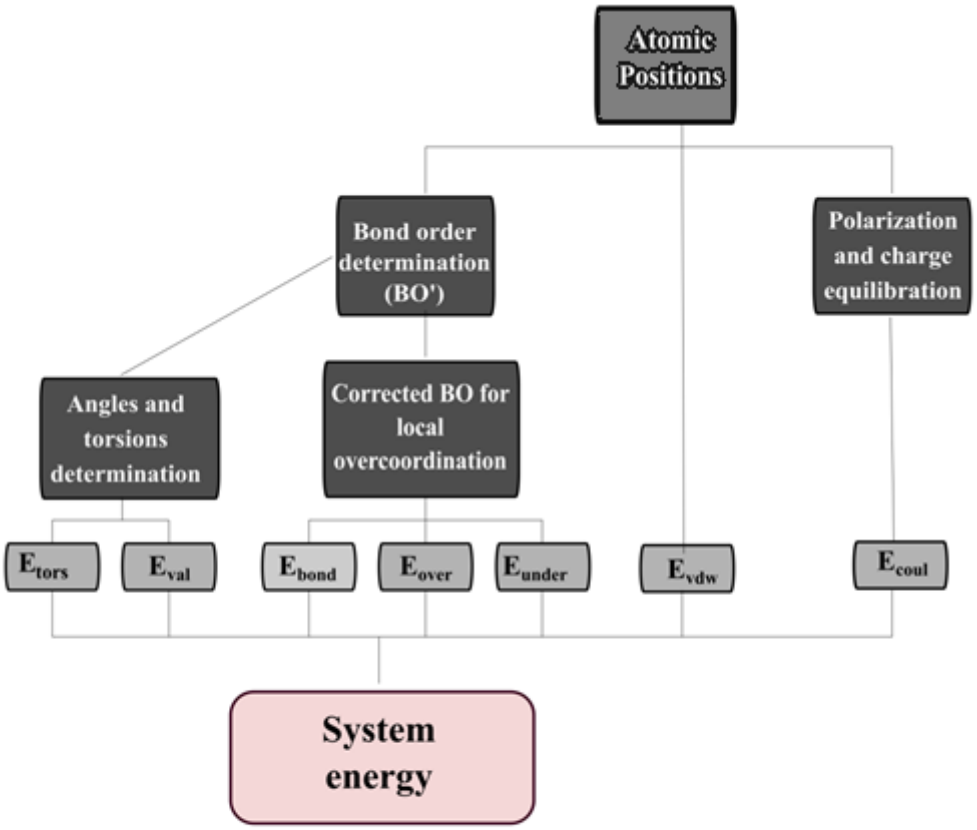

Fig.1. 3 : ReaxFF flow diagram.

Finally, after defining the initial structure and the interactions between atoms, we can run a MD simulation in order to calculate the properties of interest. Fig.1.4 shows the main steps of a MD run.

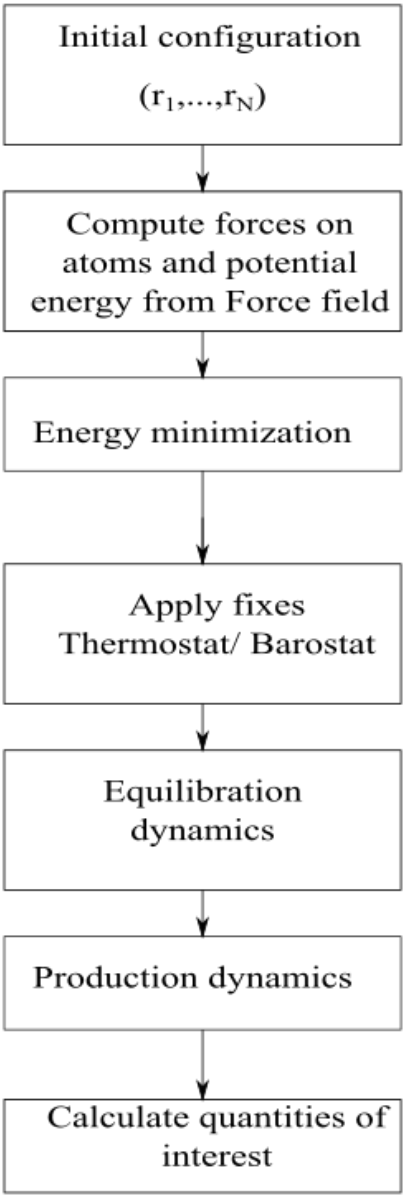

Fig.1. 4 : MD flow-chart

1.2. Density Functional Theory

Density functional theory (DFT) is considered as one of the most popular and efficient methods in computational physics/ chemistry to perform ground-state electronic-structure calculations of many-body systems such as molecules and solids. DFT bases its formalism on the central idea that any ground-state property of a system is fully determined by the electronic charge density n(r).

1.2.1. The many-body problem:

We consider a N-electron system on the Born-Oppenheimer approximation. Using Dirac notations, the stationary electronic states are determined by the time-independent Schrödinger equation:

$\hat{H}|\Psi\rangle = E|\Psi\rangle$ (1.53)

Ψ is a N-electrons antisymmetric wave function, E is the associated energy and $\hat{H}$ is the Hamiltonian that can be written as a contribution of the kinetic energy operator $\hat{T}$, the electron-electron interactions operator $\hat{U}_{e-e}$ and the nuclei-electron interactions $\hat{V}_{n-e}$:

$\hat{H} = \hat{T} + \hat{U}_{e-e} + \hat{V}_{n-e}$ (1.54)

The expressions of operators $\hat{T}$, $\hat{U}_{e-e}$ and $\hat{V}_{n-e}$ can be found elsewhere in the literature [30].

Many techniques have been developed for solving the Schrodinger equation such as the Configuration Interactions (CI) methods and diagrammatic perturbation theory. However, the use of these approaches is not efficient in most real cases and the determination of full many-body wave functions remains simply impossible for systems with more than few electrons.

The DFT offers an alternative approach by only considering the electronic density n(r) that is a function of only 3 variables which is a tremendous simplification compared to the multi-electronic wave function depending on at least 3N variables (ignoring spin). The ground state density n (r) determines all other observables and provides a complete knowledge about the many-body problem. By exploring this idea, DFT has proved its high efficiency in predicting a large set of molecular properties: structural properties vibrational frequencies, reaction paths, electric and magnetic properties, ionization and atomization energies….). In the last

decades, DFT was developed to study complex systems such as spin polarized systems, superconductors with electronic pairing mechanisms, excited states, etc. The development of DFT was rewarded by the Nobel Prize in Chemistry in 1998 attributed to Walter Kohn, the founding father of DFT.

1.2.2. The Hohenberg-Kohn (H-K) theorem:

Considering a system of N interacting electrons in an arbitrary external local potential $V_{ext}(r)$ (instead of the nuclei-interaction potential $V_{n-e}(r)$), the ground-state total energy of the system can be written as a unique functional of the ground-state electronic density n(r). Then, the external potential determines the ground-state density.

The 1st Hohenberg-Kohn theorem:

In 1964, Hohenberg and Kohn [31] proved that the inverse statement is also true: *the external potential is a unique functional to within a constant of the ground-state density n(r).*

In other words, the ground state density n(r) determines the potential V_{ext} (r) (to within a constant), that in turn fixes the Hamiltonian and therefore all the other properties of the system. The wave function is also a functional of the ground-state density, written as Ψ[n], and can be used to define the universal density functional (independent from the external potential):

$$F[n] = \langle \Psi[n] | \hat{T} + \hat{U}_{e-e} | \Psi[n] \rangle \quad (1.55)$$

The ground-state energy of the electronic system in the external potential V_{ext} is also a unique functional of ground-state density n, and can be written using F[n]:

$$E[n] = F[n] + \int V_{ext}(r) n(r) dr \quad (1.56)$$

The 2nd Hohenberg-Kohn theorem:

Hohenberg and Kohn also showed that E[n] satisfies a variational property: *the true ground-state energy E_0 is obtained by minimizing its functional with respect to electronic density n*. The global minimum is reached for the exact ground-state density $n_0(r)$:

$$E_0 = \min_n\{F[n] + \int V_{ext}(r)n(r)dr\} = E[n_0] \quad (1.57)$$

In sum, *the Hohenberg-Kohn theorem* is based on three main items: The existence of a one-to-one relation between the ground-state density and the local external potential, the definition of the universal density functional and finally, the variational principle of the energy functional with respect to the ground-state density.

1.2.3. The Kohn-Sham method:

One year later, Kohn and Sham provided in 1965 [32] a practical approach to use the H-K theorem by introducing an auxiliary fictitious system of non-interacting electrons, with the same ground-state density as the real interacting system. Kohn and Sham proposed a decomposition of the universal density functional F[n] as follows:

$$F[n] = T_{NI}[n] + E_{Hxc}[n] \quad (1.58)$$

$T_{NI}[n]$ in the non-interacting kinetic energy functional defined as:

$$T_{NI}[n] = \langle \Phi[n]|\hat{T}|\Phi[n]\rangle \quad (1.59)$$

Where Φ[n] is the KS wave function, defined as the minimizing single-determinant wave function for a given density n. The KS wave function Φ is constructed from a set of N orthonormal occupied spin-orbitals defined as products of spin functions and spatial orbitals $\{\phi_i(r)\}_{i=1,\dots,N}$.in terms of which electronic density is expressed:

$$n(r) = \sum_{i=1}^{N}|\phi_i(r)|^2 \quad (1.60)$$

E_{Hxc} is the Hartree-exchange-correlation functional, is written as :

$$E_{Hxc}[n] = E_H[n] + E_{xc}[n] \quad (1.61)$$

Where the Hartree energy functional $E_H[n]$, represents the electrostatic repulsion for the charge density n(r), and is expressed by:

$$E_H[n] = \frac{1}{2}\iint \frac{n(r)n(r')}{|r-r'|} dr dr' \quad (1.62)$$

$E_{xc}[n]$ is the exchange-correlation energy functional which is the unknown functional so far.

Based on the previous expression, the energy functional can be written as:

$$E[n] = T_{NI}[n] + E_H[n] + E_{xc}[n] + \int V_{ext}(r)n(r)dr \quad (1.63)$$

The Kohn –Sham equations:

Applying the variational principle, the density of the interacting many-body system in external potential V_{ext} can be determined by solving the KS equations of non-interacting single-body auxiliary system in effective potential V_{eff}^{KS} :

$$\left[-\frac{1}{2}\nabla^2 + V_{eff}^{KS}\right]\phi_i(r) = \varepsilon_i\phi_i(r) \quad (1.64)$$

Where the KS effective V_{eff}^{KS} :

$$V_{eff}^{KS}(r) = V_{ext}(r) + V_H(r) + V_{xc}(r) \quad (1.65)$$

Where $V_H(r) = \frac{\delta E_H[n]}{\delta n(r)} = \int \frac{n(r')}{|r-r'|} dr'$ is the Hartree potential and $V_{xc}(r) = \frac{\delta E_{xc}[n]}{\delta n(r)}$ is the exchange-correlation potential.

By self-consistently solving the KS equations, the ground –state density n(r) is obtained from eq. (1.60) and thus the ground-state electronic total energy can be determined.

With the KS formalism, the knowledge of the exact form of the exchange-correlation functional E_{xc} would lead to the exact ground-state electronic energy. However, no general explicit analytical form of E_{xc} is known. One can only search for reasonable approximations. In the next sections, we will present the most commonly used approximations for the exchange-correlation functional.

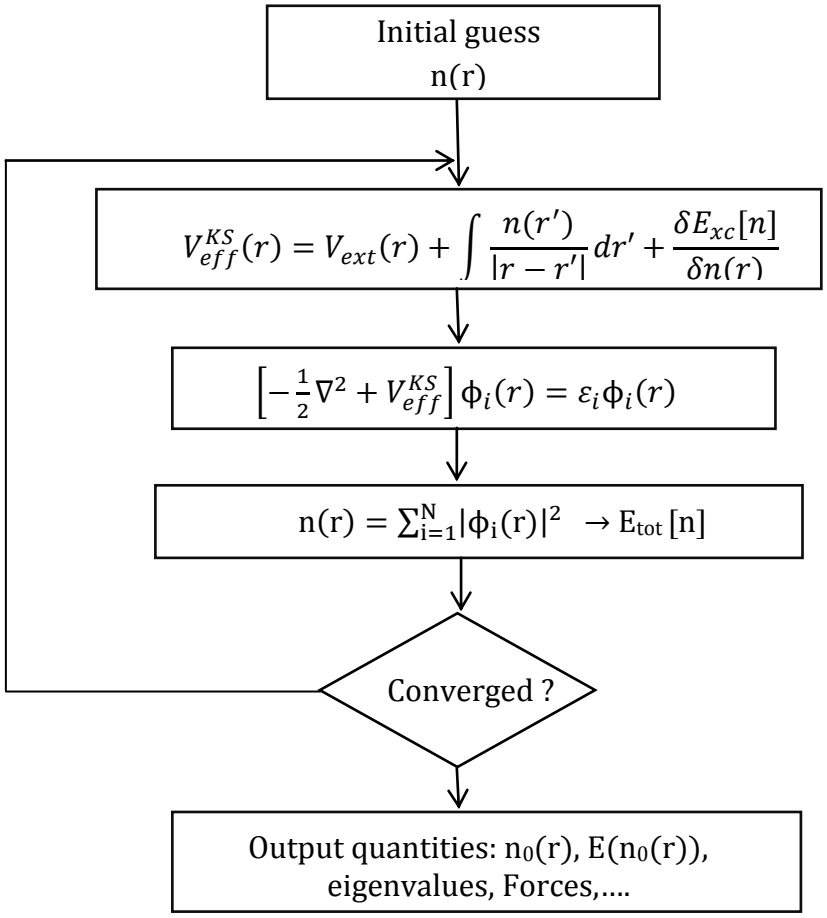

Fig.1. 5 : Self-consistent scheme to solve the Kohn-Sham equations.

1.2.4. The Local Density Approximation (LDA):

Historically, the Local Density Approximation (LDA), introduced by Kohn and Sham, represents the basis of all exchange-correlation functional approximations.

LDA approximates $\varepsilon_{xc}\big(n(r)\big)$ the exchange correlation energy per particle of a system at a given point of density n(r) by the exchange correlation energy per particle of the uniform electron gas of the same density $\varepsilon_{xc}^{unif}(n(r))$:

$$E_{xc}^{LDA}[n] = \int n(r)\, \varepsilon_{xc}^{unif}\big(n(r)\big) dr \quad (1.66)$$

The uniform gas represents a system of interacting electrons with a uniform density n. The uniform exchange correlation energy per particle is split into the exchange and correlation contributions:

$$\varepsilon_{xc}^{unif}\big(n(r)\big) = \varepsilon_{x}^{unif}\big(n(r)\big) + \varepsilon_{c}^{unif}\big(n(r)\big) \quad (1.67)$$

The analytical expression of the exchange energy per unit particle of the uniform gas electron $\varepsilon_{x}^{unif}(n)$ is known:

$$\varepsilon_{x}^{unif}(n) = -\frac{3}{4}\left(\frac{3n}{\pi}\right)^{\frac{1}{3}} \quad (1.68)$$

The correlation energy per unit particle of the uniform gas electron $\varepsilon_{c}^{unif}(n)$ cannot determined analytically, but can be numerically obtained using Quantum Monte Carlo calculations [33] and by fitting to a parameterized function of n satisfying the high-density and low-density expansions [34]. The most used parameterizations are the (VNW) [35] and the PW92 [36] .

By definition, the LDA approximation should be adopted for slowly varying density systems, the experience however, has proved that LDA works unexpectedly well for situations where electronic density is not a slowly varying function. This can be explained by some systematic (not accidental) errors cancellation by summing up the underestimated correlation energy and the overestimated exchange energy.

1.2.5. The Generalized Gradient Approximation (GGA):

Besides the local approximation, non-local forms of the exchange-correlation functional have been proposed. The Generalized Gradient Approximation (GGA) attempts to capture both local and semi-local information about the electronic density variation by including the density gradient $\nabla n(r)$ as an additional variable in the exchange-coordination functional expression:

$$E_{xc}^{GGA}[n] = \int f\big(n(r), \nabla n(r)\big) d^3r \quad (1.69)$$

A number of construction methods of the function $f\big(n(r), \nabla n(r)\big)$ have been employed and different GGAs have been generated. The Perdew-Wang 91 (PW91) [37-39] and Perdew-Borke-Ernzerhof (PBE) [40] are some of the most used and most reliable GGAs in physics. A discussion of the performance of some selected forms of GGA can be found here [41].

1.2.6. The Pseudo-Potential approach:

For larger systems, typically solids, the pseudopotential (PP) approach has become a widely used approach in DFT. The PP is based on the key observation that chemical bounding is mainly due to valence (outer) electrons while the core (inner) electrons are chemically inert and retain an atomic-like configuration (within a good approximation) . The core electrons are taken into account by replacing the external potential V_{ext} by a pseudopotential V_{ext}^{PP}whereas the Hartree and exchange-correlation terms in the KS equations are only evaluated for the valence density $n_v(r)$. Therefore, the effective potential eq. (1.65) in KS equations becomes:

$$V_{eff}^{PP}[n_v] = V_{ext}^{PP} + V_H(n_v) + V_{xc}(n_v) \qquad (1.70)$$

In order to construct a "suitable pseudopotential" for a given atom, one must specify the core orbitals and the valence orbitals as the cut-off radius r_c that separates the core region and the valence region. Then, the pseudo-wave functions $\psi^{pp}(r)$ must meet the following requirements:

- Each pseudo-wavefunctions must be identical to the corresponding real wavefunctions from the all-electrons (AE) calculations outside the cut-odd radius:

$$\psi^{pp}(r) = \psi^{AE}(r)\,, \quad r>r_c$$

- The eigenvalues must also be conserved:

$$\varepsilon_i^{PP} = \varepsilon_i^{AE}$$

- At the cutoff, the first and second derivatives of each pseudo-wavefunction must be equal to that of the corresponding all-electron wavefunction at the cut-off radius. This ensures a continuous and smooth transition of the pseudo-wavefunctions from the core region to the valence region.
- There must be no radial nodes in the core region.

Early forms of pseudopotentials obey to the additional "norm-conserving" condition [42]: The integral of the charge density below the cutoff must be equal to that of AE calculations. However, this restriction forces the wavefunctions to vary rapidly, which requires a large set of planewaves and thus a high computational cost. To solve this problem, the "norm-conserving" constraint was relaxed leading to a new generation of pseudopotentials known as "soft" and "ulta-soft" pseudopotentials, proposed by Vanderbilt [43].

More information about the relationships that must exist between real potentials and pseudo-potentials were formalized by Blöchl [44] resulting in the projector augmented-wave pseudopotentials. A schematic representation of a pseudo-wavefunction against the corresponding all-electon wavefunction is shown in Fig.1.6.

Hence, pseudopotentials are constructed as a function that represents the true all-electron potential in the valence region of the atoms but varies smoothly in the core region. The rapid oscillations of the wavefunctions in the core electrons are therefore eliminated by the pseudopotential formalism and the extremely large plane-wave basis set to describe the core states is no longer required. By reducing the number of electrons treated explicitly, the pseudo-potential approach offers the possibility of performing DFT calculations on systems of ten to thousands of electrons with the lowest computational cost.

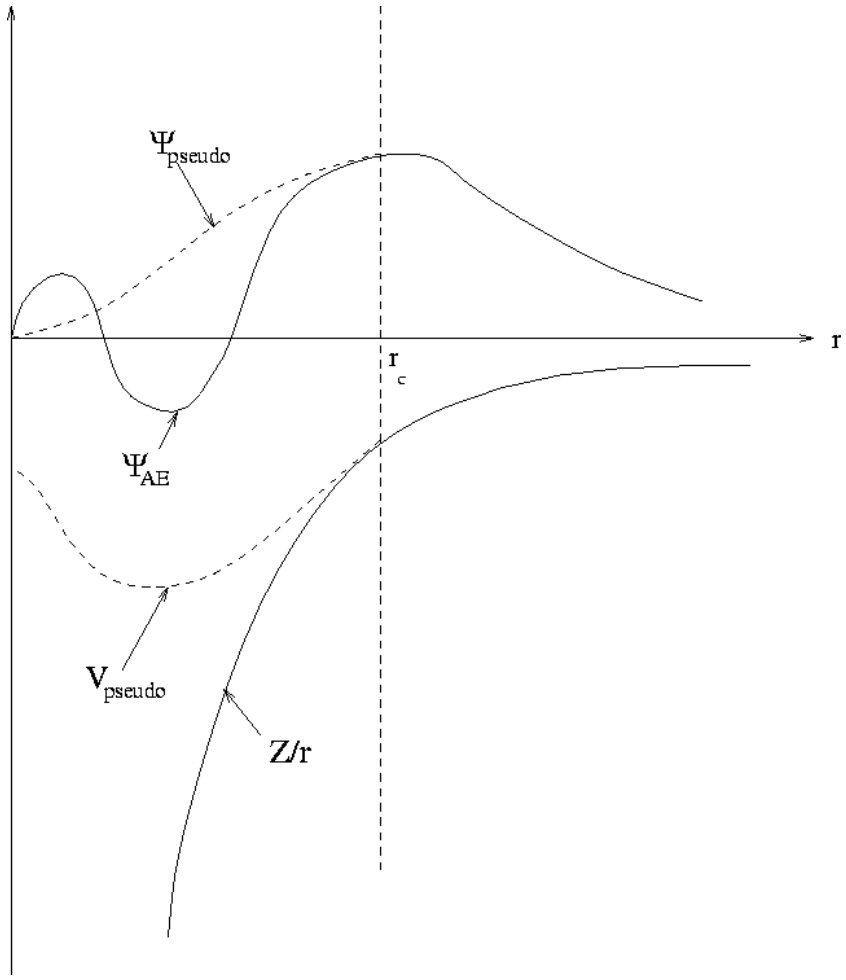

Fig.1. 6 **:** The pseudo wavefunction and pseudo electronic potential (dashed lines) against the corresponding all-electronic wavefunction and full potential (solid lines). From **http://cmt.dur.ac.uk/sjc/thesis/thesis/node20.html**

Chapter 2: Materials of study

2.1. Cement composition:

2.1.1. Portland cement:

To produce cement, silica, lime aluminum oxide and iron oxide are mixed in rotary kilns with a temperature of about 1500°C. The materials are sintered, partially melted and the clinker particles are consequently produced with few centimeters size and almost a spherical shape. Clinker particles are then cooled down and ground into fine particles of an average diameter of 20µm called Portland cement. As the cooling process is relatively fast, the crystallization is not complete and the phases of Portland cement retain some features of amorphous materials. The four major phases of Portland cement are:

- ✓ Tricalcium silicates: Or alite C_3S (3CaO. SiO_2) with 50-70% cement content.
- ✓ Dicalcium silicates: Or belite C_2S (2CaO. SiO_2) with 15-30% cement content
- ✓ Tricalcium aluminates: C_3A (3CaO. Al_2O_3) with 5-10% cement content.
- ✓ Tetracalcium aluminum ferrites: C_4AF ($4CaO.Al_2O_3.Fe_2O_3$) with 5-15% cement content.

In cement notations, C refers to CaO, S to SiO_2, F to Fe_2O_3, $\bar{S}$ to SO_3 and H to H_2O. Dashes in the formula for C-S-H emphasize its variable composition.

2.1.2. Hydration of cement:

The four phases of cement react with water in a process called cement hydration. Hydration of the silicates C_3S (alite) and C_2S (belite) leads to the formation of the main cement hydrations products: calcium-Silicate-Hydrate (C-S-H) and Calcium Hydroxide (CH) with a significantly higher hydration rate in the case of C_3S. The corresponding hydration reactions are given by [45]:

$2C_3S+10.6H \rightarrow C_{3.4}S_2H_8 + 1.3CH$ (2.1)

$2C_2S+8.6H \rightarrow C_{3.4}S_2H_8 + 0.6CH$ (2.2)

The aluminate phase C_3A produces calcium aluminates according to the following set of reactions:

$2C_3A+27H \rightarrow C_4AH_{19}+C_2AH_8$ (2.3)

$2C_3A+21H \rightarrow C_4AH_{13}+C_2AH_8$ (2.4)

$2C_3A+CH+12H \rightarrow C_4AH_{13}$ (2.5)

In the presence of Sulfates ions SO_4^{2-} and water, C_3A produces ettringite :

$C_3A+3C\bar{S}H_2+26H \rightarrow C_6A\bar{S}_3H_{32}$ (2.6)

Once the sulfate ions are all consumed, C_3A hydration continues in the presence of ettringite and water and produces monosulfoaluminates:

$2C_3A+ C_6A\bar{S}_3H_{32} + 4H \rightarrow 3C_4A\bar{S}_3H_{12}$ (2.7)

The hydration of the ferrite phase C_4AF still the least well understood [46]. Many hydration products forms were reported [47-49].

The resulting hardened cement paste from the cement hydration is a mixture of the hydration products of the four main phases of the Portland cement, some residues of unhydrated cement particles and the water present in the pores. C-S-H is the main cement paste constituent, it occupies 60-70% of the solid volume in hardened cement paste with particles dimension of 10 – 100 nm. Calcium hydroxide mineral also named portlandite is the second dominant cement paste component with 10-20% volume fraction. Crystal sizes of portlandite range in 10 – 100 µm depending on many factors such as hydration time, temperature and the impurities content. Finally, calcium aluminates, monosulfoaluminate hydrates, ettringite and calcium ferrites are the minor components of hardened cement with about 15% volume ratio [50].

2.2. Calcium Silicate Hydrates C-S-H:

2.2.1. Microstructure of C-S-H:

C-S-H is the principal hydration product of Portland cement. Representing the major binding phase in cement-based materials, C-S-H is responsible for the overall strength and mechanical performance. The structure and composition of C-S-H is not well defined and exists in different forms [45]. The chemical formula $C_{3.4}S_2H_8$ in the hydration equations of Alite and belite is only approximated. C-S-H is qualified as a poorly crystalline structure. The microstructure of C-S-H is characterized by its colloidal nature and gel-like morphology due to the nanometer size pores in C-S-H. Powers et al. [51] attributed this gel-like colloidal feature of the C-S-H microstructure by investigating the water sorption and pore volume of C-

S-H. Other works were carried on in order to describe the microstructure and the porosity of C-S-H [52,53].

2.2.2. Low density and High density C-S-H:

Based on surface area measurements by nitrogen sorption, Tennis and Jennings [54] distinguished between two types of C-S-H: a high density (HD) C-S-H and a Low density (LD) C-S-H. Some of the LD C-S-H pores were accessible to nitrogen, and none were accessible to nitrogen in HD C-S-H (See Fig.2.1). The Jennings colloid model [55] developed in order to explain the structure of the two types of C-S-H. Colloidal Particles (globules) of C-S-H agglomerate around to different patterns: tightly packed particles of HD CSH into which nitrogen cannot penetrate and less densely packed particles of LD C-S-H around which nitrogen can partially penetrate (See Fig.2.2). Small-angle Neutron scattering (SANS) observations also support the concept of two different morphologies of C-S-H in ordinary Portland cement [57]. The volumetric proportion of the two C-S-H types can be determined depending on the water to cement ratio (w/c). Results of the optimized model [54] obtained by maximizing the statistical fit gives values of LD and HD C-S-H dry densities : $\rho_{LD}^{dry} = 1440\ Kg/m^3$ and : $\rho_{HD}^{dry} = 1750\ Kg/m^3$ and saturated densities $\rho_{LD}^{sat} = 1930\ Kg/m^3$ and : $\rho_{HD}^{sat} = 2130\ Kg/m^3$ [11].

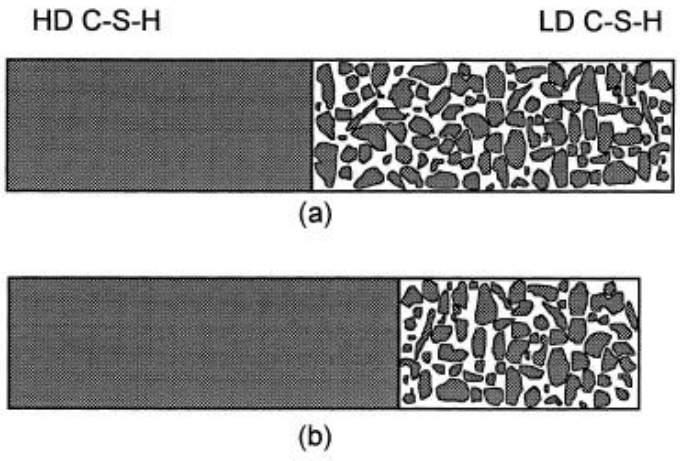

Fig.2. 1: Left regions represent HD C-S-H, right regions represent LD C-S-H for: (a) water to cement ratio (w/c) of 0.5. (b) Water to cement ratio (w/c) of 0.35. From [54]

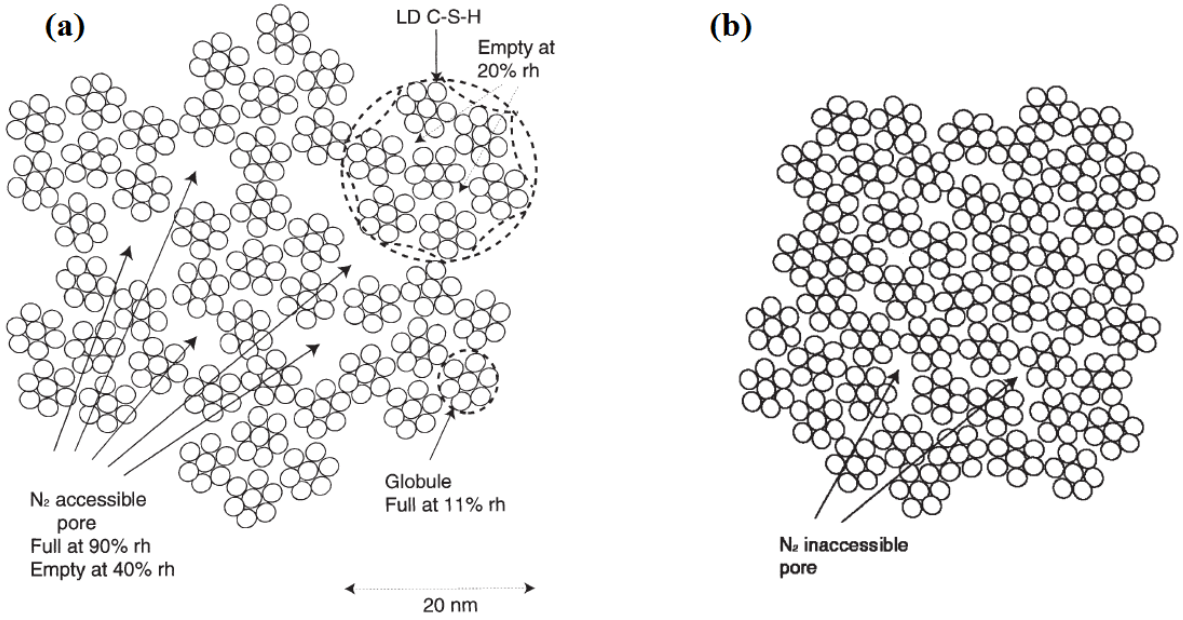

Fig.2. 2: Schematic representation of: (a) LD C-S-H type during the late stage of cement hydration. (b) HD C-S-H type during the late stage of cement hydration. Adapted from [57]

2.2.3. Nanostructure of C-S-H:

The complexity of the C-S-H structure has attracted the interest of many researchers who tried to characterize the nanostructure of C-S-H. A large number of models have been proposed [57-65].Taylor suggests that C-S-H is built up of imperfect jennite and 14Å Tobermorite layers modified by many silicate tetrahedra omissions [63]. The structure of 14Å tobermorite was determined by Bonaccorsi et al. [64]. Results show that 14Å tobermorite ($Ca_5Si_6O_{16}(OH)_27H_2O$) is a layered structure. Each tobermorite layer can be described in terms a combination of a main layer and an interlayer with an overall thickness of 1.4nm. The main layer part has a central Ca-O sheet of empirical composition CaO_2 connected on both sides to silicate chains kinked with a periodicity of three tertrahedra (“dreierketten” chains). All oxygen atoms of the central part are shared with the chains. Silicate chains that belong to adjacent layers do not form double chains but are offset from one another with an interlayer space that consists of water molecules and Ca^{2+} ions. Jennite also has a layered structure with a chemical formula of ($Ca_9Si_6O_{18}(OH)_68H_2O$) [65] but with a higher C/S ratio of 1.5 than that of 14Å tobermorite (about 0.83). Jennite layers have a similar structure than tobermorite with a “sandwich” like structure of the main layer and combined layer thickness of 1.05nm.

However, only half of the oxygen atoms of the central part are shared with the silica chains in Jennite while the other half are part of the –OH groups.

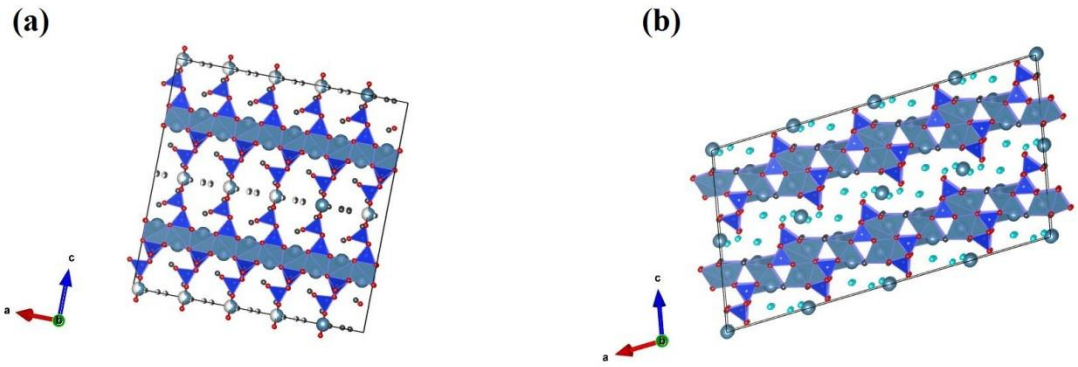

Fig.2. 3 : Bonaccorsi et al. model of tobermorite [64] viewed along (0 1 0). (b) Bonaccorsi et al. model of Jennite [65] viewed along (0 1 0).

2.2.4. Structural properties of C-S-H in the experiment:

Nevertheless, the structural features and properties of a developed model must be consistent with the experiment. Experimental studies using small-angle neutron scattering (SANS) technique have found a C/S ratio of about 1.7 [66]. This value cannot be obtained either by Tobermorite (C/S=0.83) or Jennite (C/S=1.5). Taylor and Howison suggested that the C/S ratio can be raised by removing some bridging terahedra and replacing them with Ca^{2+} ions [67]. Adopting this mechanism, many dreirekette-based models have consequently been proposed built up from Tobermorite-Jennite like structures (T/J), or from tobermorite-like structure intermixed with layers of calcium hydroxide (T/CSH) [68]. Furthermore, experimental information on the nature of silica chains connectivity in Calcium-Silciate-Hydrates are given by 29Si nuclear magnetic resonance (NMR) spectropy by determining the Qn factors denoting for the fractional chemical shift of a tetrahedraly coordinated Si atom with n bridging oxygen atoms. NMR results show three major peaks corresponding to Q_0 sites Q_1 and Q_2 [69]. Q_0 account for silicate monomers, Q_1 Silicon sites correspond to pairs of linked Silicate tetrahera (dimers) or a silicon tetrahedron at the end of a silicate chain and Q_2 sites account for the silicate tetrahedron at the middle of a chain. More highly polymerized (Q_3 or Q_4) silicate tetrahedrons were not observed. A NMR study by Brough and Brodson [70] of the hydration mechanism of C_3S (Alite Ca_3SiO_5) showed that Q_1 species, essentially dimers, represent the main products of the early stages hydration whereas Q2 are increasingly

produced as the hydration proceeded and the average chain length given by $\mu = \frac{2(Q1+Q2)}{Q1}$ consequently increases. Polymerization was observed to occur in later stages of the hydration reaction. Based on the observed data, a potential polymerization mechanism was proposed suggesting silicate dimers to connect together by monomers and form pentamer and then octomer (dimer → pentamer → Octomer).

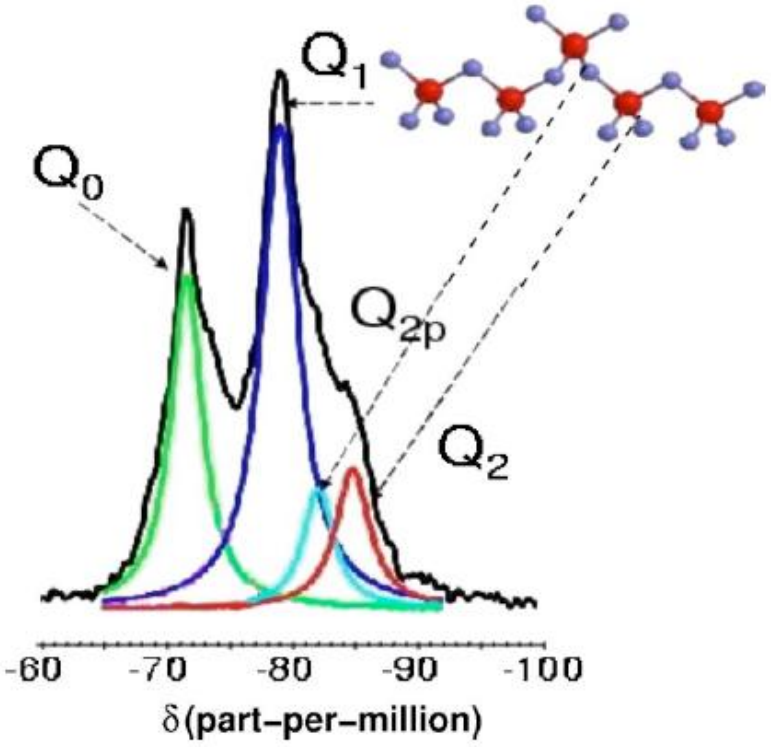

Fig.2. 4 : NMR spectra of C-S-H sample, δ is the chemical shift in ppm, from [69].

2.2.5. C-S-H realistic model:

Recently, a breakthrough in the molecular modeling of C-S-H was the "realistic model" proposed by Pellenq et al. [71] that is consistent with data given by the experiment. The model was built up from a dry 11 Å tobermorite ($Ca_6Si_6O_{16}$) and a starting C/S ratio of 1.0. Guided by the NMR results (Q_0=10%, Q_1=67% and Q_2=23%) and SANS measurement of C/S ratio, Pellenq et al. removed some neutral SiO_2 groups from the silica chains and a defective Tobermorite structure is generated with Qn fraction of Q0=13%, Q1=67% and Q_2=20% and

C/S=1.65. The obtained structure was then relaxed using the Core-shell model at 0 K. Water adsorption was afterwards performed using Grand Canonical Monte Carlo (GCMC) simulation. Results showed a similar amount of adsorbed water to that of the 14Å tobermorite interlayers .A final structure with a chemical formula of $(CaO)_{1.65}$ $(SiO_2)(H_2O)_{1.75}$ was subsequently generated. The density of the relaxed structure at zero temperature and zero pressure is about 2.45 g/cm^3 which is very close to the value found the experiment :2.6g/cm3 [72]. The calculated structural and mechanical properties of the Pellenq et al. model show great agreement with the experiment studies on C-S-H.

Bauchy et al. work [73] based on the Pellenq realistic model used the reactive REAXFF potential [74] to account for reactions occurring between the interlayer water and the defective calcium-silicate chains in the intralayer. This process allow some water molecules to dissociate into –OH groups. The structural analysis of the obtained model suggests an intermediate structure between a crystal-like and a glass-like structure. The structure is qualified as “not fully crystalline” and “not completely amorphous”. The crystal order manifests by the layered feature of the calcium-silicate chains, whereas the glass disorder is related to the spatial distribution of water molecules and hydroxyl groups in the interlayer region. This work gives more insight into the Crystal/amorphous feature for a better understanding of the complexity of the C-S-H structure.

2.2.6. Multiscale morphology of C-S-H:

To characterize the C-S-H structure, it is important to determine the morphological characteristics across multiple length scales. Fig.2.5 is a schematic of the construction elements of C-S-H at the nano and micro scales.

At the atomic scale, the solid phase of C-S-H is composed by defective layers of Calcium-Silica chains and interlayer space that represents the nanoporosity of C-S-H.

At the level above, on a 10^{-10}-10^{-9}m length scale order, the layers of the C-S-H nanostructure constitute a colloidal particle or a “globule” of approximately 2.8 nm size.

On a 10^{-8}-10^{-6} m length scale order, the colloidal particles agglomerate in two different ways to form two forms of CSH: the high density C-S-H and the low density C-S-H that differ simply in the packing density and gel porosity while the “globule” building block is the same. This level is the smallest length scale accessible by mechanical testing.

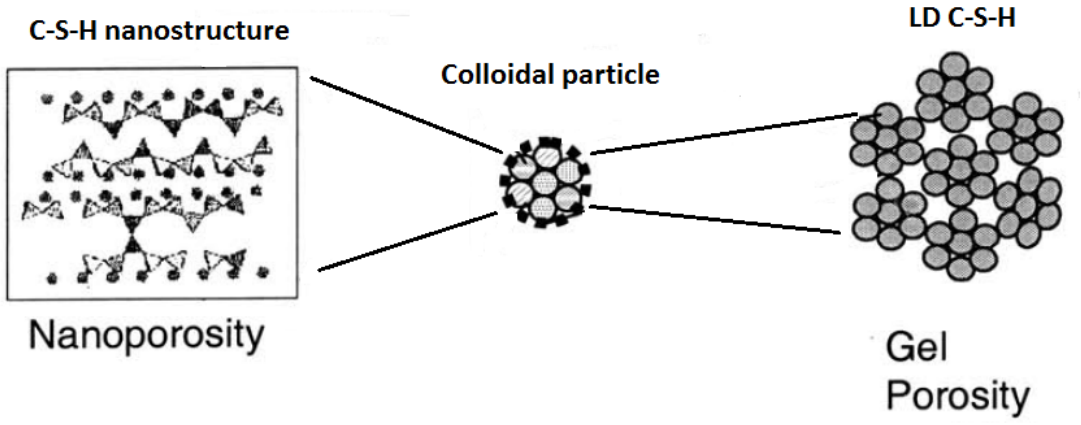

Fig.2. 5: C-S-H at different length scales. Adapted from [75]

From C-S-H to Concrete: a multiscale approach

Starting from the C-S-H in its two forms, we can identify four levels of the concrete microstructure. Fig.2.6 illustrates the four-level microstructure of concrete [76].

Level 1: Two types of C-S-H with different morphologies: LD and HD C-S-H (10^{-8}-10^{-6} m scale order).

Level 2: C-S-H together with portlandite (CH) large crystals, hydrated cement particles and micropores constitute the concrete microstructure at the 10^{-4}-10^{-3}m length scale.

Level 3: On a 10^{-3}-10^{-1} m length scale order, we find mortar made of the cement paste matrix, sand particle inclusions and an interfacial transition zone (ITZ).

Level 4: the 10^{-1}-10 m length scale refers to concrete, which is a composition of mortar matrix, aggregate and an ITZ.

It is worth noting that the chemical attacks and the degradation mechanism occur primarily at very small length scales (level 1 and below). Therefore, an upscale analysis is very valuable for a better understanding of basic properties, behavior and phenomena in cement.

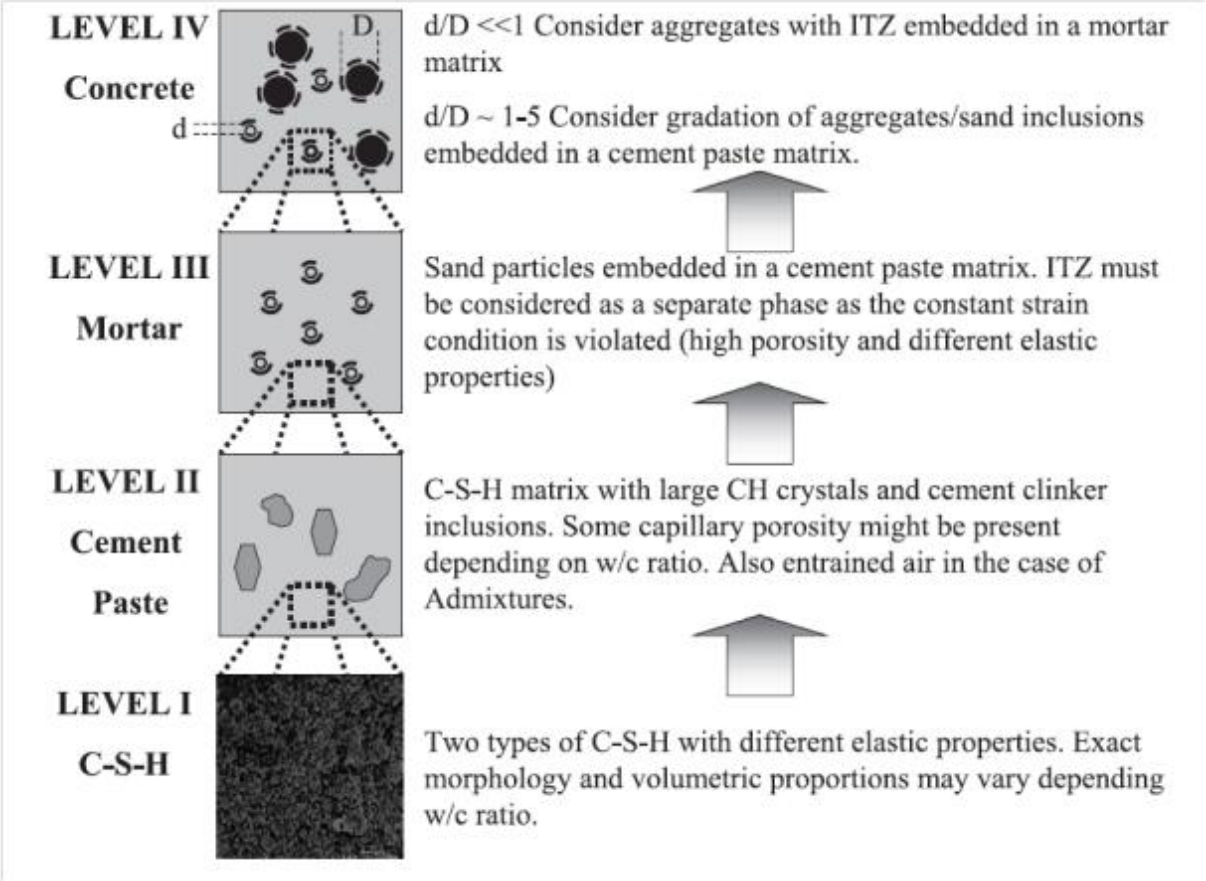

Fig.2. 6: Multiscale approach of the concrete microstructure. From [76].

2.3. Nanomodification of cement:

Nanotechnology is a fast-growing field that promises a crucial progress in cement and concrete technology by providing the ability of nano-engineering and controlling the materials at the nano-scale. Nano-modification of cement consists of manipulating the structure of cement phases by introducing new nanosized additives according to a bottom-up approach. Compared to the bulk materials, they manifest several superior properties in conductivity, catalysis, electronic conductivity, magnetism, optical absorption, stress sensing, and mechanical strength. In the construction sector, the incorporation of nanomaterials is expected to provide the building materials with new functionalities such as self-cleaning, self-heating and energy-saving [77,78]. The addition of nanomaterials (nanoparticles, nanobinders, nanotubes,nanofibers, nano-springs, nano-rods…) promises a high improvement of the mechanical behavior of concrete by acting as fillers and by preventing the crack propagation [79,80].

2.3.1. Nanotubes/nanofibers:

Carbon nanotubes/nanofibers (CNTs/CNFs) are excellent candidates for high performance cement. Two main types of CNTs can be identified: The single-walled Carbon nanotubes (SWCNTs) that consist of one single graphene cylinder and the multi-Walled Carbon nanotubes (MSWCNTs) that have concentric and coaxial graphene cylinders. The chirality of SWNTs is defined with a couple of integers (n,m) such that $n > 0$ and $m \geq 0$; in particular, the pairs (*n*,0) define the "zigzag" configuration of CNTs while the (n,n) pairs are called the "armchair" type of CNTs as shown in Fig. 2.7.

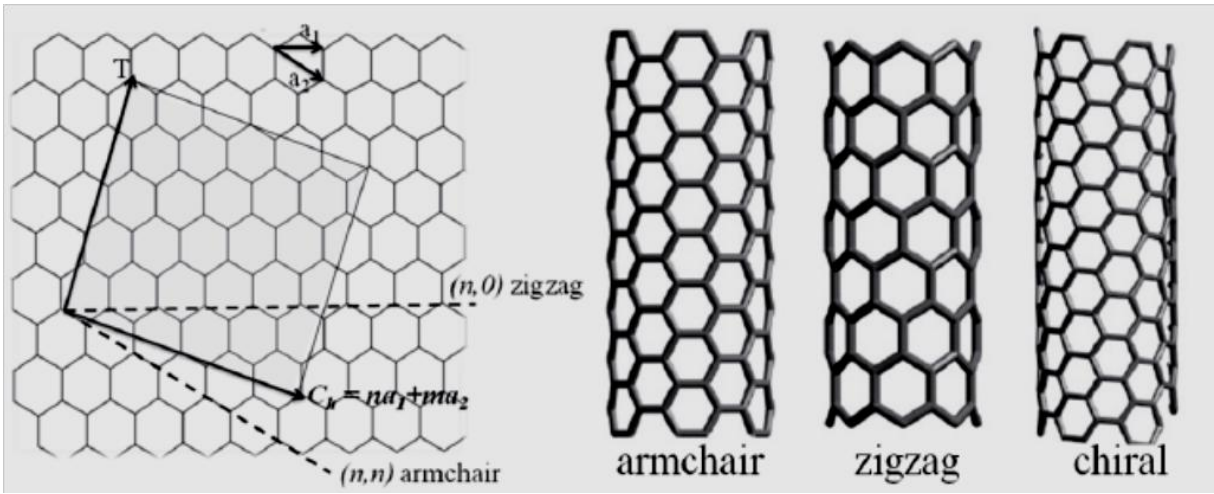

Fig.2. 7: The "zigzag", "armchair" and "chiral" types of SWCNT. From [85]

Carbon nanofibers have a cylindrical shape with graphene ring-based materials of 70-200nm diameter characterized by a high specific surface and lower production cost compared to CNTs.

CNTs/CNFs exhibit remarkable mechanical properties with extremely high intrinsic stiffness and strength in compression and tension [81, 82]. CNFs have a Young modulus of 400GPa and a tensile strength of 7 GPa [6] while CNTs exhibit even stronger mechanical properties with a Young's modulus on the order of TPa and a tensile strength of about 60 GPa [5,86] . Consequently, the CNTs/CNFs reinforcement of the cement matrix is a promising tool for enhancing the mechanical properties and the crack propagation resistance of cementitious materials. Studies have shown that the addition of CNTs in cement past increase its compressive strength up to 50% [83] and its resistance to crack propagation [84].

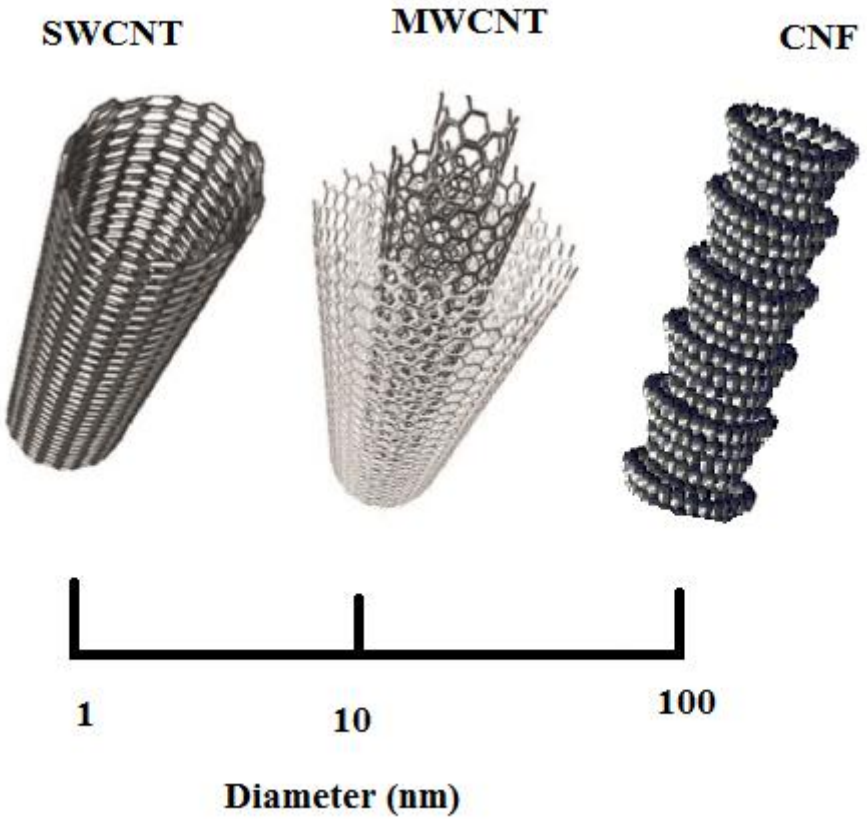

Fig.2. 8 : Schematic of SWCNT, MWCNT and CNF.

2.3.2. Nanoparticles:

A nanoparticle refers to a nano-object of any shape with all the three dimensions in the 1-100nm range. The 100nm limit induces the development of novel properties which the bulk material does not typically have [87, 88]. Nanoparticles have the characteristic of high surface area to volume ratio leading to an important potential of chemical reactivity. The insertion of Nanoparticles in cement can therefore promote the cement hydration. Nanoparticles also act as fillers that densify the microstructure of cement, reduce its porosity and thus considerably improve the mechanical and durability properties of cement based materials. Recently, many works have investigated the influence of the insertion of oxide nanoparticles such as nano-SiO_2, nano-TiO_2, nano-Al_2O_3 and nano-Fe_2O_3 in cement.

2.3.2.1. Nano-silica (Nano-SiO_2):

Is considered as the most used nano-oxide particle for cement based materials. Nano-SiO2 Plays an important role in accelerating the hydration of cement due to the high active surfaces of nano-silica. Additionally, modified cement with nano-silica exhibit a higher pozzolanic activity than high performance concrete with silica fume which leads to the production of additional C-S-H resulting in a strengthening and hardening effect as illustrated by the following reaction:

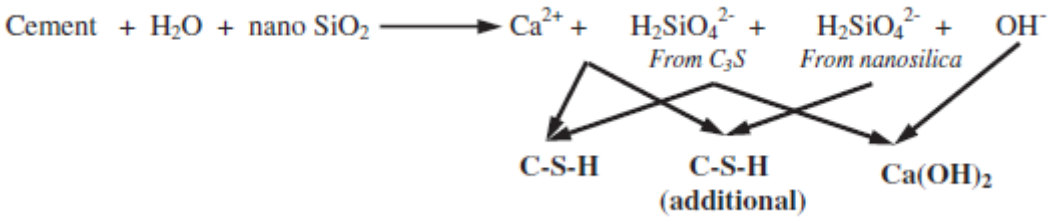

Fig.2. 9 : Hydration of cement modified by Nano-Silica

The compressive and flexural strength at 7 and 28 days of cement mortars containing nano-SiO_2 (mean diameter of 15nm) were found to be higher than mortars with silica fume [89, 90]. Hydraulic mechanical testing system (MTS) under load control and bending testing for flexural strength showed up to 26% increasing of the compressive strength at 28 days by the addition of 10% nano-SiO_2 compared to only 10% increasing in the case of 15% silica fume addition, while the flexural strength was enhanced by 27% at 28 days by the addition of nano-SiO_2 to cement mortar. Concrete containing silica nanoparticles have a refined pore structure and reduced permeability and enhanced durability properties. The Addition of nano-silica to concrete reduces the water adsorption and water permeability [91], reduces the chloride diffusion and helps to control the leaching of calcium [92].

2.3.2.2. Nano-Titania (Nano-TiO2):

Has provided concrete with self-cleaning and de-pollution capabilities generated by the mechanism of photocatalytic degradation of pollutants [93]. Nano-TiO_2 is mostly used in surface facades of buildings and in paving materials of roads. Addition of nano-TiO_2 in Portland cement accelerates the C-S-H formation at early ages [94]. Compared to nano-SiO_2, nano-TiO_2 shows a better performance for enhancing the abrasion resistance of concrete [95]. Nano-TiO_2 also enhances the compressive strength of cement based materials for small contents with an optimal gain of 18% obtained for 1% volume content [96] while the cement

compressive strength at 28 days is negatively affected by the addition of large nano-TiO_2 contents[97]. In addition, Nano-TiO_2 reduces the concrete porosity and permeability to aggressive substances which positively impacts the durability of concrete [98].

2.3.2.3. Nano-alumina (Nano-Al_2O_3):

Addition of nano-Al_2O_3 tremendously improves the elastic modulus at 28 days of mortar with up to 143% gain for 5 wt% content whereas a slight change in the compressive strength at 3, 7 and 28 days was observed for compressive strength. The elastic modulus enhancement is explained by the densification effect of the interfacial transition zone (ITZ) of mortar produced by nano-alumina [99]. In addition, a considerable change in the formation of the hydrated cement structure was revealed by SEM images where a significantly more compact microstructure with large crystals of portlandite was observed [100].

2.3.2.4. Nano-Iron (Nano-Fe_2O_3):

Addition of nano-Fe_2O_3 provides concrete with self-sensing capabilities offering the opportunity of continuous monitoring of concrete structures performance. The modified cement by Fe_2O_3 nanoparticles shows a significant change in resistance ($\Delta R/R_0$) with a linear decreasing as the compressive loading increases whereas $\Delta R/R_0$ is almost unchanged in plain cement [8]. The fractional change in resistance is an indicator of self-sensing ability of the nano-Fe_2O_3/cement composite. This indicator is 125% higher for cement mortar with 5% nano-Fe_2O_3 content against only 3% content [8]. In addition, strengthening effect is observed in modified mortars by nano-Fe_2O_3 due to the nanoparticles capacity to fill the pores of cement paste and therefore to optimize the overall microstructure. The high activity of Fe_2O_3 promotes also the cement hydration which positively affects the strength of cement. Experimental studies by Li et al [101] have found that cement mortar with nano-Fe_2O_3 content less than 10 % exhibits higher compressive and flexural strengths at 7^{th} and 28^{th} days up to 26% extent compared to plain Portland cement mortar. At the same time, the study points out that too high nano-Fe_2O_3 content can lead to the agglomeration of the nanoparticles and the creation of weak zones due to the unsuitable dispersion of the Fe_2O_3 nanoparticles in cement. In another study by Soltanian et al. [102], adding the Fe_2O_3 in cement slurry improves the elastic properties and the compressive strength up to 74% obtained for an optimal nano-Fe_2O_3 content of 11.81%. Results show also a higher viscosity and more

suspending ability of solid particles as well as lower free water of the cement slurries modified by nano-Fe_2O_3. Studies on self-compacting concrete (SCC) proved that adding Fe_2O_3 nanoparticles also improves the flexural and split tensile strengths with a maximum enhancement found for an optimal nano-Fe_2O_3 content of 4% [103].

2.3.2.5. Mixing Nanoparticles:

Adding binary and ternary combinations of SiO_2, Al_2O_3 and Fe_2O_3 nanoparticles in cement mortar was also studied and compared to single nanoparticle adding. Among the 22 groups of cement mortar mixtures, the best result was found for the ternary combination of of 1.25 wt% content with a 7–32% increase in the compressive strength and 14% decrease in the capillary absorption [104].

2.3.2.6. Other Nanoparticles:

Many other studies have been conducted to test the influence of adding other nano-oxides such as nano-ZnO_2, nano-CuO nano-$CaCO_3$ in cement base materials [105- 107]. Incorporation of nanoclay particles was also investigated and results showed a direct effect on improving the mechanical and durability properties [108- 110].

Conclusion:

The incorporation influence of the four most studied nanoparticles on the properties of cement based materials was reported from the literature and summarized in Table 2.1. As precised before, the mentioned properties highly depend on the nanoparticles content. Previous studies on the impact of addition in cement based materials are quite controversial and are difficult to compare since the concrete mix proportions and parameters (such as water/binder ratio) are not the same and the nanoparticles size and experimental procedures are different from a study to another. For instance, H. li et al. [111] found that 3 wt% addition of nano-silica improved the 28 days compressive strength by 26% of cement mortar with a water/binder ratio of 0.5 as illustrated in Fig. 2.10, while J. Liu [112] et al. found that the addition of the same amount of nano-silica has only 7.5% enhanced extent for a w/b=0.29 cement mortar.

Table 2.1: The Impact of insertion of nano-silica, nano-titania, nano-alumina and nano-iron in cement based materials.

Nanoparticle Type	**Impact on cement composites**			**References**
	Structural properties	**Mechanical, durability and rheological properties**	**Chemical and physical properties**	
Nano-SiO_2	• Refined pore structure. • Filler effect.	• Compressive and flexural strengths increase. • Reduced permeability.	• Hydration accelerator. • Higher pozzolanic activity.	[89-92]
Nano-TiO_2	• Reduced porosity.	• Abrasion resistance increase. • Compressive strength increase. • Reduced permeability.	• Self-cleaning. • De-pollution effect.	[93-98]
Nano-Al_2O_3	• Densification of ITZ.	• Elastic modulus increase.		[99,100]
Nano-Fe_2O_3	• Void filling of the C-S-H gel • Denser hydrated cement microstructure • Crystal size of Ca(OH)2 reduction.	• Compressive strength increase • Split tensile and flexural strengths increase. • Workability decrease	• Self-sensing.	[8,101-104]

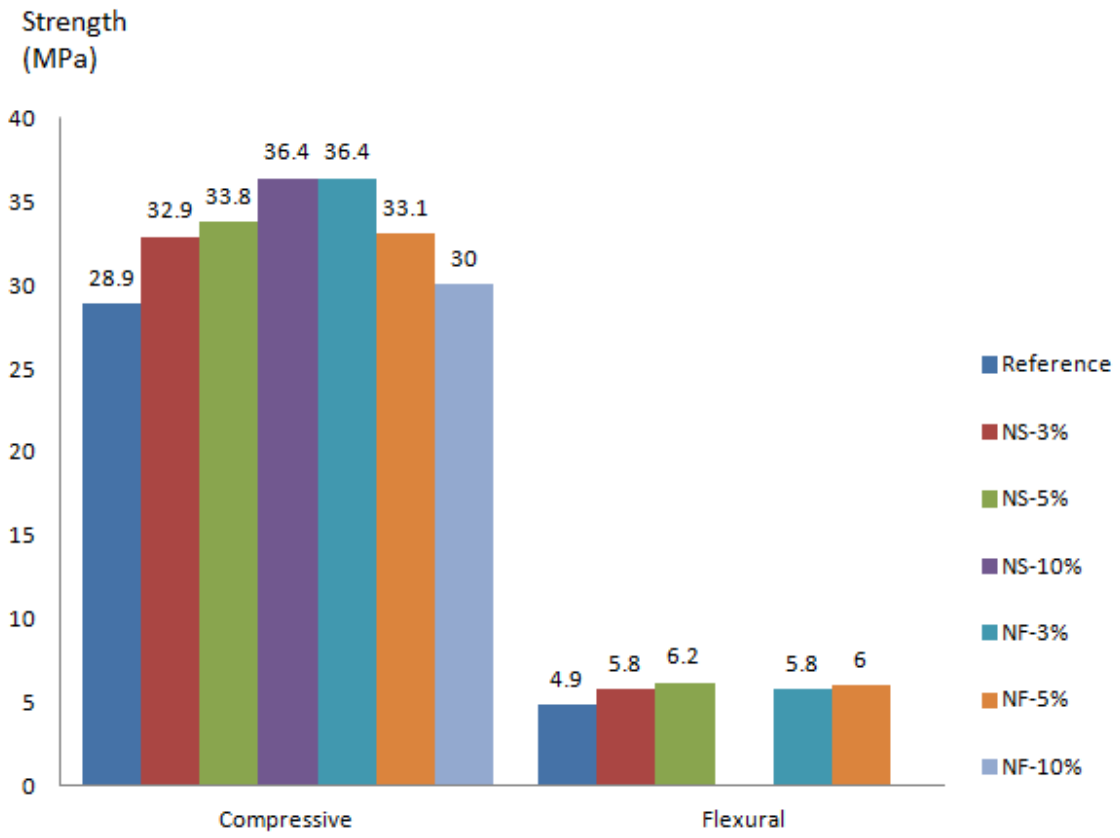

Fig.2. 10 : Compressive and flexural strengths at 28 days of cement mortar with w/b=0.5 modified by different contents of nano-silica (NS) and nano-Iron (NF). Adapted from [111].

Chapter 3: DFT study of Alite C_3S

3.1. Introduction:

Tricalcium silicate Ca_3SiO_5 (C_3S in cement chemistry notation) or alite is the main phase in ordinary Portland cement clinker. Alite is responsible for the short-term properties and early strength of cement due to the high reactivity of Ca_3SiO_5 with water.

Previous studies exhibit a sequence of 7 polymorphs of C_3S depending on temperature or impurities. The phase transformations upon heating occur in this order: three triclinic forms T_1, T_2, T_3, three Monoclinic forms M_1, M_2, M_3 and a Rhombohedral form R [113]. The complexity of C_3S polymorphism and confusions around defining the crystal structures of C_3S is behind the major challenges to simulate the properties of C_3S. Elastic modulus and hardness of C_3S have been determined experimentally by Velez et al. [114] from nanoindentation and resonance frequency measurements.

In addition, several molecular dynamic studies have been conducted. Manzano et al. investigated the elastic properties of M_3 phase of C_3S using force field methods [115]. Molecular dynamic work of Tavakoli and Taright on C_3S has demonstrated the great impact of the choice of force field on the determination of mechanical properties of C_3S[116]. A recent work by Mischra et al. reviewed the performance of several force fields such as CSH-FF [117], IFF [118] and REAXFF [28] to reproduce physical and chemical properties of C_3S and other cementitious systems and discussed the strength and limitations of each force field. No force field was found to be accurate for both calculating structural and mechanical properties and describing reaction mechanisms. A force field database named “cemff” was therefore produced in order to provide “guidelines” for selecting the most relevant force field depending on the nature of the targeted properties and the simulated system [119]. Given the large unit cell and the complexity of C_3S structure, very few *ab inito* simulations were performed to determine C_3S properties. Durgun et al. attempted to understand and control the reactivity of C_3S by introducing impurities by means of first principle methods [120].

In this chapter, we aim to provide a new insight into structural, electronic and mechanical properties by means of *ab intio* calculations. We choose the triclinic T_1 form of C_3S in our study since it is the most stable phase at room temperature.

3.2. Computational method

In this work, density functional theory (DFT) calculation were performed using the Projected Augmented Wave (PAW) [44] method within the Pseudopotential formalism implemented in the Vienna *ab initio* package (VASP) [121,122]. The valence electron configurations Ca $3s^2 3p^6 4s^2$, Si $3s^2 3p^2$ and O $2s^2 2p^4$ have been used. The exchange-correlation effects were approximated within the generalized gradient approximation (GGA) [123] using *Perdew*-Burke-Ernzerhof (PBE) parameterisation [124]. A well converged mesh of 5x5x5 k-points was used to sample the first Brouillon-zone using the Monkhorst-Pack method [125]. The convergence of results was tested to be fully obtained setting the energy cutoff of the plane-wave (PW) basis at 500eV. The structure was relaxed through conjugate-Gradient (cg) energy minimization algorithm with a stopping criterion of 10^{-5} eV. All calculations were performed at 0 K of temperature.

3.3. Results and discussion

3.3.1. Structural properties:

C_3S has a triclinic unit cell (T1 phase) at room temperature, classified under P/1 space group. Initially, the crystal structure of C_3S was setup according to the X-ray crystal data by Golovastikov et al. [126]. Fig.3.1 displays the atomic relaxed structure of C_3S. The unit cell of C_3S consists of 54 Ca atoms, 18 Si atoms and 90 oxygen atoms (18[Ca_3SiO_5]). The crystalline structure of C_3S is composed of independent SiO_4 tetrahedras surrounded by calcium atoms and interstitial oxygen atoms.

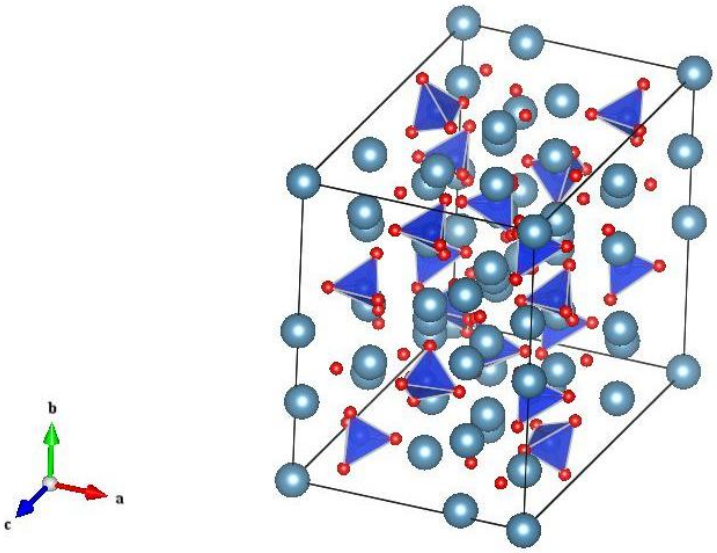

Fig.3. 1: Crystalline structure of C3S. Dark blue tetrahedras stand for SiO_4^- and blue atoms for Calcium atoms.

To test the performance of the PBE functional, structural optimisation was performed using two additional revised versions of PBE: rPBE [127] and RevPBE [128] that were developed in order to improve the adsorption energetics and the description of molecular bonding to surfaces. The corresponding optimized cell parameters using the three functionals were reported in Table 3.1.

Table 3.1: Calculated lattice constants (a_0, b_0 and c_0), cell angles (α, β and γ).

	This work			Exp. (T=298 K)	MD IFF (T=298 K)
	PBE (T=0 K)	rPBE (T=0 K)	revPBE (T=0 K)		
a_0 (Å)	11.70	11.87	11.91	11.67[a]-11.64[b]	11.74[c]
b_0 (Å)	14.28	14.43	14.47	14.24[a]-14.22[b]	14.16[c]
c_0 (Å)	13.71	13.88	13.92	13.72[a]-13.69[b]	13.70[c]
α (°)	104.81	104.79	104.78	105.50[a]-105.29[b]	104.9[c]
β (°)	94.45	94.23	94.19	94.33[a]-94.57[b]	94.4[c]
γ (°)	90.11	90.11	90.12	90.00[a]-89.85[b]	90[c]

[a] Ref: [126], [b] Ref[129], [c]Ref[130]

The obtained results are found to be in good agreement with the available theoretical and experimental data [126, 129, 130]. Using rPBE and revPBE functionals, the deviation with respect to experimental data is about 2% and 2.3% respectively while PBE functional performs remarkably better with less than 0.5% of deviation. Consequently, PBE functional was chosen for studying the properties of C_3S.

3.3.2. Mechanical properties:

The elastic constants were calculated from the stress-strain method implemented in the VASP package. According to the triclinic crystal symmetry of C_3S, the elasticity tensor has 21 non-zero independent constituents. The nine elastic constants C_{42}, C_{43}, C_{41}, C_{46}, C_{51}, C_{52}, C_{53} and C_{56} are found to have almost zero values and will be neglected in this analysis. We report in Table 2 the rest of the calculated elastic constants. This approximates the elastic tensor of our structure to a monoclinic crystal elastic tensor (13 non-zero constituents). This approximation is justified by the obtained value of the angle γ given in Table 1 (γ=90.11~90°) showing that the structure is close to monoclinic symmetry. The bulk modulus K and shear modulus G were determined according to the averaged Voigt–Reuss–Hill (VRH) approximation [131]. The Voigt and Reuss values of bulk and shear moduli were calculated using appropriate expressions for a monoclinic symmetry tensor [132]:

$$K_R = \frac{1}{S_{11} + S_{22} + S_{33} + 2(S_{12} + S_{23} + S_{31})} \qquad (3.1)$$

$$K_V = \frac{C_{11} + C_{22} + C_{33} + 2(C_{12} + C_{23} + C_{31})}{9} \qquad (3.2)$$

$$G_R = \frac{15}{4(S_{11} + S_{22} + S_{33}) - 4(S_{12} + S_{23} + S_{31}) + 3(S_{44} + S_{55} + S_{66})} \qquad (3.3)$$

$$G_V = \frac{C_{11} + C_{22} + C_{33} - (C_{12} + C_{23} + C_{31}) + 3(C_{44} + C_{55} + C_{66})}{15} \qquad (3.4)$$

Where S_{ij} are the constituents of the compliance tensor (inverse of elastic tensor), V and R denote Voigt and Reuss upper and lower bounds respectively.

The approximated Young's modulus (E) and Poisson's ratio (ν) were derived from the calculated bulk and shear moduli using the standard formulas:

$$E = \frac{1}{\frac{1}{3G} + \frac{1}{9K}} \quad (3.5)$$

$$\nu = \frac{1}{2}\left(1 - \frac{3G}{3K + G}\right) \quad (3.6)$$

The universal elastic anisotropy index A^u was used to quantify the elastic anisotropy of the C_3S crystal [141]:

$$A^u = 5\frac{G^V}{G^R} + \frac{K^V}{K^R} - 6 \geq 0 \quad (3.7)$$

A zero value of A^u refers to a locally isotropic single crystal. The bigger A^u is, the more anisotropic crystal it is. The obtained values are listed in Table 3.2.

The comparable values of C_{11}, C_{22} and C_{33} show a slight anisotropic behaviour. This is confirmed by the small value of A^u (A^u=0.11). However, the material is expected to be less compressible in the second direction (0 1 0) given the slightly higher value of C_{22} compared to those of C_{11} and C_{33}. As for the shear moduli (C_{ii}) i=4, 5, 6), the material is expected to have higher resistance to shear along the second direction.

Table 3.2: Calculated elastic constants C_{ij}, Bulk modulus (K), isotropic shear modulus (G), Young's modulus (E), Poisson's ratio (ν) and Universal anisotropy index (AU)

	This work (T=0°K)	Exp.[a] (T=298°K)	MD IFF T_1-C_3S[b] (T=298°K)	MD Reaxff M_3-C_3S[c] (T=298°K)	MD IFF M_3-C_3S[d] (T=298°K)
C_{11} (GPa)	171.80				
C_{22} (GPa)	198.85				
C_{33}(GPa)	175.66				
C_{44}(GPa)	47.42				

C_{55}(GPa)	64.19				
C_{66}(GPa)	56.60				
C_{12}(GPa)	58.72				
C_{23}(GPa)	74.07				
C_{31}(GPa)	61.97				
C_{54} (GPa)	-1.67				
C_{61} (GPa)	-10.36				
C_{62} (GPa)	-8.49				
C_{63} (GPa)	-4.85				
K (GPa)	103.08		103.99	103	105
G (GPa)	56.58		65.48	54.5	
E (GPa)	143.47	135-147	162.36	138.9	143.7
ν	0.27	0.3	0.24	0.28	0.28
A^U	0.11				

[a] Ref: [129], [b] Ref[116], [c] Ref[115], [d]Ref [134]

The resulting bulk modulus value (B=103.88 GPa) perfectly agrees with the work of Tavakoli and Tarighat based on MD simulations [116]. Nevertheless, our results predict a shear modulus of 56.58 GPa for C_3S, which is 13% smaller than the value predicted by Tavakoli and Tarighat. To the best of our knowledge, there are no direct experimental measurements of the bulk or shear moduli. We also compared our results to MD studies on M_3 phase of C_3S [115, 134]. We notice that bulk and shear moduli obtained by Manzano et al. (K=103 GPa, G=54.5 GPa) are pretty close to our results. This can be explained by the extremely small transformation enthalpies of the C_3S polymorphism and very similar modifications undergoing a phase transformation [133], making the elastic response of the different phases of C_3S quite similar. The Young's modulus (E) was experimentally determined with a value of 135 GPa by means of nanoindentation, and 147 GPa by resonance frequency measurements [114]. Our calculated Young's modulus (E=143.47 GPa) lies between the two experimental values. The obtained value of Young modulus by Tavakoli and Tarighat is higher (about 11%) than ours. The Young's modulus value of the M_3-C_3S by Manzano et al. (E=138.9GPa) [115] or by Mishra et al. [134] (143.7 GPa) are again quite

close to our calculated value. Our calculations predict a Poisson's ratio equal to 0.27 for C_3S. This value is rather closer to the one obtained by molecular dynamics for M_3-C_3S (ν=0.28) than that obtained by Tavakoli & Tarighat for T_1-C_3S (ν=0.24). The very comparable results of the obtained elastic parameters for the T_1-C_3S and those computed for M_3-C_3S confirm the similarity of the elastic behaviour between T_1 and M_3 phases of C_3S.

3.3.3. Electronic properties

The contribution of each atom type (Calcium, Silicon and Oxygen) to the total density of state (DOS) was calculated to investigate the electronic structure of C_3S. The Fermi level was set to zero to which all energies were relatively calculated. From Fig.3.2, we see that both oxygen and calcium atoms contribute to the valence region; while the conduction region is dominated by calcium atoms with weak contribution of Oxygen atoms. Si atoms contribute very little to the total DOS. The valence and conduction regions are separated by a band-gap of 3.57 eV. We calculated the partial DOS (PDOS) of both calcium and oxygen atoms to further understand the origin of the states contribution to DOS. Fig.3.3 shows that the upper part of valence region, lying between -10.0 eV and Fermi level, derives from 2p orbitals of Oxygen atoms; while the bottom part of the conduction region (between Fermi level and 10.0 eV) is due to the 3d-states of Calcium atoms. This result suggests that C_3S reactivity is mainly due to 2p-O and 3d-Ca states. Going through deeper energies in the valence region, we see that the region lying between -20.0 eV and -10.0 eV is a shared contribution of 3p-Ca and 2s-O states followed by a sharp peak located between -40.0 eV and -30.0 eV that derives from 3s-Ca states.

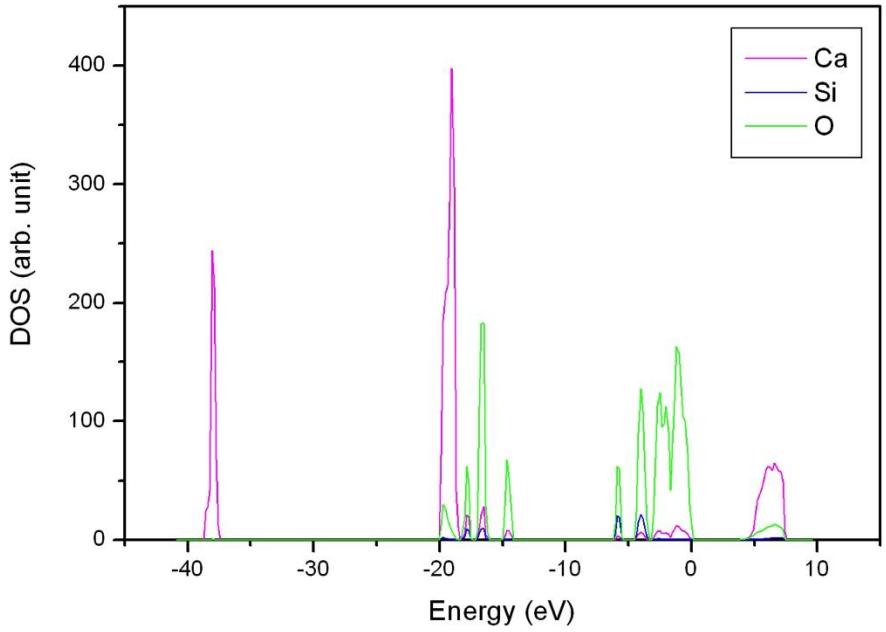

Fig.3. 2 : Total DOS of C_3S with atomic contributions.

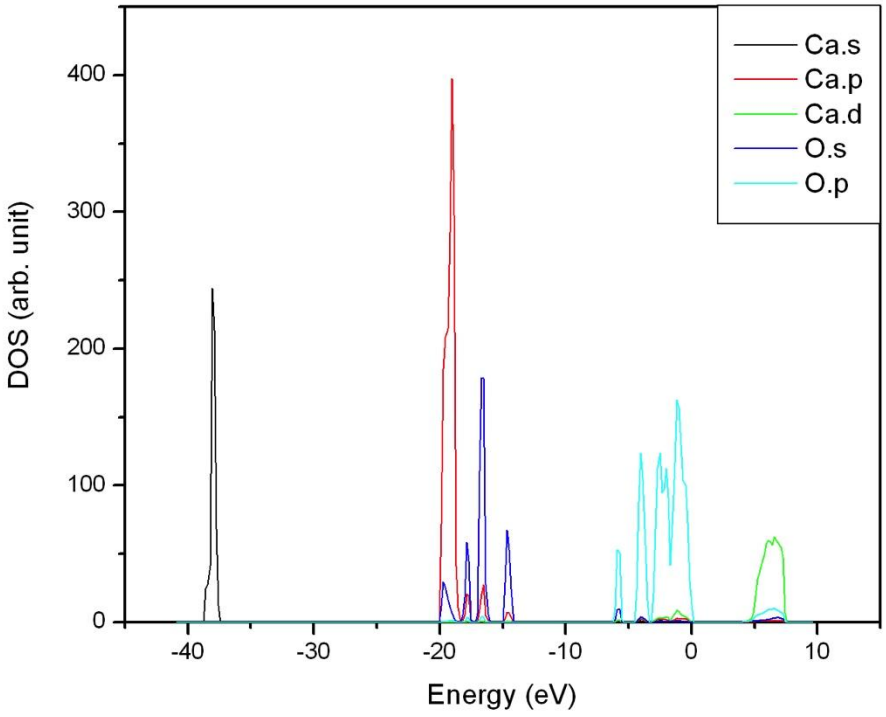

Fig.3. 3 : Partial DOS of Oxygen and Calcium with orbital contributions.

In order to investigate the charge transfer, we plotted the valence charge density in the plane P, which contains all the atom types as illustrated in Fig.3.4. Fig.3.5 gives more details concerning the density distribution. The charge distribution allowed us to distinguish two types of oxygen atoms. The first one includes Oxygen atoms that are only bonded to Calcium atoms. We denote these oxygen atoms by Oc-type. The second type gathers oxygen atoms bounded to silicon atoms in silicon–oxygen tetrahedrons SiO_4^{4-} that we will refer to by Os. Larger density is observed between silicon and oxygen indicating a strong covalency.

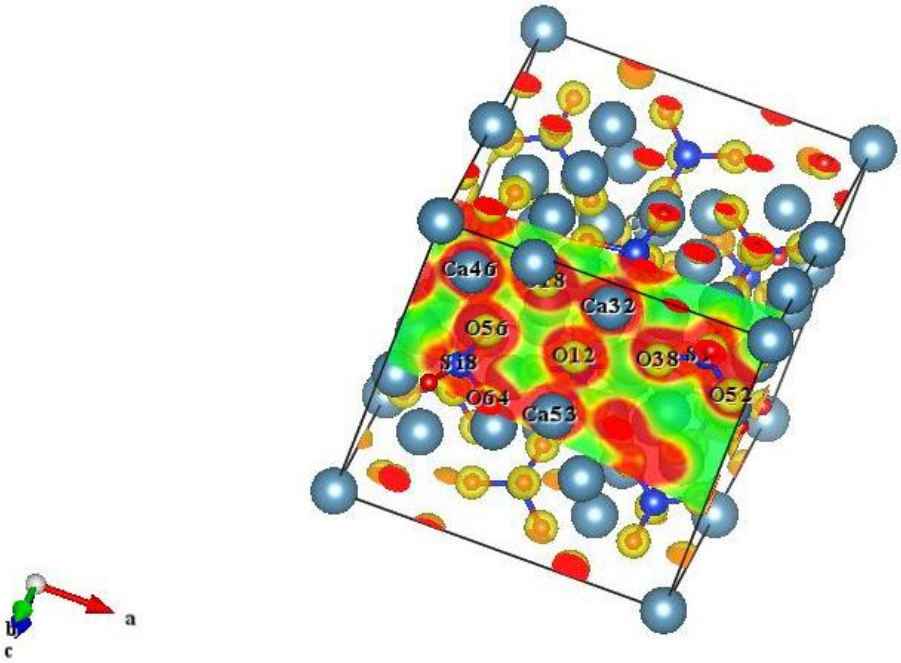

Fig.3**.** 4 : Charge density on the P plane of C_3S

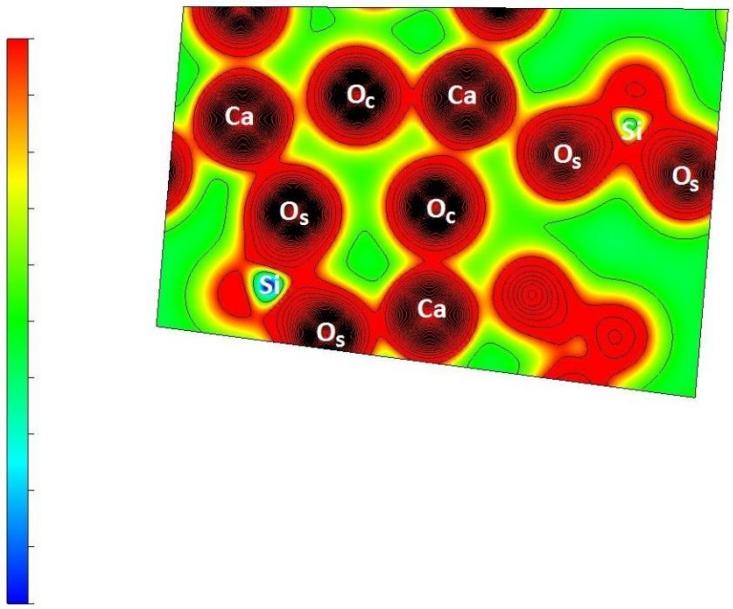

Fig.3**.** 5 : Charge density map on the P plane of C_3S

Thereafter, we calculate Bader charge [135] of atoms included in the considered plane and were reported in Table 3.3. The present results showed that Ca and Si atoms together transfer +4.58e. This obtained charge transfer is very close to that of the C_2S (Ca_2SiO_4) which is about +4.61e reported by E. Durgun et al. using hybrid DFT functional [120]. However, our calculations highly overestimated the net charge of silicon atoms +3.08e against +1.0e± 0.1e charge on Si in O_4 coordination according to the experiment [136, 137] and charge analysis by Mishra et al. [6]. The shortcoming of predicting a wide range for charges of a given system as well as a poor agreement of the silicon charge in a O_4 coordination by *ab initio* methods was reviewed in the study by H. Heinz and U W. Suter [138] where a particular attention was given to atomization ionization energies of the elements across the periodic table in order to estimate semi-empirical values in good agreement with the experiment. For instance, in the INTERFACE force field formalism, atomic charges of C_3S were derived with high accuracy based on the on the thermodynamic consistency approach that both combines experimental data and chemical-physical knowledge for each compound as explained in reference [118]. Our results indicate a Oc net charge of -1.43e; whereas it is equal to -1.55e on average for Os atoms. This means that each Os atom takes about -0.12e more charge from the system compared to an Oc atom. This analysis suggests that Os-type atoms are more bound to the system than Oc-type atoms. Moreover, Os-Si bonds of 1.63-1.68 A length are shorter than the Oc⋯Ca (2.35-2.51 A) indicating that the Os⋯Si bond is much stronger than Oc⋯Ca bonds. This characteristic agrees with the large difference in electronegativity between Ca and O ions

(χO-χCa =2.55) compared to the electronegativity difference between Si and O (χO-χSi =1.65) according to Pauling scale of electronegativity [139]. Correspondingly using MD calculation, R. K. Mishra et al. reported that the Si-O bonds length of 1.6 Å is shorter and the ionization of the valence electrons are moderate [132], while the Ca···Oc (and, Ca···Os) distance was near to 2.40 Å leading to a strong ionization of valence electrons.

Table 3.3: Bader charge of Oc, Os, Ca and Si in the pure phase of C_3S and C_2S.

Atoms	C_3S	C_2S[b]
Oc	-1.440 e	-
Ca	+1.530 e	+1.530 e
Si	+3.050 e	+3.080 e
Os	-1.550 e	-1.535 e

[b]ref: [120]

To get an insight into the reactivity of C_3S, we analysed the Local density of states (LDOS) in the valence band maximum (VBM) and conduction band minimum (CBM). Here, we use the Fukui function based on the frontier orbital theory to characterize the reactive sites under electrophilic and nucleophilic attacks [140]. Fig.3.6 shows that LDOS of the CBM is dispersed in regions in the vicinity of some calcium atoms. This suggests that calcium atoms are susceptible to be active under nucleophilic attack (such as OH^-). In the other hand, Fig.3.7 shows that the LDOS of the VBM is highly accumulated only around Oc atoms suggesting that reactivity under electrophilic attacks is mainly due to Oc atoms. In contrast, Os are expected to be inactive under electrophilic attacks. This agrees with the fact that Oc are badly bounded to the system, conducting to an easy loss of electrons in favour to electrophile cations (H^+ for instance).

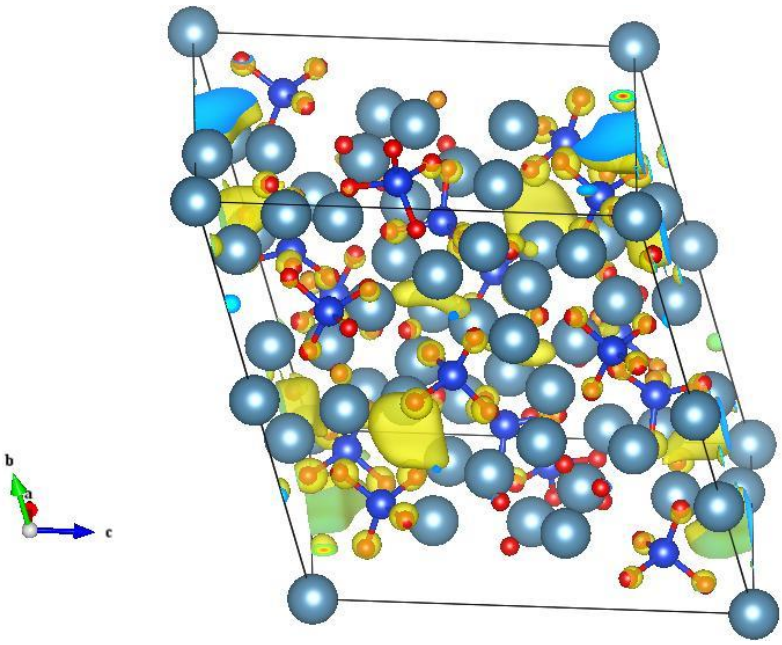

Fig.3. 6 : LDOS of CBM of C_3S.

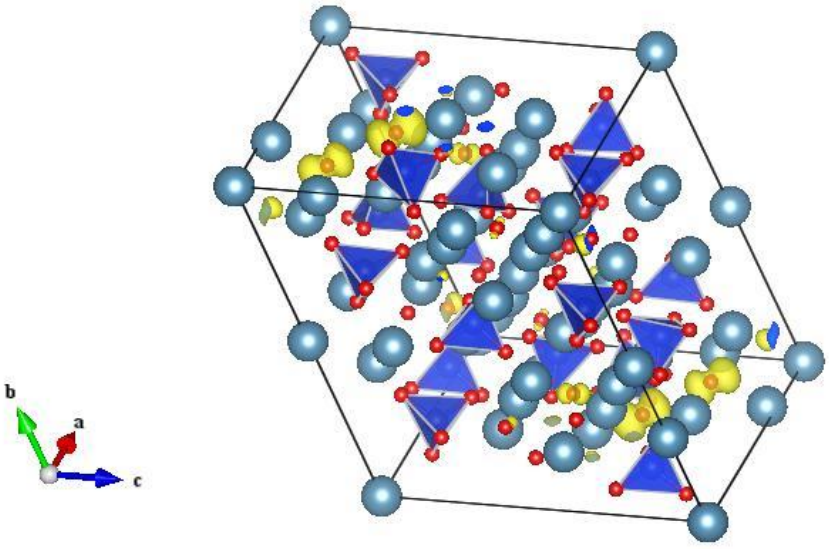

Fig.3. 7: LDOS of VBM of C_3S.

3.4. Conclusion

The present work attempted to determine structural, mechanical and electronic properties of C_3S by means of DFT calculations. Elastic behaviour of C_3S was characterized by taking into account the crystal system of C_3S and the anisotropy of the material. Main elastic constants were calculated and young modulus was deduced. Our results are in excellent agreement with experiment. We also calculated the electronic properties to get an insight into the reaction mechanism of C_3S. LDOS of VBM and CBM were analysed to characterize reactive sites of C_3S. Two oxygen atom-types were distinguished from the charge density of the system. LDOS of VBM is highly localized explaining the observed high reactivity of C_3S under electrophilic attacks (e.g. H^+). Moreover, reactive sites under electrophilic attacks were noticed to be only around some specific oxygen atoms. In contrast, the analysis of LDOS for CBM suggests that some calcium atoms are responsible for undergoing reaction with anions such as hydroxide ion (OH^-).

Chapter 4: DFT study of Belite C_2S

4.1. **Introduction**

Belite, or Dicalcium Silicate, has been the focus of attention for producing environmentally friendly cements. Belite requires a lower energy synthesis and has a low limestone demand compared to alite, the first major component of cement. In fact, the fabrication of high belite cements can reduce up to 35% CO_2 emission than ordinary cement [142]. Unfortunately, the slow hydration mechanism of belite leads to a slower development of belite rich cement strength. Several studies have been conducted on improving belite's reactivity. Belite has a sequence of five polymorphs in this ascending order with increasing temperature of stability: γ- C_2S, β- C_2S, α'_L-C_2S, α'_H-C_2S and α-C_2S [143,144]. γ-belite with the orthorhombic olivine structure (space group: Pbnm) is the thermodynamically stable phase at room temperature. γ-belite is almost nonreactive with water [145]. On the other hand, the metastable β phase of belite with a monoclinic phase (space group: P21/n) at room temperature conditions exhibits higher reactivity rate with water at room temperature. β-phase is the predominant form of belite in normal portlandite cement. The α'_L, α'_H and α phases are stable at higher temperature. Recently, the order of phase transitions and phonon dynamics of belite were studied using DFT calculations and interatomic potential functions [146]. Chemical stabilization of reactive β-form of belite down to room temperature by incorporating guest ions has been investigated [147,148] and many experimental works tried to examine the polymorphism-reactivity dependence [149]. However, the reactivity mechanism of the different belite phases is still very little understood due to experiment limitations and inconsistencies between theoretical predictions and experimental data [150]. In addition, considering the low synthesis temperature of gamma-polymorph compared to β-polymorph makes a reactive version of γ-belite widely chased from the environmental and economical perspective [151]. Therefore, studying the influence of the crystallography of belite phases on reactivity is crucial to enhance its reactivity. Moreover, belite is responsible for developing late strength. Understanding the effect of the belite complex on cement cohesion and mechanical properties is quite important in the field of developing high performance concrete [152]. Atomistic simulations using first-principle and force field methods have demonstrated their great potential for studying cement complex phases [116, 119, 153]. In this chapter, we aim to investigate and to compare the properties of the belite ground-state phase: γ-phase, as

well as the most present form of belite in traditional cements; i.e. β-phase, by means of first-principles calculations.

4.2. Computational details

In this work, we have performed DFT (Density Functional Theory) calculations on gamma_belite using the Vienna *ab initio* package (VASP) [121,122]. The Projected Augmented Wave (PAW) [44] method was adopted with the Pseudopotential approach. Generalised Gradient approximation GGA [123] with PBE (*Perdew*-Burke-Ernzerhof) parameterisation [32] and Local density approximation LDA [154] were selected to evaluate the exchange-correlation effects and to test the functional dependence of our results. The convergence of total energies was amply reached with respect of a cut-off energy of 600 eV for the three functionals. Well converged meshes of 9x4x7 and 8x7x5 using Monkhorst-Pack method [125] were chosen to sample the first Brouillon-zone for gamma-phase and beta-belite respectively. Geometry optimisation was achieved through conjugate-Gradient (cg) energy minimization algorithm with a stopping criterion of 10^{-7} eV.

4.3. Results and discussions

4.3.1. Structural properties

The initial structure of γ-belite was set up based on Smith et al. experimental data [155] and β-belite initial structure was taken from Tsurumu et al. work [156] for the structural relaxation. The unit cells of both γ- and β-belite consist of 16 Oxygen atoms, 8 Calcium atoms and 4 Silicon atoms (4[Ca_2SiO_4]) as illustrated in Fig.4.1.

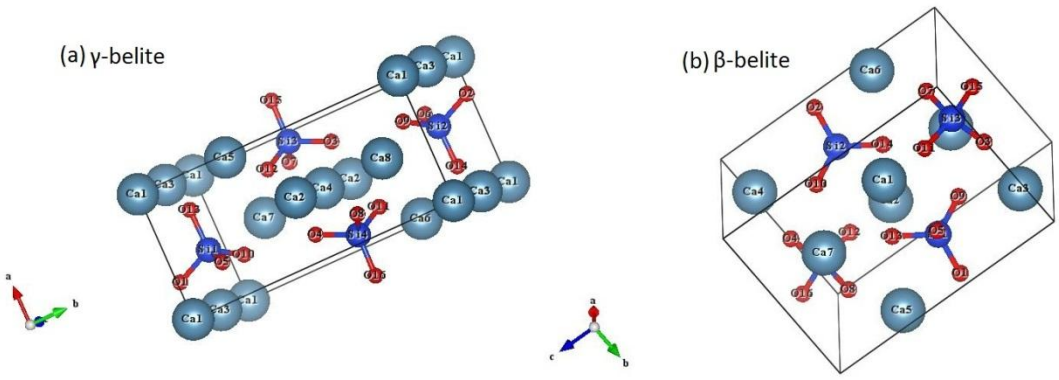

Fig.4. 1: Structure of (a) γ-belite and (b) β-belite.

The structures were completely relaxed from each functional. For a given set of lattice constants, total energies are computed by means of LDA and GGA. The equilibrium bulk modulus (B_0) and its pressure derivative ($B_0^{'}$) have been determined by fitting the obtained energy data with respect to volume using the Murnaghan equation of state EOS [157]:

$$E(V) = E_0 + \frac{B_0.V}{B_0^{'}}\left[\left(\frac{V_0}{V}\right)^{B_0^{'}}.\frac{1}{B_0^{'}-1}+1\right]-\frac{B_0.V_0}{B_0^{'}-1} \qquad (4.1)$$

Where E_0 and V_0 are respectively the equilibrium energy and volume at zero pressure.

The calculated equilibrium cell parameters, bulk modulus and its pressure derivative are given in Table 4.1 and are compared to previous experimental and theoretical data [115,158-161]. The three used functionals provide very comparative cell parameters values to experiment data. For γ-belite, the best agreement is found by GGA approximation for the calculation of lattice constants with a slight underestimation of the cell parameters by less than 1.5%. The computed bulk modulus is in good agreement with previous theoretical studies. The results obtained by PBEsol are the closest to available data. Nevertheless, we couldn't find any available experimental data of γ-belite bulk modulus in the literature. Thus, our calculations predict the bulk modulus of γ-belite to be approximately around 85 GPa.

For β-belite, GGA slightly overestimates the lattice constants (less than 1.3%) in opposition to LDA with less than 1.9% underestimation of lattice constants. The calculated bulk modulus is

in great agreement with theoretical available data and the found values by the two functionals are very comparable (97.0 GPa from GGA and 104.7 GPa from LDA).

Table 4.1: Calculated lattice constants (a_0, b_0 and c_0), cell angles (α, β and γ), bulk modulus (B) and its pressure derivative (B') of γ-belite and β-belite and compared to experimental and other theoretical data.

	γ-belite					β-belite			
	This work (GGA)	This work (LDA)	Expt.[158]	Previous theor. (GGA-PBE) [159]	Previous theor. (ReaxFF) [160]	This work (GGA)	This work (LDA)	Expt. [161]	Previous theor. [115]
a_0 (Å)	5.07	5.02	5.08	5.11	5.13	5.57	5.43	5.5	5.11
b_0 (Å)	11.19	10.98	11.23	11.33	11.17	6.82	6.65	6.76	11.33
c_0 (Å)	6.72	6.6	6.76	6.8	6.33	9.37	9.14	9.32	6.8
α	90°	90°	90°	90°	90°	90°	90°	90°	90°
β	90°	90°	90°	90°	90°	94.7°	95.4185°	94.1°	94°
γ	90°	90°	90°	90°	90°	90°	90°	90°	90°
B (GPa)	82.1	85.2			95.56	97.03	104.69		111
B'	2.13	3.48				3.56	4.15		

4.3.2. Mechanical properties

The γ-polymorph of belite belongs to space group Pbnm and has an orthrohombic crystal structure. The orthotropic materials are characterised by three symmetry planes. According to this crystal symmetry, the elasticity tensor has 9 non-zero independent constituents: C_{11}, C_{22}, C_{33}, C_{44}, C_{55}, C_{66}, C_{12}, C_{23}, C_{31}. The necessary and sufficient mechanical stability conditions, or the generic stability criteria, of an unstressed orthorhombic crystal to be satisfied are the following [162]:

$$C_{11} > 0;\ C_{11}C_{22} > C^2_{12} \quad (4.2)$$

$$C_{11}C_{22}C_{33}+2C_{12}C_{13}C_{23}-C_{11}C^2_{23}-C_{22}C^2_{13}-C_{33}C^2_{12}>0 \quad (4.3)$$

$$C_{44}>0;\ C_{55}>0;\ C_{66}>0 \quad (4.4)$$

The β-polymorph of belite belongs to space group P21/n and has a monoclinic crystal structure. According to this crystal symmetry, the elasticity tensor has 13 non-zero independent constituents: C_{11}, C_{22}, C_{33}, C_{44}, C_{55}, C_{66}, C_{12}, C_{23}, C_{31}, C_{54}, C_{61}, C_{62}, C_{64}. The necessary and sufficient mechanical stability conditions, or the born generic stability criteria, of an unstressed orthorhombic crystal to be satisfied are the followings [132]:

$C_{11}, C_{22}, C_{33}, C_{44}, C_{55}, C_{66} >0$ (4.5)

$C_{11}+C_{22}+C_{33}+3(C_{12}+C_{23}+C_{31})>0$ (4.6)

$C_{22}C_{66}-C_{62}^2>0$; $C_{44}C_{55}-C_{54}^2>0$ (4.7)

$C_{22}+C_{33}-2C_{23} >0$ (4.8)

$C_{33}(C_{22}C_{66}-C_{62}^2)+2C_{23}C_{26}C_{26}-C_{23}^2C_{66}-C_{36}^2C_{22}>0$ (4.9)

$2[C_{16}C_{36}(C_{22}C_{13}-C_{12}C_{23})+C_{16}C_{26}(C_{33}C_{12}-C_{13}C_{23})+C_{36}C_{26}(C_{11}C_{23}-C_{12}C_{13})]-[C_{16}^2(C_{22}C_{33}-C_{23}^2)+C_{36}^2(C_{11}C_{22}-C_{12}^2)+C_{26}^2(C_{11}C_{33}-C_{23}^2)+C_{66}.x]>0$ (4.10)

Where $x=C_{11}C_{22}C_{33}-C_{11}C_{23}^2-C_{22}C_{31}^2-C_{33}C_{12}^2+2C_{12}C_{23}C_{31}$ (4.11)

The calculated elastic constants by the used functionals are listed in Table 4.2. In all cases, the obtained values satisfy the elasticity stability conditions. From elastic coefficients, we have determined the elastic compliances S_{ij}. Then, the four well-known parameters to quantify the response of a material to various deformations: the bulk modulus (K), shear modulus (G), Young modulus (E) and Poisson's ratio are derived from the Voigt–Reuss–Hill (VRH) [131] approximation that establishes the connection between the elastic behaviour of an aggregate and a single crystal. The values of bulk and shear moduli can be taken as the average of Voigt and Reuss bounds (eq.3.1, eq.3.2, eq.3.3 and eq.3.4). Then, the average value of Young's modulus E and Poisson's ration can be obtained from the calculated values of K and G as detailed in the previous chapter (eq.3.5 and eq.3.6). To quantify the elastic anisotropy, we used the universal elastic anisotropy index A^u [141] calculated from Voigt and Reuss bounds of K and G via equation 3.7. A zero value of A^u refers to a locally isotropic single crystal. The bigger A^u is, the more anisotropic it is. Finally, we present the previous listed parameters in Table 4.2 along with the experimental and theoretical available data.

Table 4.2: Calculated elastic constants C_{ij}, Bulk modulus (K), isotropic shear modulus (G), Young's modulus (E), Poisson's ratio (ν) and Universal anisotropy index (A^U)

	γ-belite				β-belite				
	This work		Other works		This work		Other works		
	GGA	LDA	Reax FF [151]	IP [146]	GGA	LDA	Reax FF [151]	IP [146]	Exp.
C_{11} (GPa)	189.22	200.82			167.1	202.19			
C_{22} (GPa)	128.58	136.26			192.85	254.47			
C_{33}(GPa)	163.62	174.28			168.76	203.72			
C_{44}(GPa)	60.90	65.24			52.58	62.25			
C_{55}(GPa)	46.75	49.92			45.53	55.92			
C_{66}(GPa)	64.34	67.5			31.12	41.51			
C_{12}(GPa)	72.22	76.63			47.97	58.66			
C_{23}(GPa)	71.81	76.74			58.48	72.02			
C_{31}(GPa)	76.89	80.87			63.39	77.29			
C_{54} (GPa)	-	-			-4.76	8.01			
C_{61} (GPa)	-	-			-10.21	-1.6			
C_{62} (GPa)	-	-			0.95	2.68			
C_{63} (GPa)	-	-			-9.07	-12.47			
K (GPa)	101.08	107.31	95.56	93.1	95.73	119.02	125.8	84.9	
G (GPa)	50.51	53.66	48.58	50.8	47.84	59.78	59	41,1	
E (GPa)	129.89	137.98	124.7	129	123.02	153.62	153.1	106.2	130-140 [164,165]
ν	0.29	0.29		0.27	0.29	0.28		0.30	0.30 [166]
A^U	0.29	0.29			0.44	0.41			

Comparing values of C_{11}, C_{22} and C_{33}, both LDA and GGA functionals predict a higher compressibility in the second principal direction (0 1 0) of the γ-phase crystal. The highest obtained value of C_{22} in the case of β-structure suggests a great resistance to compressibility in the second direction (0 1 0). Almost equal C_{11} and C_{33} values for β-belite predict a comparable resistance to compressibility in the first and third directions. Now, comparing C_{11}, C_{55}, and C_{66}, the system has more resistance to shear solicitation along the (0 0 1) direction for γ-belite and along the (1 0 0) for the β-belite.

Obtained values from both LDA and GGA functionals are fairly comparable for the γ-structure; whereas a functional dependence of the results in the case of β-belite is noticed. Only mechanical properties of β-belite have been experimentally determined, thus we consider the reference values for γ-belite to be those predicted by other theoretical previous studies. In the following analysis, we will focus on the calculated values from GGA as the obtained lattice parameters are the closest to the experiment compared to LDA functional that generally produces more rigid crystals [163]. The calculated bulk modulus K for γ-belite (101.08 GPa) is in great agreement with the calculated values from Force field calculations 95.56 GPa by Wang et al. [151] and 93.1GPa by Rejmak et al. [146] The calculated bulk modulus for β-belite is about 5% lower with a value of 95.73GPa. Theoretical results using molecular dynamics calculations are quite controversial comparing the results obtained for β-belite [146,151]. The calculated bulk modulus by Wang et al. for β-belite (125.8 GPa) using reactive forcefields method is 48% higher than that calculated by Rejmak et al (84.9GPa).

The Shear and Young's moduli were also found to be very comparable for both phases with slightly lower value for β-belite (of about 5%). Again for γ-belite, our results for shear modulus and Young's modulus are in excellent agreement with force field studies [146, 151]. On the other hand, greater differences are observed for β-belite. Results by Wang et al. describe a stiffer material with a Young's modulus of 153.62 GPa whereas the opposite was found by Rejmak et al. with a value of only 106 GPa. These values somewhat deviate from the 130-140 GPa range set by experimental measurements for beta-phase [164, 165]. By contrast, our results (E=123.02 GPa) are fairly close to the experiment with a slight underestimation of about 5%. Let us notice that for a non-isotropic material the calculated value of the Young's modulus strongly depends on the considered direction. Since calculated value only corresponds to the average value, differences between results are rather due to the used averaging formulas. We obtain the same value of Poisson's ratio for γ-phase (0.29) in both phases, which is quite close to -phase's 0.3 obtained by experimental studies on β-belite [166]. The calculated anisotropy indexes corresponding to a non-zero value confirms the anisotropy nature of belite. A higher anisotropy trend is observed in β-belite with a higher anisotropy index of 0.44 compared to 0.29 as expected considering the more symmetrical structure of the γ-belite.

4.3.3. Electronic properties

To investigate the bonding character of γ- and β-belite, we have calculated the net charges of atoms from Bader [46] partitioning of charge density using GGA functional. We report the net

charge of each atom type in Table 4.3. Looking at the calculated Bader charge of both phases, we noticed that Bader charge is almost equitably distributed between atoms of Si and atoms of Ca. Silicon atoms have an averaged charge of about +3.1|e| in both phases whereas calcium atoms Caγ in γ-phase and Caβ in β-phase have a bader charge of +1.56|e| and +1.58|e| respectively. The bader charges on oxygen atoms Oγ in γ-belite are also equally distributed with a bader charge of about -1.55|e|. However, different Bader charges were obtained for Oβ atoms showing that the oxygen atoms are not equivalent in β-belite. From Table 4.3, we can define two sets of Oβ: O1-type and O2-type with averaged charge of -1.54|e| and -1.57|e| respectively.

Table 4.3: Bader charge of γ and β-belite

Atoms	γ-belite	β-belite
Ca	+1,56	+1,57
Si	+3,09	+3,10
O1	-1,55	-1,54
O2		-1,57

For further understanding of the bonding characteristics of the two belite phases, the total DOS illustrating the contribution of each atom type (Calcium, Oxygen and silicone) is calculated from GGA functionals. We display in Figure 3 the total DOS obtained from GGA functional for both γ-, and β-belite. Calculated Fermi level from is subtracted to get a Fermi level at zero energy as presented in DOS and PDOS graphs. As shown in Fig.4.2, for both γ- and β-belite the upper DOS region of the valence region of below the Fermi level is mainly due to Oxygen atoms contribution. The partial DOS (PDOS) of Oxygen presented in Fig.4.3 shows that this part is derived from 2p orbitals. In contrast, the conduction part above the Fermi level is dominated by calcium contribution and more precisely by 3d states of calcium as illustrated in Fig.4.4. This result perfectly agrees with Wang et al.[14] work and confirms that belite reactivity is mainly due to 2p-O and 3d-Ca states. The total DOS in Fig.4.2 shows very small contribution of Si atoms to DOS and thus for belite hydration reactivity.

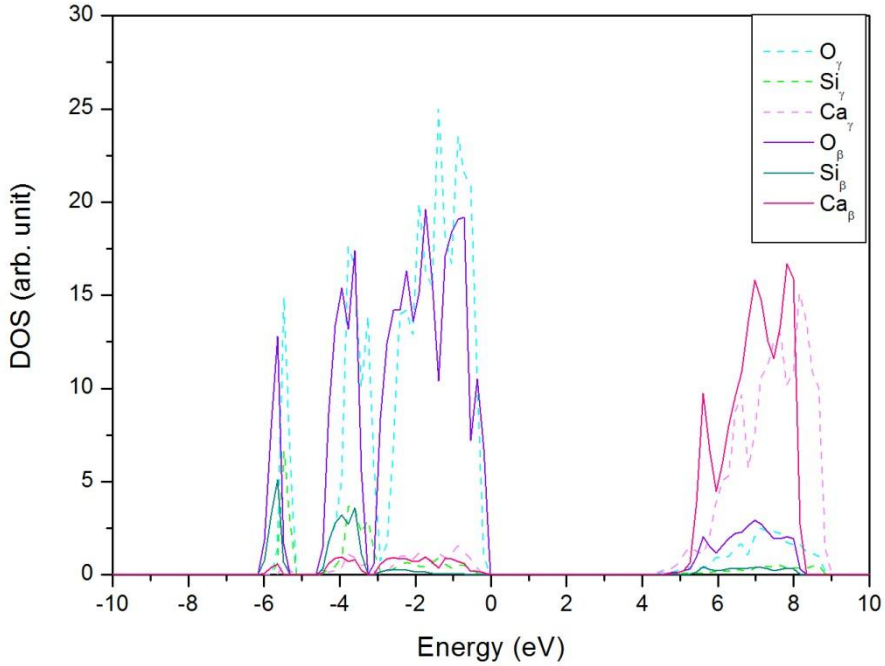

Fig.4. 2: Total DOS of γ-belite and β-belite, including atomic contributions

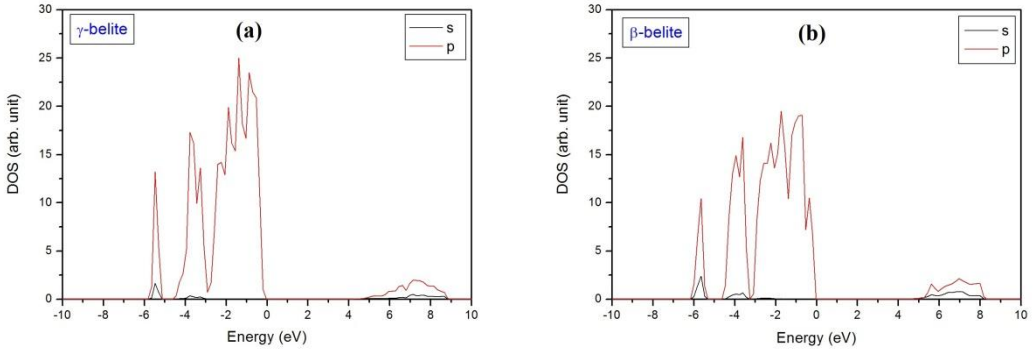

Fig.4. 3: Partial DOS of Oxygen with orbital contributions of (a) γ-belite and (b) β-belite.

To shed light on the link between the DOS and reactivity with water, the valence part of DOS can be analysed for the two phases from Fig.4.2. In the valence part, by looking at the closest peaks to Fermi level of γ- and β-belite, a short peak near the Fermi level situated at -0.36 eV is only seen in β-belite. To understand the origin of this peak, we have investigated the contributions of O1 and O2 oxygen types defined in by the bader charge analysis. Fig.4.5 shows that the spotted peak with the closest position to the Fermi level exclusively arises from

O1-type contribution. Such specific oxygen atoms (O1-type) have the closest most occupied energy levels to the Fermi level, and thus are expected to be more active under electrophilic attacks than the rest of oxygen atoms (O2-type). This difference can be among the factors explaining the higher reactivity of O atoms in β-phase compared to γ-phase.

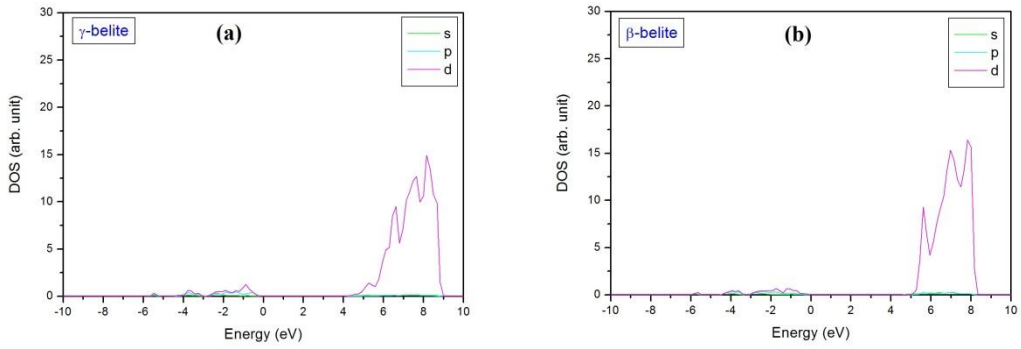

Fig.4. 4 : Partial DOS of Calcium with orbital contributions of (a) γ-belite and (b) β-belite.

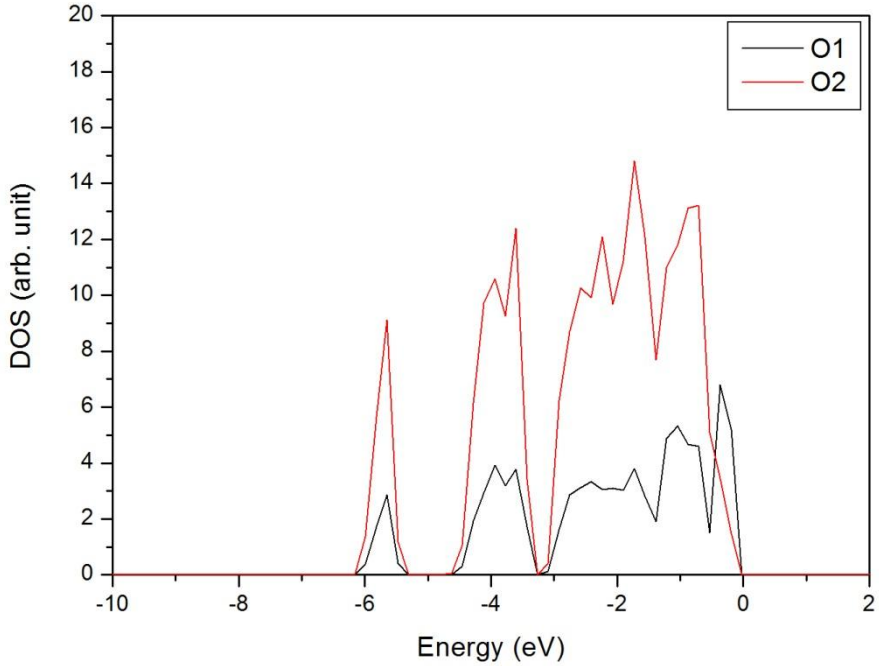

Fig.4. 5: Partial DOS of O1 and O2 oxygen types in β-belite.

For a deeper understanding of the reactivity of belite phases, the local reactivity can be also qualitatively analysed by comparing the plotted local density of states (LDOS) of Conduction bottom Minimum (CBM) and Valence Band Maximum (VBM) in Fig.4.6 and Fig.4.7 respectively. This analysis uses Fukui function as a local reactivity descriptor based on the

frontier orbital theory [140]. Note that VBM and CBM characterize the exposed areas to electrons loss and electrons gain respectively. VBM and CBM provide information of the reactive regions under electrophilic and nucleophlic attacks. The LDOS of CBM in Fig.4.6 is delocalized for both phases. Therefore, no peculiar reactive sites to nucleophilic attacks can be deduced from this analysis even though the CBM LDOS is distributed differently comparing γ- and β-belite. It is mainly dispersed in the regions between Ca and SiO_4 polyhedral in β belite; whereas it is symmetrically dispersed in the space between calcium atoms (Ca2-Ca4 and Ca1-Ca3) in γ-belite. On the other hand, the plotted VBM in Fig.4.7 shows that both LDOS are localised around the Oxygen atoms and thus more likely to undergo electrophilic attacks in agreement with the previous DOS analysis. However, we can see that LDOS is highly localised around few oxygen atoms (O1-type) in β-belite whereas the VBM LDOS is shared between most oxygen atoms in γ-belite. This finding is in consistency with the closest most occupied energy levels to the Femi level by O1-2p states in DOS of β-belite, confirming the higher reactivity of O1-type oxygen atoms in β-belite, which may explain the enormous difference in the water reactivity between γ-belite and β-belite.

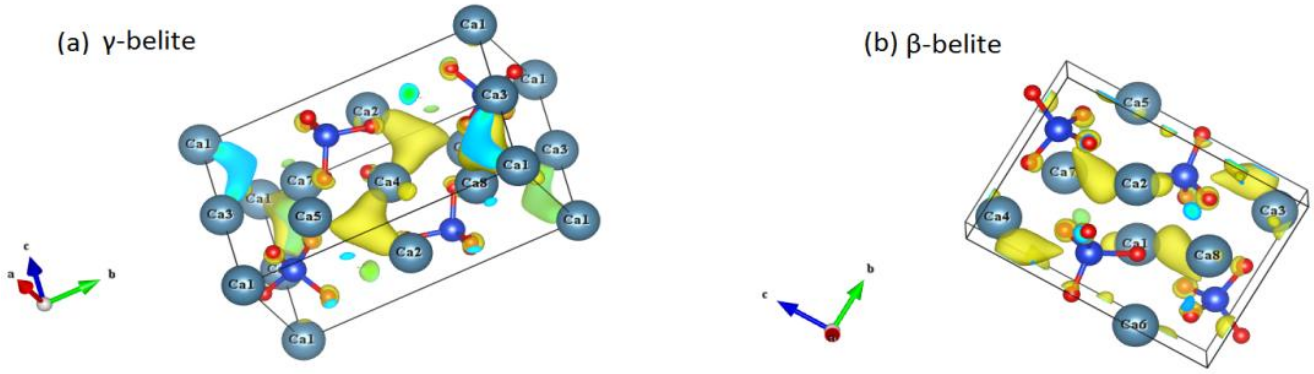

Fig.4. 6: LDOS of CBM of (a) γ-belite and (b) β-belite.

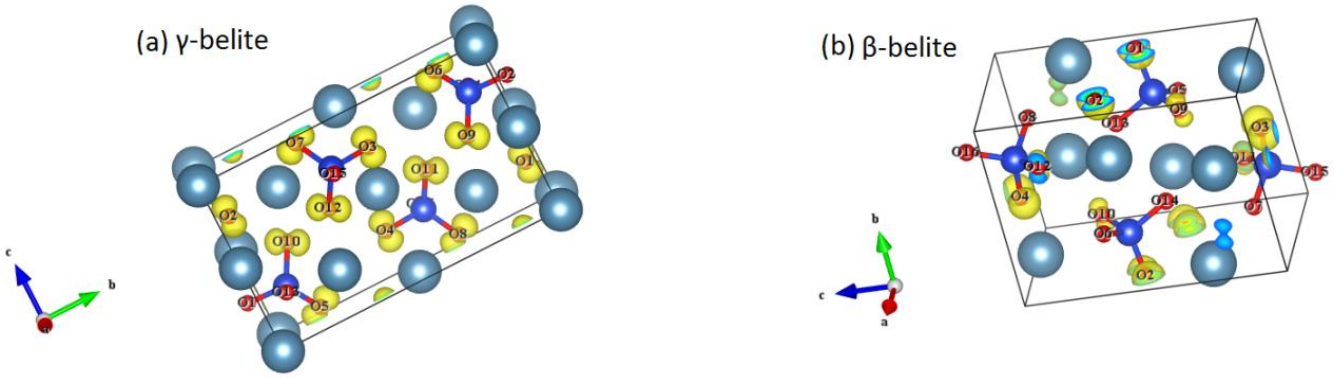

Fig.4. 7: LDOS of VBM of (a) γ-belite and (b) β-belite.

To get more insights into the chemical bonding and the charge transfer in each phase, we have plotted the charge density in Fig.4.8 and the 2D-map in Fig.4.9 in planes containing the three types of atom (Si, Ca and O) that we named P_g and P_b plane for γ-phase and β-phase respectively. We see that Silicon atoms are tightly bounded to the closest oxygen atoms in both phases. The strong projected charge density between the oxygen and silicon ions indicates the strong covalent bonding character. On the other hand, the charge density is not quite important between calcium and oxygen ions confirming again the high ionic character of Ca-O bond in γ-phase the two belite phases. Fig.4.9 reveals however a significant difference regarding the charge density distribution over the oxygen atoms. Fig.4.9.a shows a uniform distribution of the electron density over the four oxygen atoms in γ-belite whereas an asymmetric electronic density on the O1-Ca1-O11 pairs in β –belite as shown in Fig.4.9.b The non-uniform electron density distribution in P_b plane where the calcium atom is coordinated to O1 and O2 oxygen types is consistent with the bader charge analysis and LDOS localization confirming the different electronic environments around the two types of oxygen. Thus, our analysis suggests that the high reactivity of β-belite is due to the electron transfer from calcium atoms to the reactive oxygen atoms of O1-type in β-belite that undergo electrophilic attacks from water (of type H+) in the hydration process.

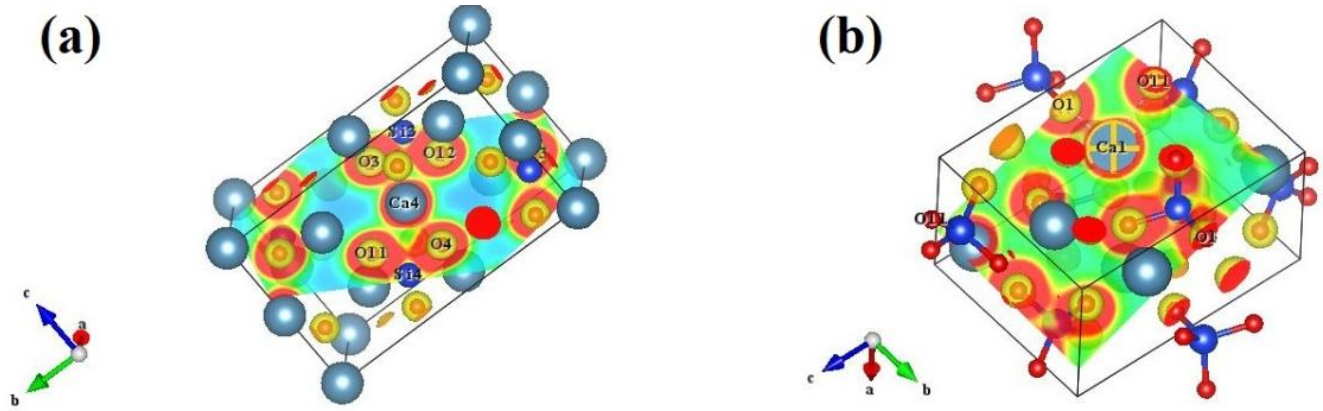

Fig.4. 8: Charge density of (a) γ-belite and (b) β-belite.

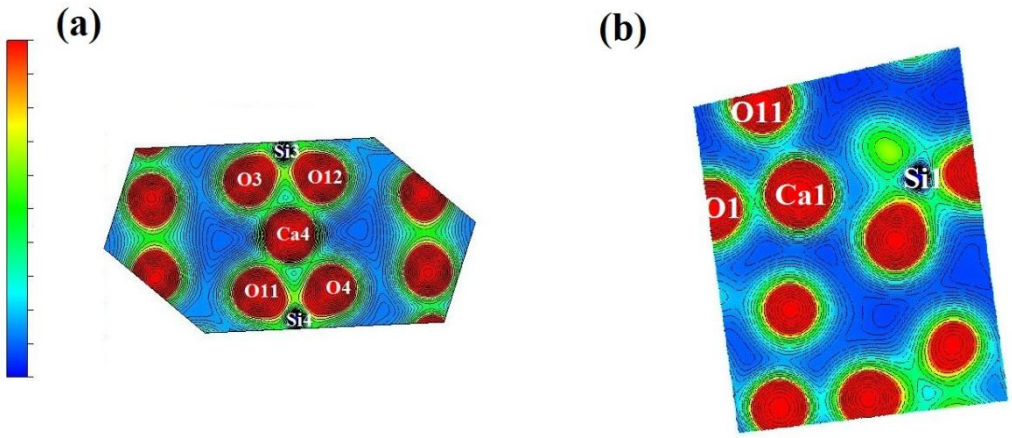

Fig.4. 9: Charge density map on the Pg of γ-belite and Pb plane of β-belite.

4.4. Conclusion

The main aim of this work was to determine and compare between structural, mechanical, bonding and electronic properties of γ- and β-belite by means of DFT calculations. The calculated structural and mechanical properties by GGA functional were found to be in great agreement with the experiment. Comparable elastic parameters and moduli were obtained for γ- and β-belite with slightly higher values for γ-belite predicting that γ-phase is insignificantly more rigid and resistant. On the other hand, the analysis of chemical bonding and electronic properties of the two phases reveals relevant distinctions that may explain the stability of γ-belite and the reactivity of β-belite in the hydration process. In β-belite, two oxygen atoms types (O1 and O2) were distinguished by analyzing the atomic charges and the most occupied energy levels near the Fermi level in the PDOS of O-2p states, whereas γ-belite exhibits a

high symmetry in the charge distribution over all oxygen atoms. The uniformly distributed LDOS of VBM may also explain the non-reactivity to water of γ-belite; while the highly located LDOS of VBM around O1-type oxygen atoms indicates high reactivity under electrophilic attacks. Many theoretical works attempted to introduce impurities to enhance the β-belite reactivity rate. By analogy with the localized nature of VBM around O1-type, localizing the CBM LDOS around some specific Calcium atoms by doping mechanisms would efficiently increase the reactivity of β-belite under nucleophilic attacks, and thus the overall reactivity with water.

Chapter 5: Molecular Dynamics study of C-S-H

5.1. Introduction

In this chapter, we will investigate the structural and mechanical properties of the recent realistic model by Bauchy et al. [73]. In order to provide nanoscale information about the crack propagation and rupture mechanism in cement based materials, a particular attention was paid to the characterization of the mechanical response of C-S-H to tensile loading by studying the elastic, plastic and failure behaviors. Recently, Mechanical properties have been determined using several realistic C-S-H models [28,167] by molecular dynamics approach. However, only elastic behavior was considered to study the mechanical reponse of C-S-H. Few MD works have studied the mechanical behavior of C-S-H beyond the elastic limit. Murray el al. [168] calculated tensile and compressive strengths along the perpendicular axis to the calcium-silicate chains of C-S-H and concluded that the tensile strength is only 23% of the compressive strength. Nevertheless, no atomic scale studies based on recent C-S-H realistic models have been conducted to characterize the mechanical behavior up to the failure point.

C-S-H realistic atomic model:

Using molecular simulations, many authors developed several models of C-S-H that agree the most with the experiment results and correctly predict the C-S-H properties. The realistic model of C-S-H $((CaO)_{1.65}(SiO_2)(H_2O)_{1.75})$ by Pellenq et al. [71] was constructed in order to provide values of C/S ratio and density close to those by neutron scattering measurements (C/S=1.7 and d=2.6 g/m^3). Many posterior works used the Pellenq model of C-S-H to describe the C-S-H structure at the nanoscale. Manzano et al. [74] used the C-S-H realistic model by Pellenq. et al. to study the mechanism of water dissociation to hydroxyl groups in the micropores of C-S-H using the REAXFF reactive force field [28] and the influence that it has on the structural and mechanical properties. Manzano et al. calculated the elastic tensor of C-S-H and compared the deduced mechanical properties of C-S-H before and after water dissociation. Unlike most silicates that manifest a "hydrolytic weakening" effect [169], the presence of water has a hardening effect since it reacts with the silicate chains transforming the layered two-dimensional like structure of C-S-H to a three dimensional like structure. Bauchy el al. [73] also developed the realistic model described by Pellenq el al. within the reactive forcefield REAXFF [170] parameterized by Manzano et al. that allows the water molecules to dissociate into hydroxyl to form Si-OH an Ca-OH groups to study the atomic

order in C-S-H. According to this study, an investigation of the atomic order of the C-S-H structure was carried out and C-S-H was described as an intermediate structure between a crystalline and an amorphous material.

Simulation Method

We prepared a 3x3x3 supercell composed of 13527 atoms based on the C-S-H model by Bauchy et al. [73] The system was simulated using REAXFF forcefield implemented in the Large-Scale Atomic/Molecular Massively Parallel Simulator (LAMMPS) [171] package. Manzano et al. extended the REAXFF capacity to perform calculation on calcium silicate systems by the parameterization of the Ca-O/H interactions within the reactive force field [172]. Timestep was set to 0.25 fs and the structure was relaxed in the NPT ensemble at 300 K and zero external pressure for 2.5 ns until the convergence of energy and lattice parameters was achieved. The lattice parameters of the relaxed triclinic box are: a=39.00 Å, b=57.28 Å, c=71.90 Å. α=91.60°, β=91.72°, γ=88.35°. The atomic structure of C-S-H is displayed in Fig.5.1.

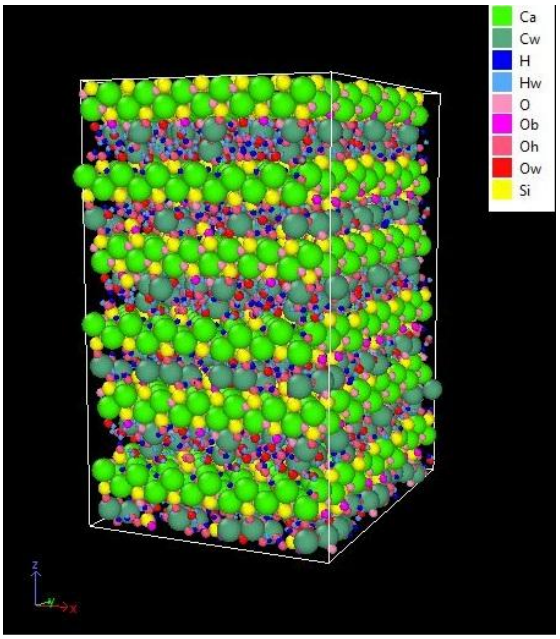

Fig.5. 1: The atomic structure of C-S-H.

5.2. Structural properties

We analyzed the radial distribution function (RDF) or g(r) that is defined as the probability of finding a particle is a shell dr at a distance r from another particle chosen as a reference. The total RDF g(r) is given by:

$$g(r) = \frac{V}{N}\frac{dn(r)}{dV(r)} \quad (5.1)$$

Where dn(r) is the number of atoms between r and r+dr from a given atom, dV(R) is the shell volume between r and r+dr that can be approximated as $4\pi r^2$, N is the total number of atoms and V is the volume of the simulation box.

The total RDF can be considered as the contribution of all pair correlation functions $g_{AB}(r)$ between any two atom types A and B of the system. The partial RDF $g_{AB}(r)$ between particles of types A and B, defined as the probability of finding a neighbor atom of B type of an atom of A type at a distance r, can be computed as follows:

$$g_{AB}(r) = \frac{V}{N_A}\frac{dn_{AB}(r)}{dV(r)} \quad (5.2)$$

Where $dn_{AB}(r) = \sum_{i\in A}\sum_{j\in B}\delta(r_{ij} - r)$ is the number of atoms B located at a distance r from an atom A and N_A is the number of atoms of A type. Finally, the Atomic contribution of A type to RDF $g_A(r)$ is defined as the partial $g_{A\text{-}X}(r)$ between particles of A type and any other particle of X type in the system.

We plot in Fig.5.2.a the radial distribution function g(r). Five peaks of RDF are situated in the 0.99 Å, 1.51 Å, 1.62 Å, 2.23 Å and 2.65 Å regions were observed. The first and third peaks situated in the 0.99 Å and 1.62 Å regions respectively are quite high and sharp compared to the second and the two last peaks that are much lower. To investigate the origin of these peaks, we plot the contributions of the species of the system to RDF. Nine labels are used to distinguish between the local environments of the atoms. The Oxygen atoms are classified in four categories: Ow refer to oxygen of the water molecules, Oh are oxygen atoms of the hydroxyl groups, Ob are the bonding oxygen atoms in the Silica chains and O are the non-bridging oxygen atoms in the silica/calcium layers. We also make difference between two Calcium types: Ca is the intralayer calcium and Cw is the interlayer calcium. Finally the hydrogen atoms have two types: The Hw atoms in the water molecules and H atoms in the

hydroxyl groups. We see from Fig.5.2.b that the first sharp peak situated in the 0.99 Å region is mainly due to the water and hydroxyl groups atoms (Ow, Hw, O and H). The second peak situated in the 1.51 Å is much shorter and is fully due to Hw atoms contribution. The third peak at 1.62 Å is due to Si atoms as well as the oxygen atoms O, Ob and Oh. The Fourth peak in the 2.23 Å region is dominated by both calcium types Ca and Cw contributions and the rest of the atoms with smaller contributions. The fifth peak at approximately 2.63 Å region is due mostly to Ob atoms and less significantly to Ca, O of the intralayer space and Cw, Ow and Oh atoms in the interlayer space.

Based on the information provided by the atoms contributions to RDF, we plot the partial radial distribution function (PRDF) of each pair of atoms spotted in each peak. Fig.5.3.a shows that the first peak is mainly due to Oh-H and Ow-Hw interactions with a mean bond length of 1 Å for both and coordination numbers of hydrogen atoms around oxygen atoms of 0.97 and 1.81 respectively within a sphere of 1.3 Å. The position of this first peak was also found by Manzano et al. [74] by both DFT and MD simulations. The second peak is fully due to Hw-Hw correlation with a coordination number of 0.98 within a sphere of 1.6 Å as illustrated in Fig.5.3.b while the third peak at 1.62Å is due to Si-O Si-Oh and Si-Ob interactions (see Fig.5.3.c) With coordination numbers of oxygen atoms around Si atom of about 2.21, 1.08 and 0.7 respectively within a sphere of 2.5Å. Bauchy et al. also found that the first peak in the 0.99 Å region is due H-O bonds. However, only a second peak in the 1.6 Å, associated with a superposition of both H-H and Si-O correlations, was spotted. The rest of peaks were not distinguishable. Here, we see that the Hw-Hw interactions result in an intermediate peak at 1.51 Å region while the peak in the 1.62 Å region is mainly due to correlations between Si and Oxygen atoms.

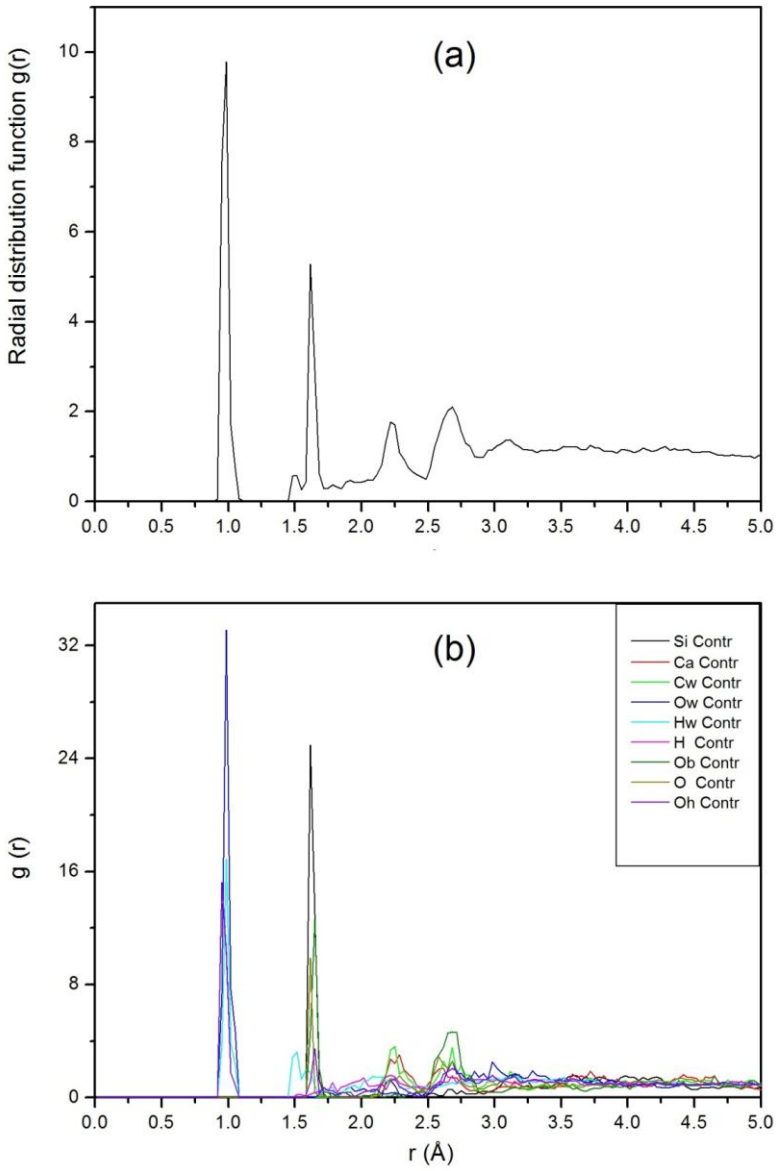

Fig.5. 2: (a) Radial pair distribution functions of C-S-H. (b) Contribution of pair interactions to RDF.

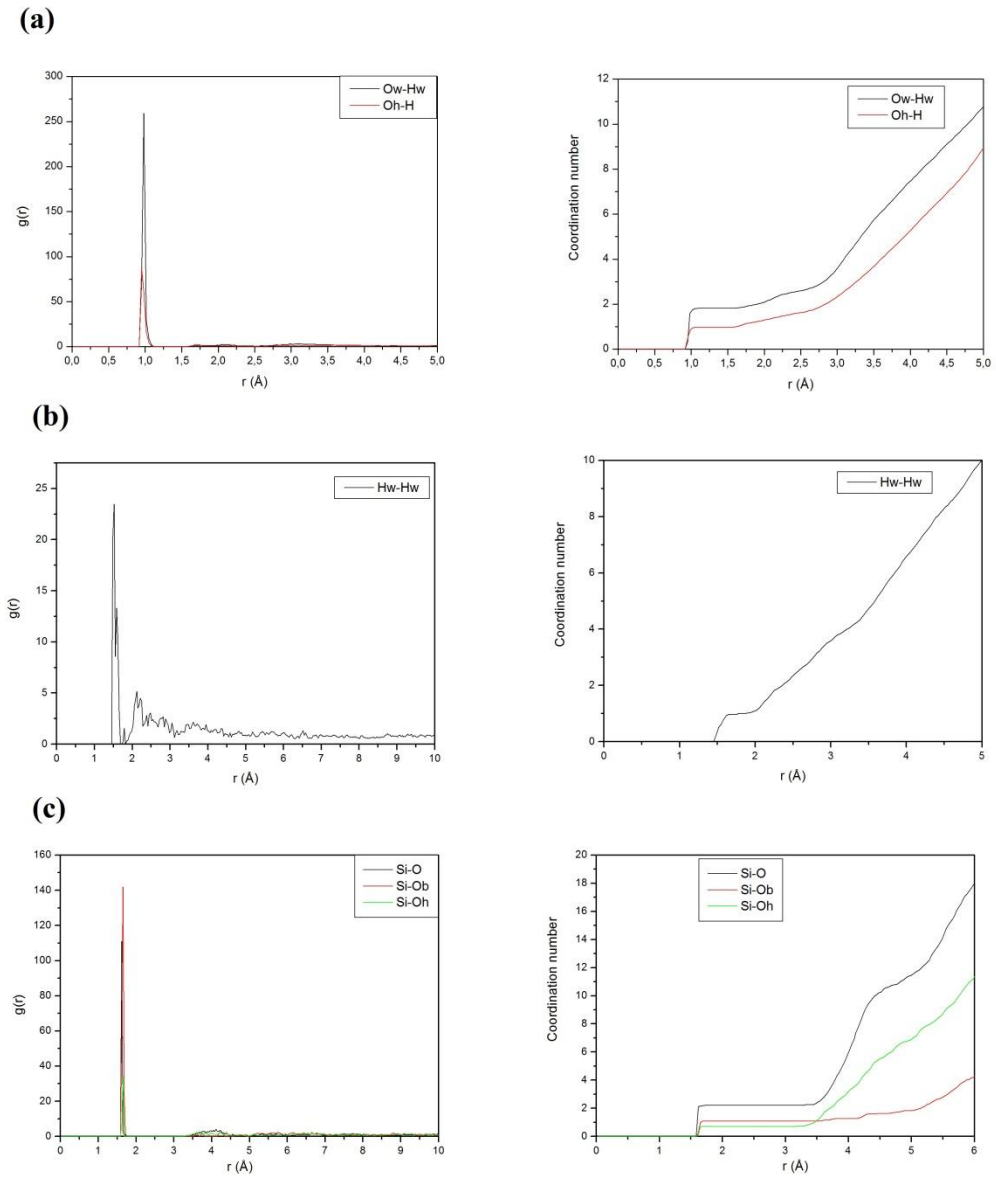

Fig.5. 3: Radial distribution function and coordination number of (a) H-Oh and Hw-Oh interactions. (b) Hw-Hw interaction. (c) Si-O Si-Oh and Si-Ob interactions.

Fig.5.4 shows that the peak situated in the 2.23 Å region is mainly due to Ca-O interactions in the intralayer as well as the Cw-Oh interactions in the interlayer while the last peak in the 2.65 Å is mainly due to the Ob-O, Ob-Ob and Cw-Ow interactions with a smaller contribution of Cw-Oh interactions. Manzano et al. also found a peak at approximately 2.6Å by calculating partial RDF of Ca-O. However, no precisions were given about the oxygen types that contribute the most to this peak. Moreover, we can see from Fig.5.4.a that the highest coordination number of about 5.0 was calculated for O atoms around intralayer Calcium atoms Ca suggesting a dominant geometry of 5 O-type oxygen atoms around Ca within a sphere of 3 Å in the intralayer space. On the other hand, Fig.5.4.b shows that the oxygen

atoms around the interlayer calcium atoms Cw oxygen within a 3.0Å sphere are mostly Oh oxygen-type with a coordination number Cw—Oh of 3.5. In addition, Oxygen atoms of Ow and O types are also found around Cw atoms within a 3.0Å sphere with a coordination number of about 1.33 for both Cw—Ow and Cw—O . Finally, The Ob atoms are mainly surrounded by O-type oxygen atoms and less significantly by Ob-type atoms with coordination numbers of 4.0 and 0.92 for Ob—O and Ob-Ob respectively as shown in Fig.5.4.c.

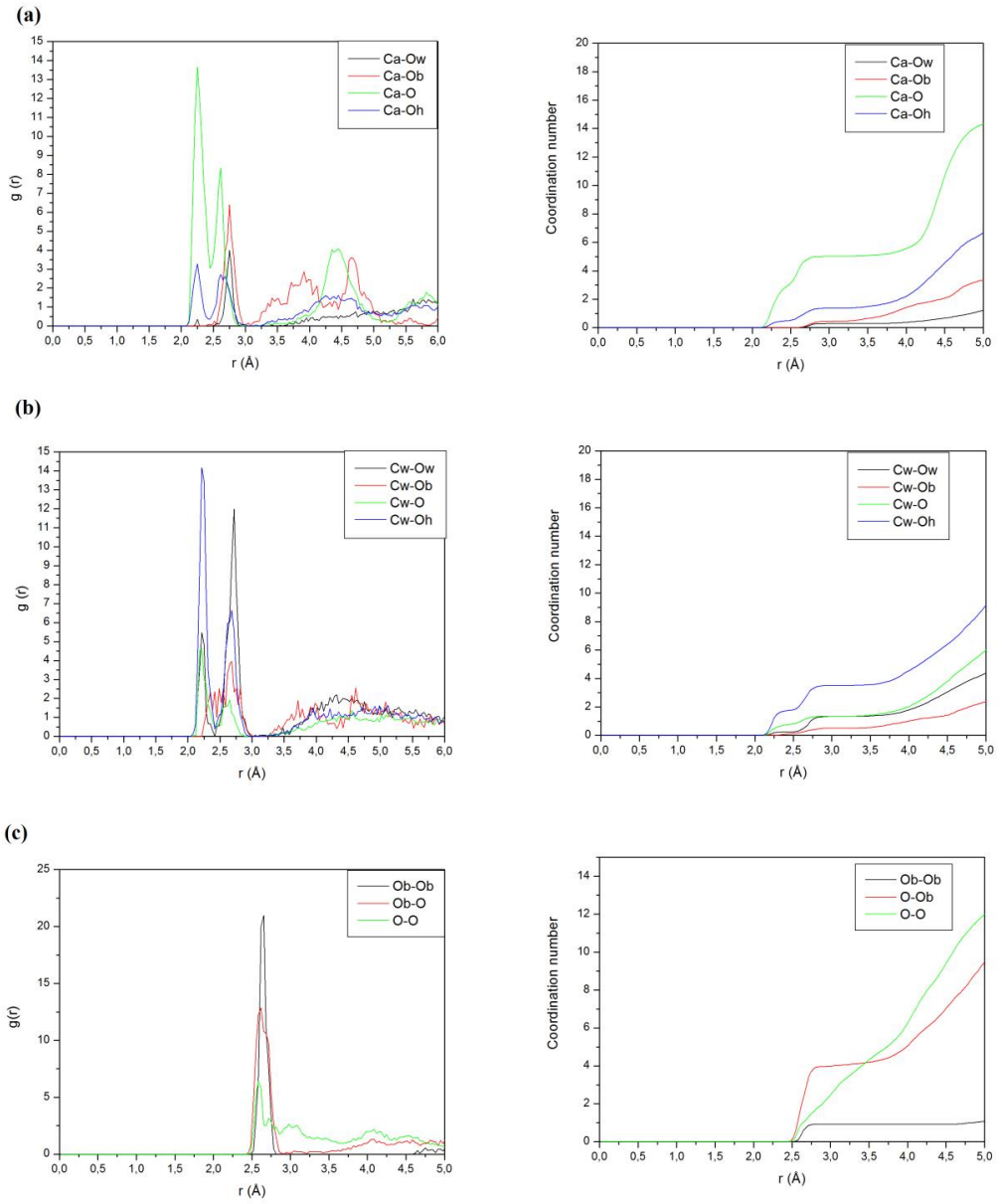

Fig.5. 4: Radial distribution function and coordination number of (a) Ca and oxygen interactions. (b) Cw and Oxygen interactions. (c) Ob-O Ob-O and O-O interactions.

5.3. Mechanical properties:

After equilibrating the system, uniaxial strain (X, Y and Z) and shear strain (XZ, YZ and XZ) were applied with an engineering strain rate of $0.007ps^{-1}$ in the NVT ensemble and the corresponding stresses are calculated. The linear part of the stress-strain response enables to calculate the 21 independent elastic constants Cij that we compared to other Molecular Dynamics (MD) works in table 5.1. The calculated values of Cij are close to those found by previous MD works with an average difference of 5.6% in comparison with the Cij values by Pellenq et al. [71]. Although different geometries and interatomic potentials were used in the mentioned MD works, values of the calculated elastic constants are quite comparable. We see that C_{11} and C_{22} values are higher than C_{33} value indicating that the system is more resistant in the XY plane corresponding to the silicate layers. From the elastic tensor, we calculated the bulk (K) and shear (G) moduli according to the Voight-Reuss-Hill (VRH) bounds [131]. The equivalent isotropic Young's modulus (E), Poisson ratio (ν) and indentation modulus (M) were derived from K and G using the formulas:

$$E = \frac{1}{\frac{1}{3G}+\frac{1}{9K}} \qquad (5.3)$$

$$\nu = \frac{1}{2}\left(1 - \frac{3G}{3K+G}\right) \qquad (5.4)$$

$$M = 4G.\frac{3K+G}{3K+4G} \qquad (5.5)$$

Table 5.1: Calculated elastic constants in comparison with other MD works

	This work (REAXFF)	MD (Pellenq et al) [71]	MD (Manzano et al.) [74]
C_{11} (GPa)	85.74	93.5	90.9
C_{22}(GPa)	83.18	94.9	91.7
C_{33}(GPa)	67.80	68.5	72.6
C_{44}(GPa)	19.04	19.2	21.4
C_{55}(GPa)	18.72	16.1	21
C_{66}(GPa)	31.27	31.2	28.6
C_{12}(GPa)	45.31	45.4	33.1
C_{13}(GPa)	26.49	26.1	30
C_{23}(GPa)	27.01	30.01	29.6

Table 5.2: Calculated Bulk modulus (K), shear modulus (G), Young's modulus (E), Poisson's ratio (ν) and indentation modulus (M)

	This work (REAXFF)	MD (Pellenq et al.) [7]	MD (Manzano et al.) [8]
K (GPa)	47.39	47 - 51	48.6
G (GPa)	22.45	22 - 24	24.7
E (GPa)	58,16	66 - 55	74 - 58.3
v	0.3	0.3	0.28
M (GPa)	63.72	65	69

The calculated elastic properties are summarized in Table 5.2 against other MD works. Our results are very close to those found by Pellenq et al. and Manzano et al. Moreover, we can also compare with the experiment by calculating the indentations modulus (M) that can be determined by nanoindentation measurements. The found value 63.7 GPa is in great agreement with that by nanoindentation 65 GPa. [173]

5.4. Crack propagation:

Shrinkage crack in cement materials is greatly related to tensile strength. The crack potential gets more important as the tensile strength decreases In order to investigate the tension strength of the system in the x, y and z directions, the stress evolution with respect to tensile strain in the x, y and z directions is plotted in Fig.5.5 The stress of the entire systems of atoms is given by the following formula:

$$S = -\frac{NK_BT}{V} - \frac{\sum_i^N r_i . f_i}{d . V} \quad (5.6)$$

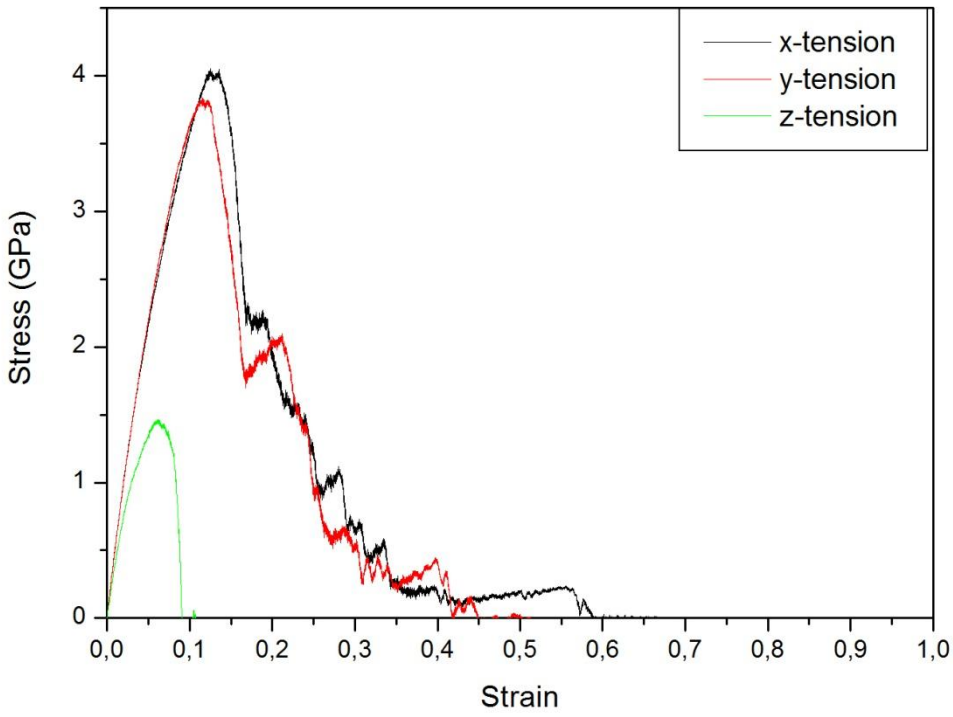

Fig.5. 5: Stress-strain relationships for tension along x, y and z axes.

Where N is number of atoms, K is Boltzmann constant, T is temperature, d is dimensionality of the system, and V is volume. ri and fi are respectively the position and force vector of atom i.

In x and y directions, Stress evolution is very similar. Stress rapidly increases with strain in the elastic phase that ends at 0.03 Å/Å strain approximately. The ultimate strength in the x direction (4.05 GPa) is slightly higher than the y direction (3.85 GPa) corresponding to 0.13 Å/Å and 0.11 Å/Å respectively. Then, the stress slowly decreases in the plastic phase. The slow decreasing of the stress in the plastic phase is an indicator of the ductile behavior in the x and y directions.

In the z direction, the response to tensile is quite different. Stress increases in the elastic phase as strain increases up to 0.02 Å/Å strain. Subsequently, the stress continues to increase up to an ultimate strength of 1.46 GPa at 0.06 A/A strain. Then, the stress sharply decreases to zero at 0.09 Å/Å strain indicating a brittle behavior of the system in the z direction.

Understanding the fracture mechanism generated by tensile is important to improve the durability of cement materials. Therefore, we investigated the C-S-H system response to tensile in x, y and z directions. The relaxed structure is slowly elongated in the desired direction up to 70%. The intermediate configurations are recorded all along the process in order to spot first defects and cracks in the structure and to follow up the crack propagation.

5.4.1. Tensile along x axis:

With a tensile loading along the x direction, Fig.5.6a shows initial small defects in the interlayer regions at 0.17 Å/Å strain soon after reaching the yield point. As long as strain increases, the interlayer defects grow and form visible cracks in the structure as shown in Fig.5.6.b. Then, calcium atoms and silicate chains nearby the cracks dissociate leading to crack overlapping the structure as shown in Fig.5.6.c. In Fig.6d corresponding to 0.63 Å/Å strain, cracks continue to grow and overlap in the +/- 45° direction and tend to form one larger crack indicating the rupture of the structure.

These results are very similar to those found by D.Hou et al who studied the fracture mechanism of C-S-H in presence of nano-voids. However, the crack propagation is significantly slower compared to D.Hou results [174]. The crack propagation rate is highly affected by the present void in D.Hou [174] simulation. The present void localized in the center of the box also influences the crack initiation that was located near the central void, while the crack was initiated in the interlayer regions in the case of our study. However, the present void in C-S-H didn’t affect the direction of the crack propagation that was found to be the same (+/- 45° from x axis). Moreover, the cup-and-cone failure surface at the end of the tension simulation (Fig.5.6.d) is also observed in both studies confirming the ductile failure feature of C-S-H.

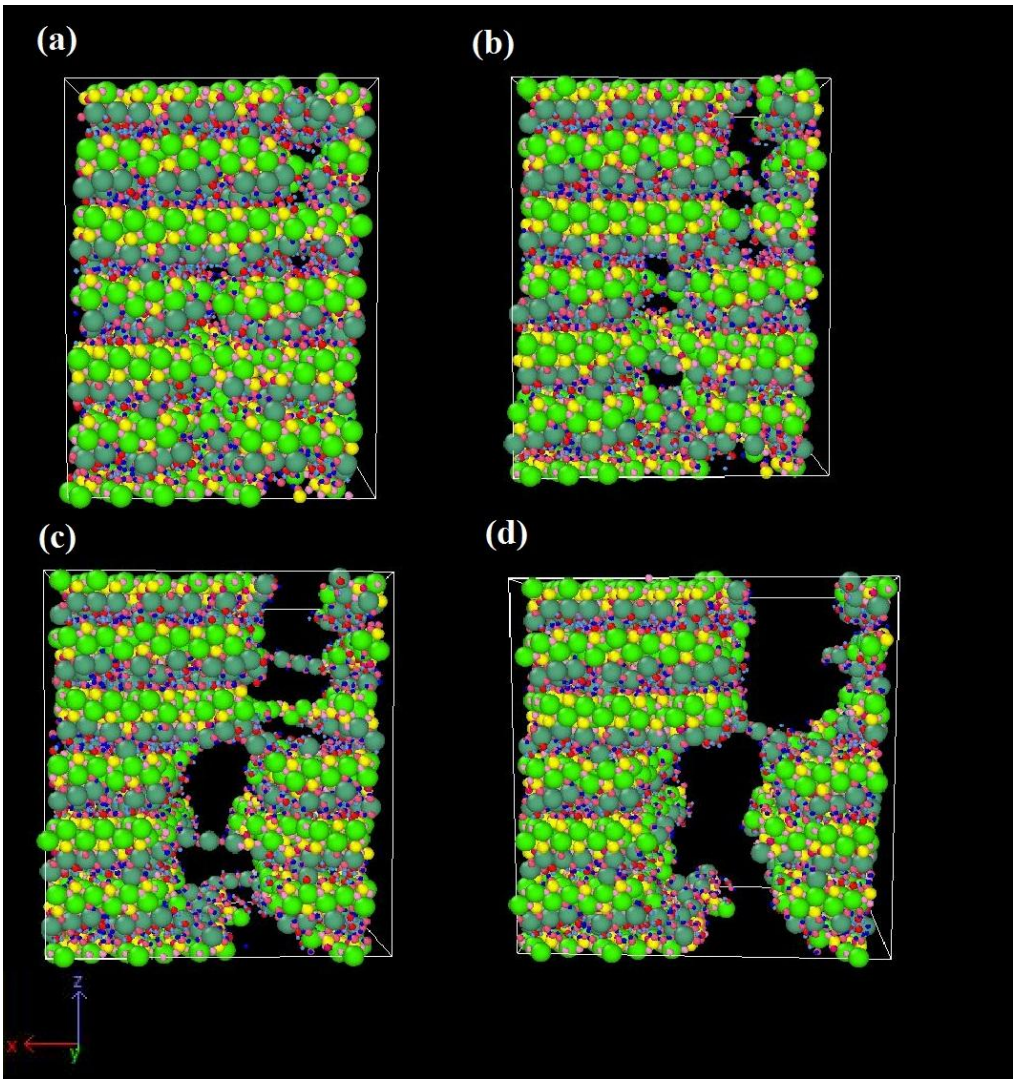

Fig.5. 6: C-S-H tensioned along x axis at (a) 0.17 Å/Å strain, (b) 0.30 Å/Å strain, (c) 0.50 Å/Å strain, (d) 0.6 Å/Å strain

5.4.2. Tensile along y axis:

Fig.5.7 shows the crack propagation of the structure elongated in the y direction. Small defects are initialized in the interlayer regions right after the yield point as shown in Fig.5.7.a corresponding to 0.14 Å/Å strain. Initial defects grow to bigger cracks as we can see at 0.19 Å/Å deformation stage (Fig.7.5.b). This deformation stage corresponds to the rapid stress reducing after reaching the yield point in the stress-strain curve (Fig.5.5). Then, the interlayer cracks propagate into the neighboring calcium silicate chains as shown in Fig.5.7.c corresponding to 0.34 Å/Å strain. The interlayer calcium atoms Cw attempt to reconstruct the calcium silicate chains by bridging the fractured parts. This explains the slight stress increase at 0.2 Å/Å strain and the slow-down of the stress decreasing rate afterwards in the stress-strain evolution. The crack propagation mode is very similar to that of x tension. The crack

grow along a direction of +/-45° from y axis and overlap to form a larger crack as strain increases from 0.34 Å/Å to 0.48 Å/Å as we can see in Fig.5.7.d. As in the case of tension along x axis, the rupture surface exhibits a cup-and-cone geometry indicating a ductile failure of C-S-H in the y direction.

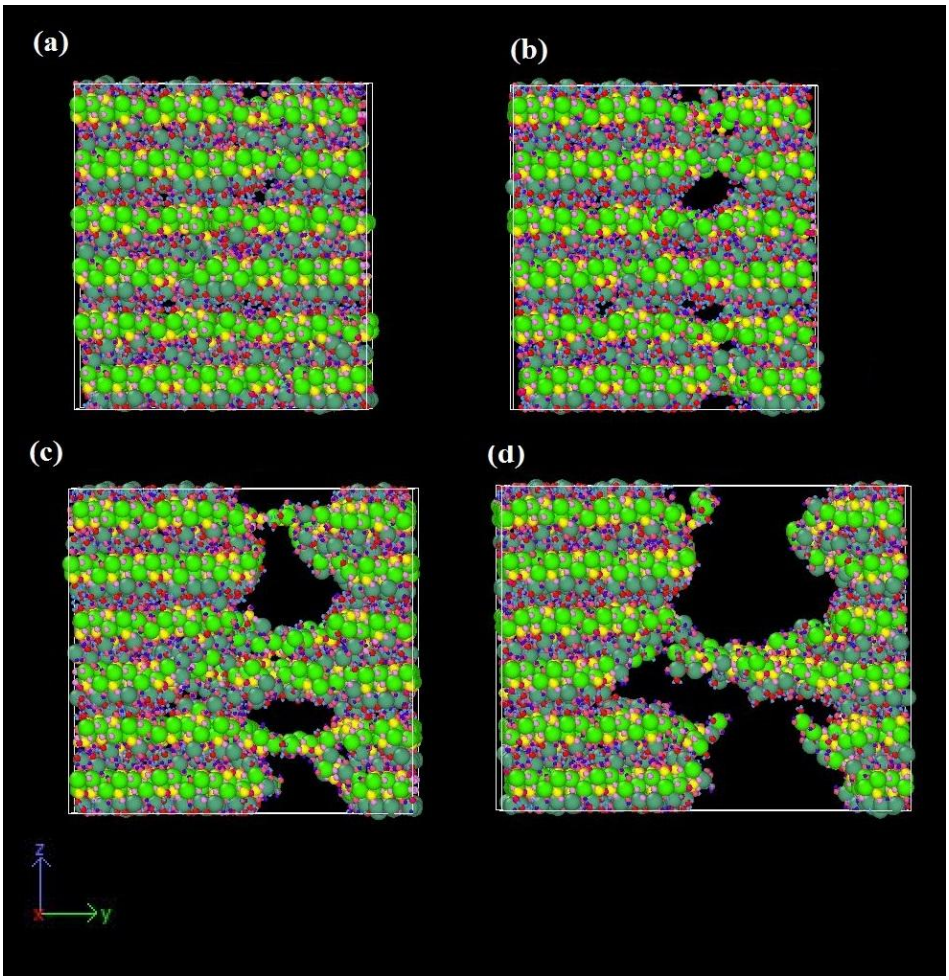

Fig.5. 7: C-S-H tensioned along y axis at (a) 0.14 Å/Å strain, (b) 0.19 Å/Å strain, (c) 0.34 Å/Å strain, (d) 0.48 Å/Å strain

5.4.3. Tensile along z axis :

The response of C-S-H to a tension along the z direction is illustrated in Fig.5.8. The defects are visible in the interlayer regions as soon as the strain reaches a value of only 0.063 Å/Å as shown in Fig.5.8.a. Many small defects can be seen in the same level of the interlayer region. As strain increases from 0.063 Å/Å to 0.09 Å/Å, the initial cracks grow very fast in the interlayer region as can see from Fig.5.8.b. At only 0.15 Å/Å tensile strain (fig.5.8.c), the box is almost separated in two halves that continue to move away from each other as strain increases as shown in Fig.5.8.d. The rate of the crack propagation and the rupture surface

geometry demonstrate the brittle behavior of the C-S-H system along the z direction. The "catastrophic" rupture mode along the z direction was also observed by D.Hou et al. [174].

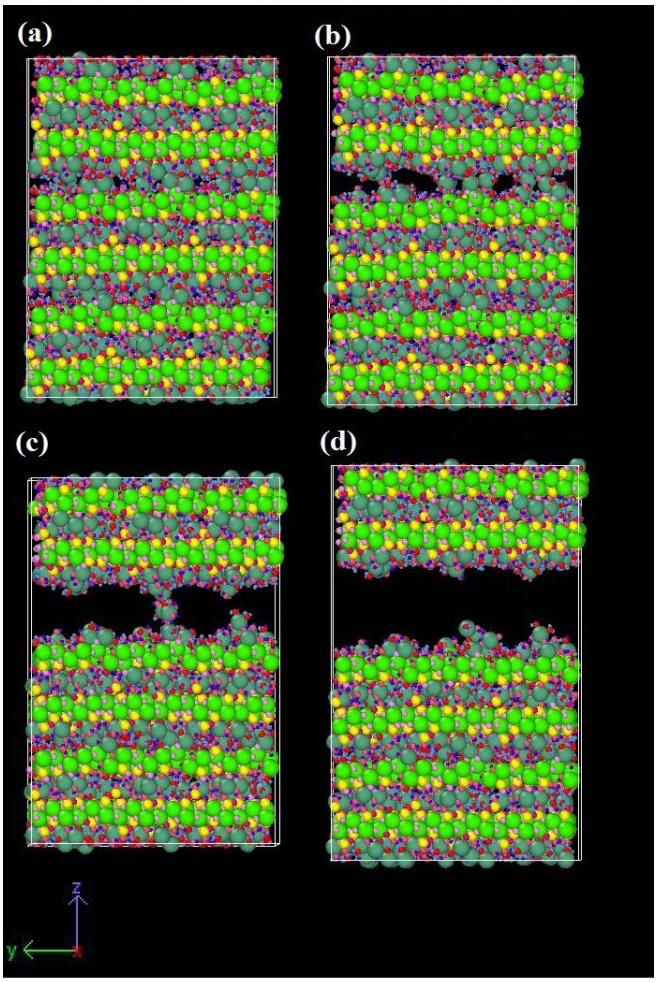

Fig.5. 8: C-S-H tensioned along z axis at (a) 0.063 Å/Å strain, (b) 0.09 Å/Å strain, (c) 0.15 Å/Å strain, (d) 0.24 Å/Å strain.

5.5. Conclusion:

In this work, the structural and mechanical properties of C-S-H have been studied using MD methods. The realistic model of C-S-H was used to describe the C-S-H system and the structure of C-S-H was investigated. The contributions of pair interactions to the main peaks of the RDF were determined and coordination between atoms was studied. Elastic properties were evaluated using Stress-Strain relationship. The crack propagation was observed and the fracture mechanism was investigated. According to the rupture modes, C-S-H exhibits a ductile behavior in the x and y directions while the catastrophic rupture mode shows the brittle behavior of C-S-H in the z direction.

Chapter 6: Nano-modified Calcium-silicate-hydrates by Fe_2O_3 nanoparticles.

6.1. Introduction

In this chapter, we provide an analysis on the molecular scale of the structural and mechanical strengthening of modified Calcium Silicate Hydrates (C-S-H) by embedding Fe_2O_3 nanoparticles. The nanoparticles size dependency of both interaction energy and bonding mechanism has been studied. Many systems of modified C-S-H by Fe2O3 nanoparticles with sizes ranging from 2.1nm to 3.0nm were studied and the corresponding structural and mechanical properties were derived. Finally, the molecular structure evolution under tensile loading was examined in order to characterize the fracture mechanism of the nano-Fe_2O_3/C-S-H.

6.2. Methods

6.2.1. C-S-H model:

We use the same C-S-H model as in chapter 5. More details about the model construction can be found in the literature [73,175,176].

6.2.2. Fe_2O_3 Nanoparticles:

The Fe_2O_3 nanoparticles were spherically carved from a large bulk Hematite α-Fe_2O_3 material. The α-Fe_2O_3 crystal information was found by Blake et al. [177] using X-ray methods. Under the condition of stoichiometry, some surface atoms were added and charges were rescaled using Electronegativity Equalization Method (EEM) [178]. The annealing procedure was then used to allow the surface atoms to find the best positions. Finally, the nanoparticles were relaxed in the NPT ensemble at 300 K and zero external pressure. Six nanoparticles with different sizes ranging from 1.9nm to 3.0nm were used in order to study the size effect of the inserted nanoparticles in the C-S-H matrix as shown in Fig.6.1.

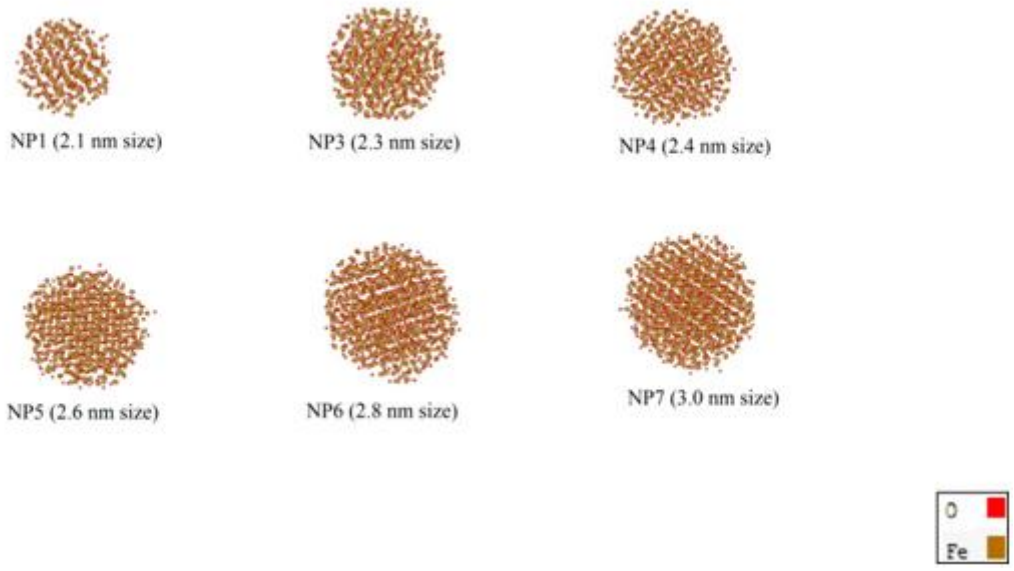

Fig.6. 1: Fe_2O_3 nanoparticles with six different sizes

6.2.3. Force Fields:

The REAXFF force field [28] was used to describe interactions between the C-S-H particles using the parametrization by Manzano et al. [172]. REAXFF was also selected for transferability issues and we used the parameterization by Aryanpour et al. [179] to describe interactions in the Fe_2O_3 system. The interactions between oxygen and hydrogen atoms from C-S-H matrix and atoms of the Fe_2O_3 nanoparticles were defined by the REAXFF parametrized by Aryanpour et al.. In addition, the interactions between Si and Ca atoms from C-S-H and Oxygen atoms from Fe_2O_3 nanoparticles were defined by REAXFF. Finally, Si--Fe and Ca--Fe short range interactions were defined by the Lennard-Jones potential parameterized by Rappé et al. [180]. This parameterization was also used by T.Wu et al. in order to study the properties of $CaO\text{-}SiO_2\text{-}Al_2O_3\text{-}FeO$ slags [181].

6.2.4. Computational cell:

A fully relaxed 3x3x3 Calcium-Silicate-Hydrates (C-S-H) triclinic supercell containing 13527 atoms with lattice parameters a=39.00 Å, b=54.23 Å, c=71.84 Å, α=89.92°, β=92.40° and γ=88.19°was used for C-S-H matrix (See Fig.6.2)

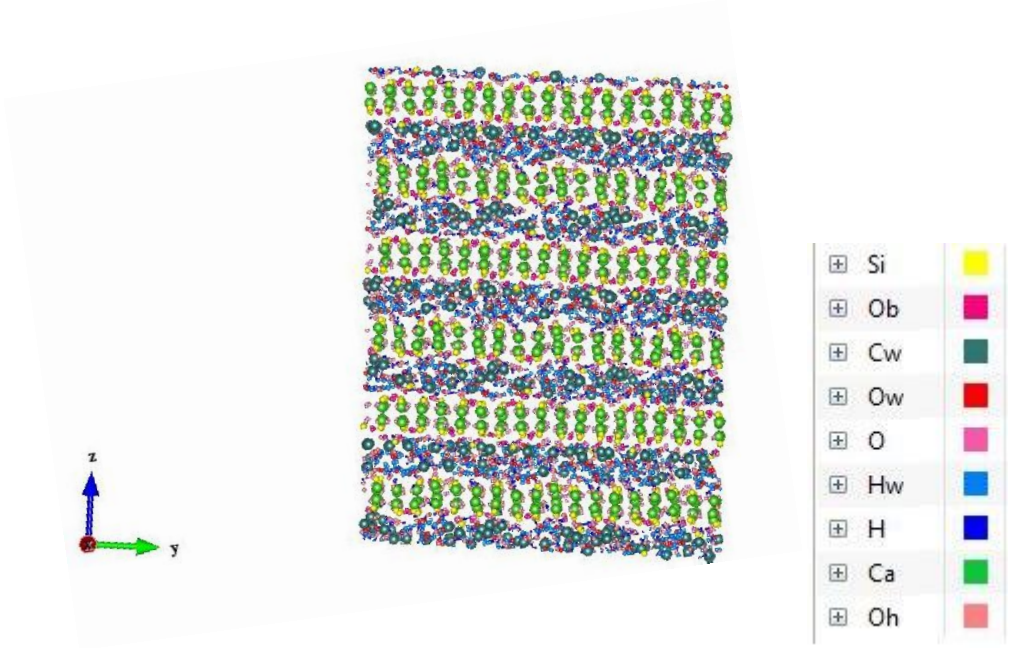

Fig.6. 2: C-S-H atomic structure

To incorporate the nanoparticle in the C-S-H matrix, a spherical hole was gradually indented in the center of the 3rd interlayer of the C-S-H structure by slightly pushing atoms backwards. Energy minimization was then performed on the resulted indented structures. Optimized C-S-H system with a 2.4nm hole is shown in Fig.6.3

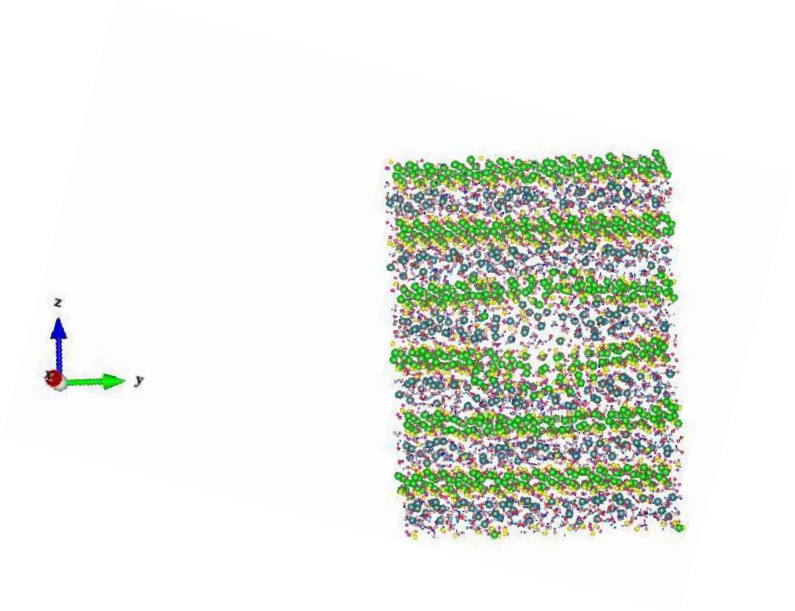

Fig.6. 3: (YZ) slice of the indented C-S-H with a hole size of 2.4nm.

For each nanoparticle, the hole size was selected to have the smallest possible value that results in favorable interactions between C-S-H and the inserted nanoparticle. A triclinic system with the periodic boundary conditions was used to describe the NP/C-S-H composites. Fig.6.4 presents the (XY) slice of C-S-H modified by NP2-type nanoparticle: NP2/C-S-H structure.

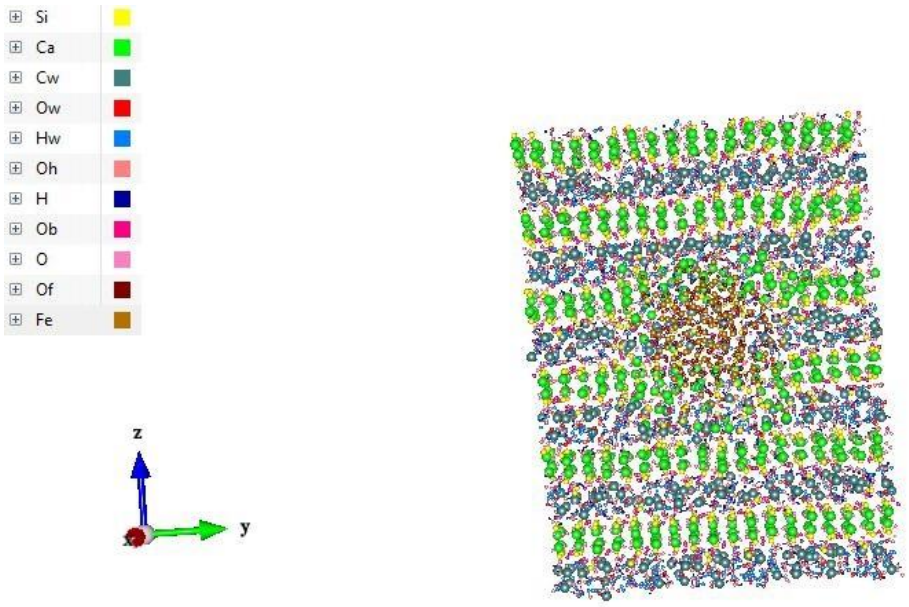

Fig.6. 4: (YZ) slice of the NP2/C-S-H structure.

For all the nanoparticles, the equilibrium void size between C-S-H matrix and the nanoparticle was found to be about 1.5 Å. After energy minimization, the six structures were relaxed in NPT ensemble at 300 K and zero pressure for about 2.5ns with 0.25 fs timestep in order to reach the equilibrium state. Then, a MD simulation of 200ps in NVT ensemble was performed for data collection. The Large-scale Atomic/Molecular Massively Parallel Simulator (LAMMPS) [171] was used for the molecular dynamics simulations.

We define the nanoparticle (filler) volume fraction ϕ in our simulations as

$$\phi = \frac{4\pi R^3}{3<V>N_n} \quad (6.1)$$

Where R is the nanoparticle radius, < V > is the total average volume of the nanocomposite simulation box during NPT simulation and Nn is the number of inserted nanoparticles in the simulation box. Volume fractions and the properties of the six inserted properties were summarized in Table 6.1.

Table 6.1 : Fe_2O_3 Nanoparticle sizes, number of atoms and Fe_2O_3/C-S-H volume ratio.

	size (nm)	Number of atoms	Volume fraction (%)
NP-1	2.07	405	1.7
NP-2	2.26	580	2.1
NP-3	2.39	710	2.5
NP-4	2.61	930	3.1
NP-5	2.81	1160	3.9
NP-6	2.98	1390	4.5

At the end of the equilibration process, the neighboring environment of Fe_2O_3 nanoparticles is modified. For instance, the atomic structure of the NP2-type nanoparticle and neighboring C-S-H atoms at the beginning and at the end of the hybrid structure relaxation is shown in Fig.6.5 We can see that at the end of the simulation, C-S-H atoms come closer to the nanoparticle surface and space between the nanoparticle and C-S-H is clearly reduced.

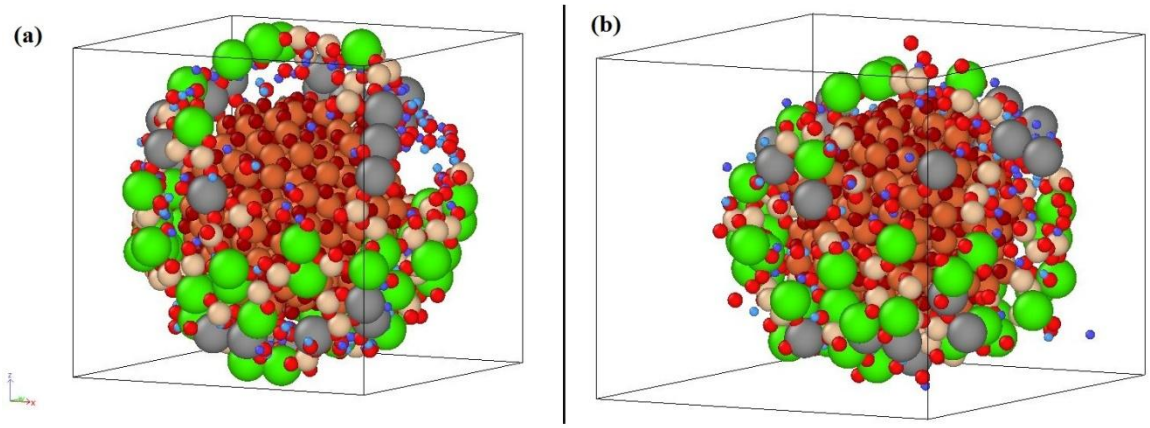

Fig.6. 5: C-S-H neighboring atoms of Fe_2O_3 NP2-type nanoparticle at: (a) The start of the structure relaxation. (b) The end of the structure relaxation.

6.3. Structural properties:

6.3.1. Total energy:

By choosing the smallest void size, structures were optimized and relaxed in room temperature conditions for about 2.5ns as shown in Fig.6.6. Then, the atomic energy of the C-S-H/Fe_2O_3 composite is plot as a function of the inserted nanoparticle size in Fig.6.7. We see that the total energy decreases as the nanoparticle size increases. The density convergence of each structure was also reached as illustrated in Fig.6.8. We see that the density slowly increases as the space between the C-S-H matrix and the nanoparticle is gradually filled during the relaxation. Finally, the density of the composite system is plot as a function of the inserted nanoparticle size in Fig.6.9.

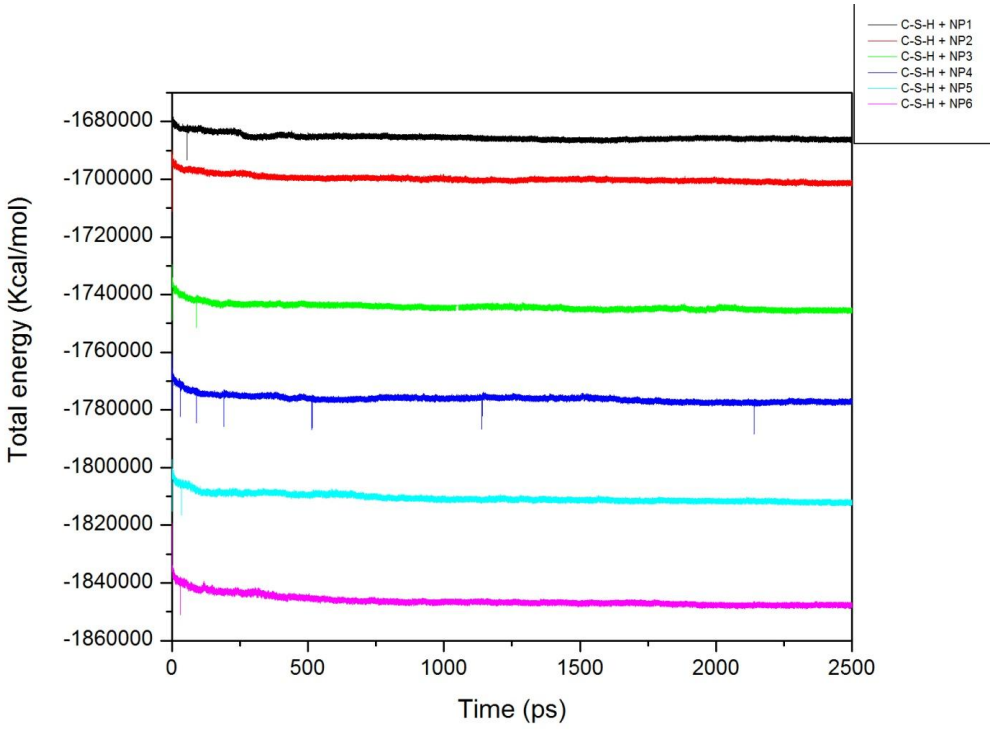

Fig.6. 6: Total energy of NP/C-S-H structures during relaxation as a function of the equilibration time

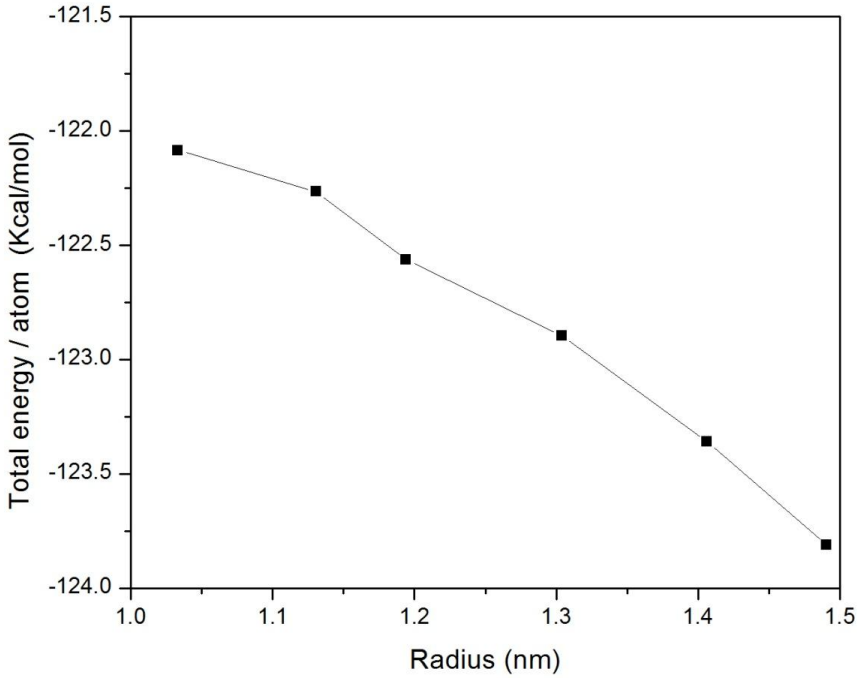

Fig.6. 7: Total energy of Fe_2O_3/C-S-H as a function of the inserted nanoparticle radius

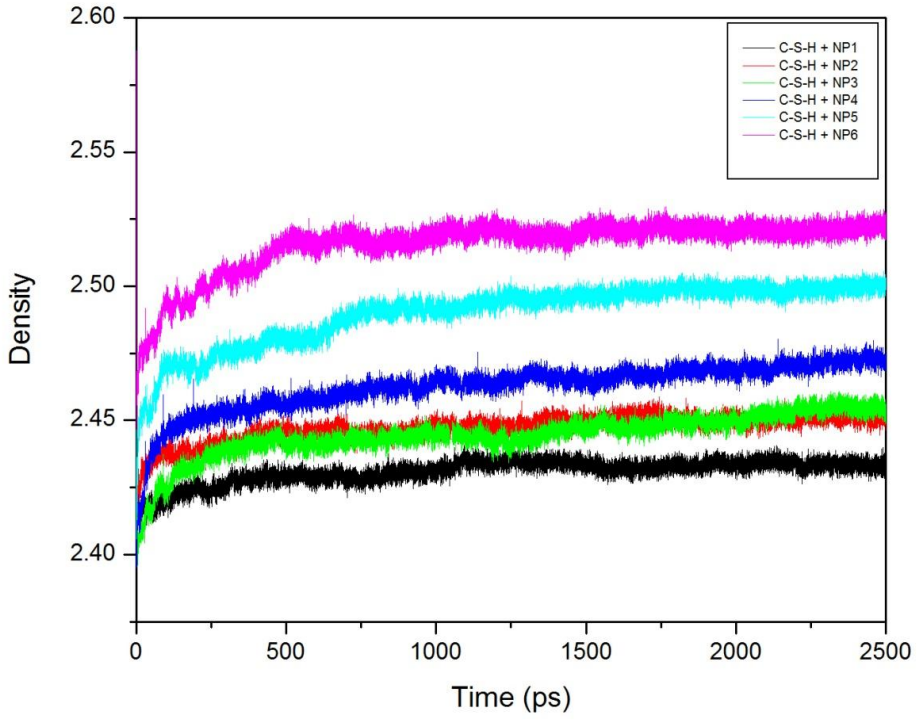

Fig.6. 8: Density evolution of the NP/C-S-H structures during equilibration.

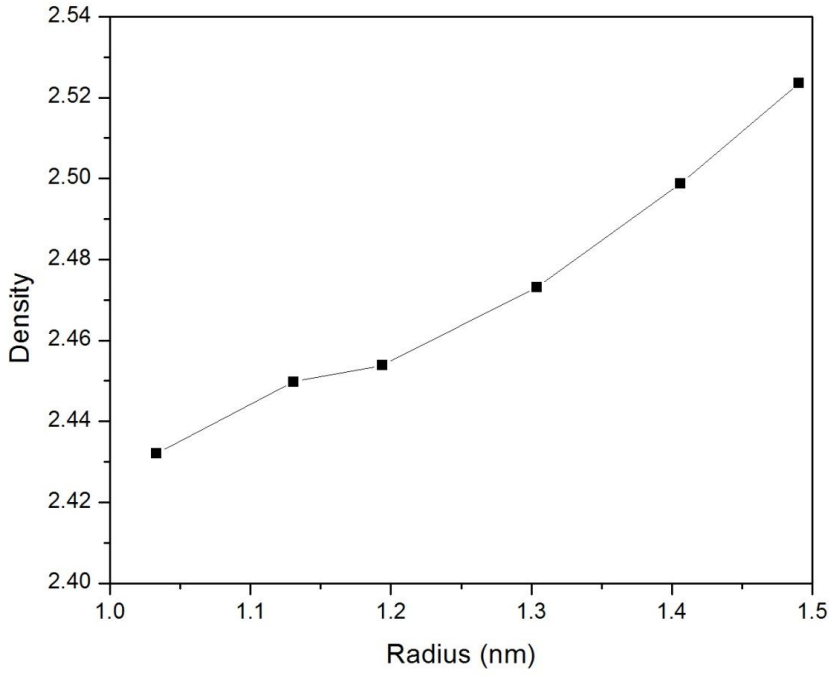

.

Fig.6. 9: Density of Fe_2O_3/C-S-H composites as a function of the inserted nanoparticle radius.

6.3.2. Interaction energy:

The nonbonding interaction energy between the nanoparticle and C-S-H matrix at the end on the simulations was calculated according to the formula:

$$U_{inter} = U_{\mathrm{C-S-H/Fe2O3}} - U_{C-S-H} - U_{\mathrm{Fe2O3}} \quad (6.2)$$

Where $U_{\mathrm{C-S-H/Fe2O3}}$, U_{CSH} and U_{NP} are the nonbonding energies of the Fe_2O_3/C-S-H composite, C-S-H matrix and Fe_2O_3 nanoparticle respectively. In Fig.6.10, the negative non-bonding interaction energy denotes an adhesive nature of interactions between C-S-H and the Fe_2O_3 nanoparticle that increases with the nanoparticle size. Indeed, as the inserted nanoparticle size increases, more atoms of the nanoparticle are located at the surface that connect with C-S-H atoms, which increases the number of non-bonding pairs between the nanoparticle and the C-S-H matrix.

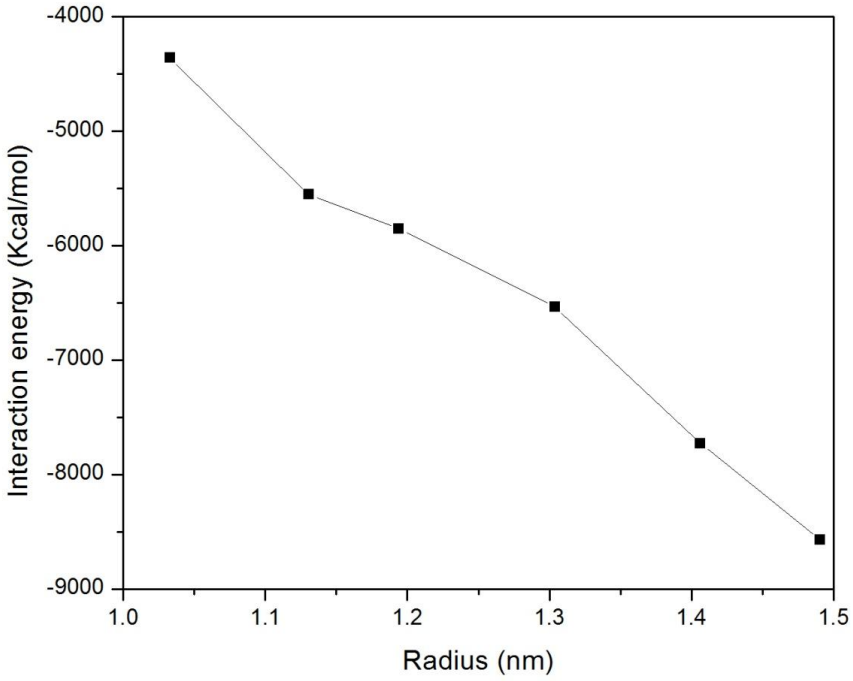

Fig.6. 10: Non-bonding interaction energy between Fe_2O_3 nanoparticle and C-S-H matrix as a function of the inserted nanoparticle radius.

Splitting up the non-bonging energy into short range Van der Waals (vdW) and long range electrostatic energy parts, we see from Fig.6.11 that the total interaction energy is mainly due to the vdW energy contribution. The small positive electrostatic energy contribution indicates repulsive long range forces between C-S-H and Fe_2O_3 nanoparticle that are largely offset by the attractive vdW short-range forces. The variation of interaction energy according to the nanoparticle size is mainly governed by that of vdW energy contribution while the electrostatic energy component is almost the same for all sizes of the inserted nanoparticles.

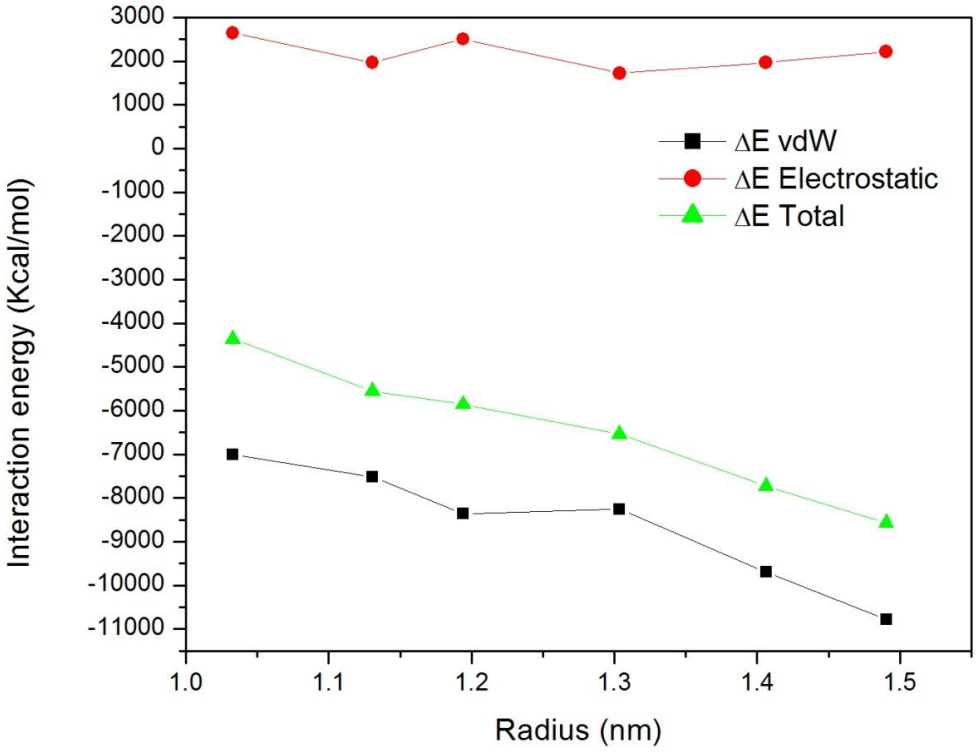

Fig.6. 11: Van-der-Waals interaction energy, Electrostatic interaction energy and total interaction energy of C-S-H/Fe_2O_3 as functions of the inserted Fe_2O_3 nanoparticle radius.

In order to compare the number of non-bonding pairs between the two structures as an intensive property, the interaction energy was normalized by the volume of the inserted nanoparticle. We can see from Fig.6.12 that the number of nonbonding pairs per unit volume decreases as the nanoparticle size increases. The best normalized interaction energy is found for the smallest inserted nanoparticle of 1.03nm radius.

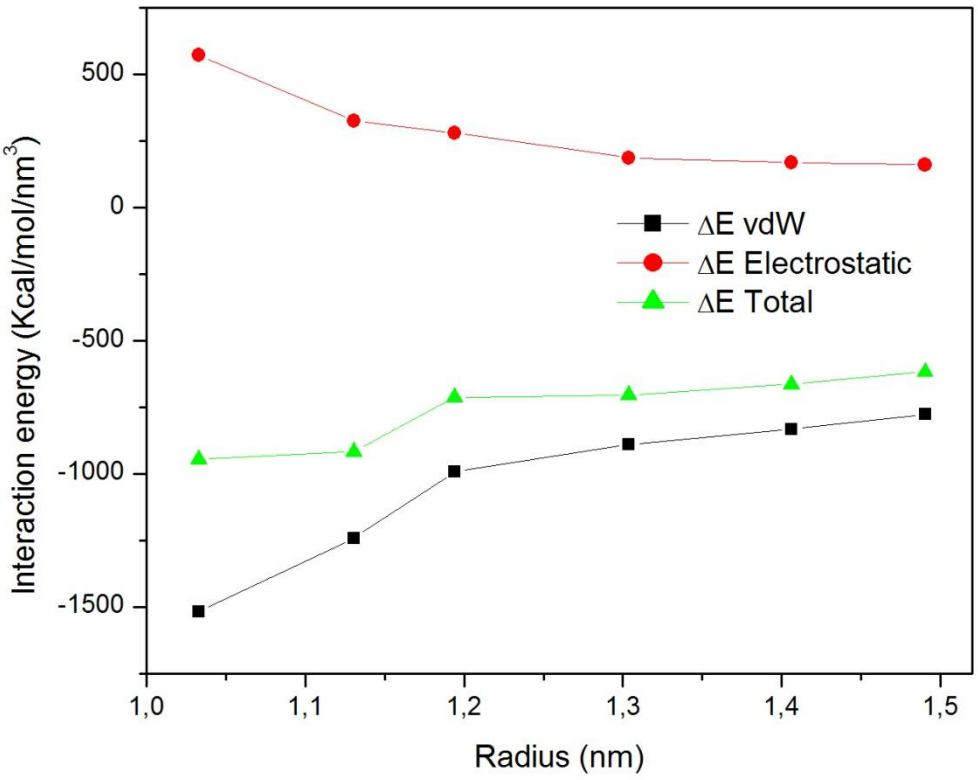

Fig.6. 12: Normalized Van-der-Waals interaction energy, Electrostatic interaction energy and total interaction energy of C-S-H/Fe_2O_3 as functions of the inserted Fe_2O_3 nanoparticle radius.

6.3.3. Radial distribution function:

In order to investigate the coordination correlations between atoms of the Fe_2O_3/C-S-H composite, we analyzed the radial distribution function (RDF). The radial distribution functions of C-S-H and Fe_2O_3/C-S-H modified structures were displayed in Fig.6.13.

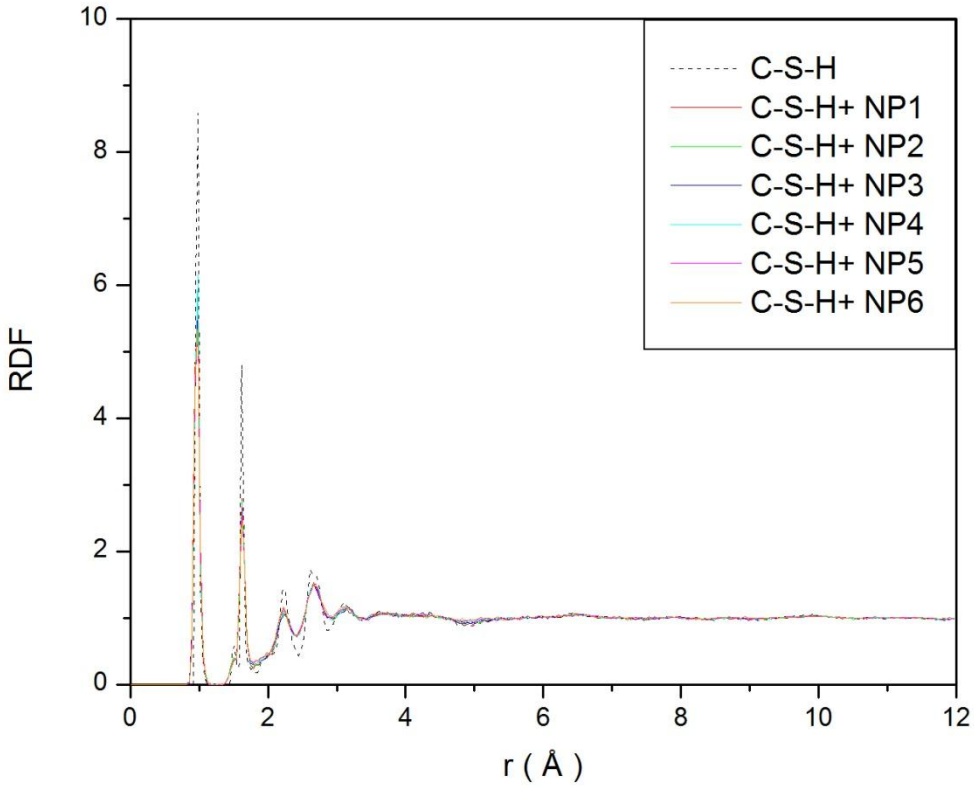

Fig.6. 13: Radial distribution function of C-S-H and Fe_2O_3 modified C-S-H structures

We can see that there is no major change in the RDF shape. However, one can notice that the peaks are sharper and more pronounced for the pure-CSH structure. In order to understand the origin of each peak, the atomic contribution to RDF were plot in Fig.6.14 where we compare the partial RDF pair contributions $g_{AB}(r)$ of pure C-S-H and modified Fe_2O_3/C-S-H structure with NP1 insertion type. Fig.6.15 shows a zoom of the main peaks of RDF contributions. We can see a small peak situated at 1.0 Å that appears in the NP1/C-S-H that originates from the contribution of Oxygen atoms from the Fe_2O_3 nanoparticle (Of) that bond with the Hydrogen atoms from the C-S-H surrounding matrix. A short and large peak appears at 2.1 Å that comes from the Fe-Of bonding in the Fe_2O_3 nanoparticle. We can see also another large peak at 2.58 Å that originates from Fe atoms that associate with Oxygen atoms of the C-S-H matrix.

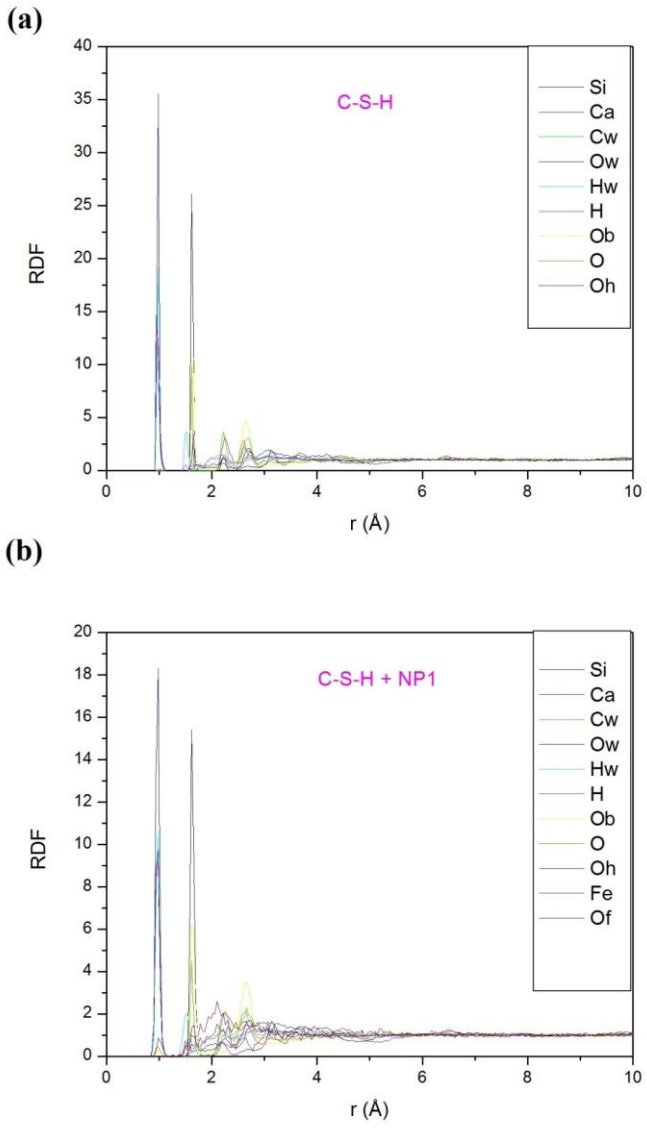

Fig.6. 14: RDF atomic contributions of: (a) Pure C-S-H. (b) Fe_2O_3/C-S-H structure modified by the NP1-type Fe_2O_3 nanoparticle

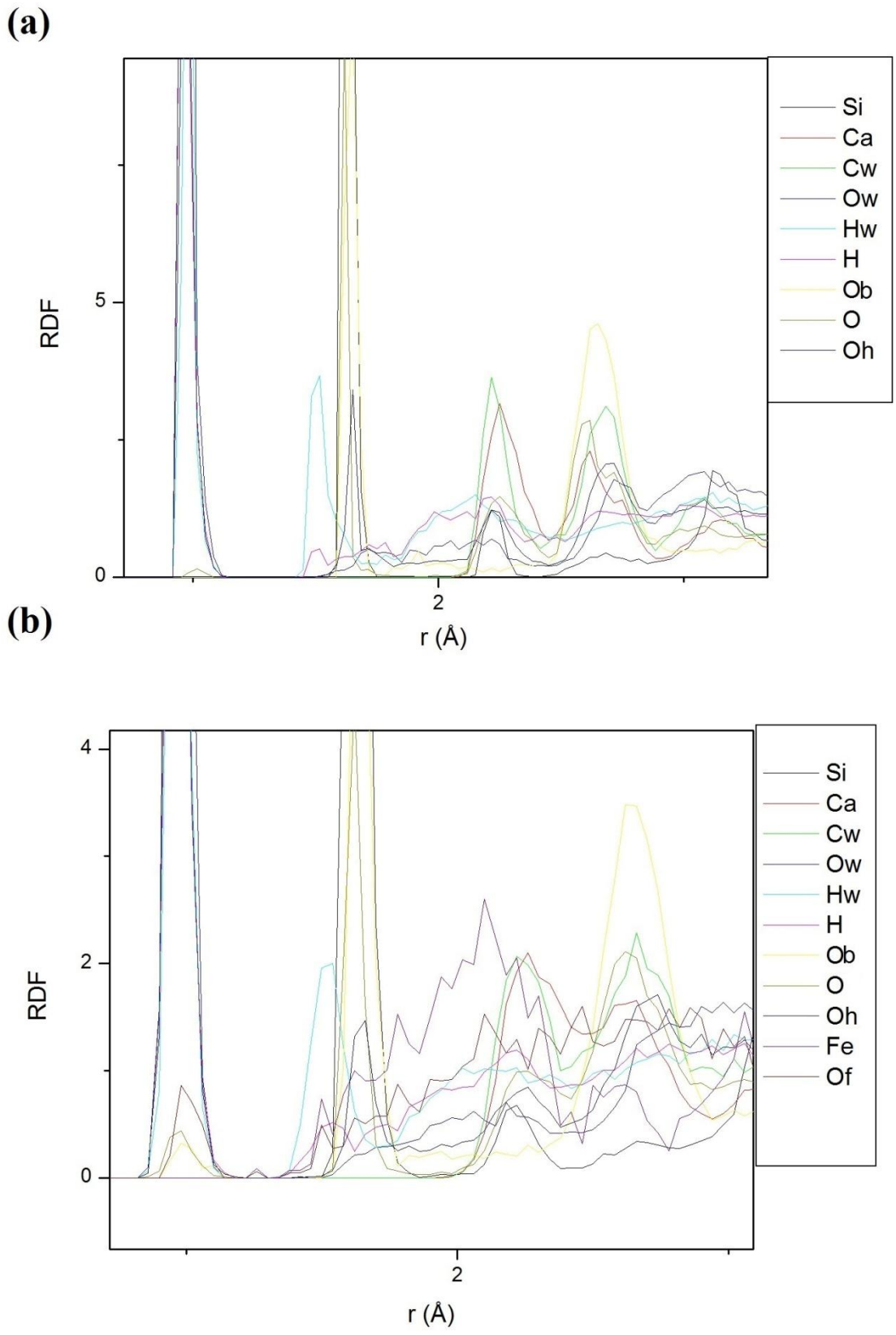

Fig.6. 15: Major peaks of: (a) C-S-H pure structure. (b) NP1/C-S-H structures.

6.3.4. Bonding mechanism:

To get more insights of the interfacial bonding between Fe_2O_3 nanoparticles and C-S-H matrix, the coordination number between Fe and oxygen atoms from the C-S-H matrix and between oxygen atoms of Fe_2O_3 nanoparticles Of and hydrogen atoms from the C-S-H surrounding matrix were calculated. Variations of the Si—O and O—H coordination numbers in C-S-H matrix induced by adding Fe_2O_3 nanoparticles were also evaluated. We see from Table 6.2 that Fe atoms coordinate with oxygen atoms of C-S-H near the surface of the nanoparticle while Table 6.3 shows that Of atoms of the nanoparticle coordinate with Hydrogen atoms from the C-S-H matrix. The iron atoms Fe located at the surface of the nanoparticle coordinate with hydroxyls (OH-) from the C-S-H matrix. As the nanoparticle increases, more Fe atoms from the nanoparticle form bonds with the Oh and Ow atoms with an average bond length of 1.97 Å and 1.83 Å respectively. However, the number of Fe---O pairs per unit volume decreases as the nanoparticle size increases which explains the decreasing tendency of Fe---O coordination number in Table.6.2. This is consistent with the normalized interaction energy variation with respect to nanoparticle size. In addition, Fe atoms coordinate with oxygen atoms of the silica sheet (O and Ob types) while the Si—O total coordination number of 4 in pure C-S-H decreases as the nanoparticle size increases (Table 6.4). The Fe atoms act on the silica chain by attracting the outer oxygen of the chain. Thus, the Silica chain geometry is modified by the vicinity of the nanoparticle. The tetrahedral geometry of Si—O coordination is altered nearby the nanoparticle and an amount of oxygen atoms of the silica chains are trapped near the nanoparticle surface as we can see from Fig.6.16.

Table 6.2 : The coordination number of Fe atoms and oxygen atoms of the C-S-H matrix

	C-S-H+NP1	C-S-H+NP2	C-S-H+NP3	C-S-H+NP4	C-S-H+NP5	C-S-H+NP6
Fe-Ow	0.25	0.15	0.17	0.13	0.15	0.13
Fe-Ob	0.11	0.06	0.05	0.07	0.04	0.06
Fe-O	0.41	0.31	0.31	0.26	0.24	0.26
Fe-Oh	0.50	0.41	0.40	0.35	0.30	0.31
Total	1.27	0.92	0.93	0.81	0.74	0.76

Table 6.3 : The coordination number of Of atoms and Hydrogen atoms of the C-S-H matrix

	C-S-H+NP1	C-S-H+NP2	C-S-H+NP3	C-S-H+NP4	C-S-H+NP5	C-S-H+NP6
Of-Hw	0.06	0.03	0.03	0.05	0.03	0.02
Of-H	0.05	0.05	0.04	0.04	0.02	0.03
Total	0.11	0.08	0.07	0.09	0.05	0.05

Table 6.4: The coordination number of Si atoms and oxygen atoms of the C-S-H matrix

	C-S-H	C-S-H+NP1	C-S-H+NP2	C-S-H+NP3	C-S-H+NP4	C-S-H+NP5	C-S-H+NP6
Si-Ow	0.00	0.03	0.04	0.04	0.03	0.04	0.06
Si-Ob	1.09	1.04	1.03	1.04	1.01	1.02	1.00
Si-O	2.20	2.15	2.15	2.14	2.15	2.14	2.11
Si-Oh	0.70	0.73	0.72	0.72	0.74	0.73	0.75
Total	4.00	3.96	3.94	3.94	3.93	3.92	3.92

Table 6.5: Coordination numbers of hydrogen atoms around oxygen atoms from water molecules and from hydroxyl groups of the C-S-H matrix.

	C-S-H	C-S-H+NP1	C-S-H+NP2	C-S-H+NP3	C-S-H+NP4	C-S-H+NP5	C-S-H+NP6
Ow-Hw	1.81	1.61	1.60	1.56	1.58	1.57	1.55
Ow-H	0.03	0.09	0.10	0.1	0.11	0.10	0.11
Total	1.84	1.70	1.70	1.66	1.69	1.67	1.66
Oh-Hw	0.08	0.13	0.12	0.14	0.13	0.13	0.13
Oh-H	0.97	0.91	0.91	0.89	0.88	0.89	0.86
Total	1.05	1.04	1.03	1.03	1.01	1.01	0.99

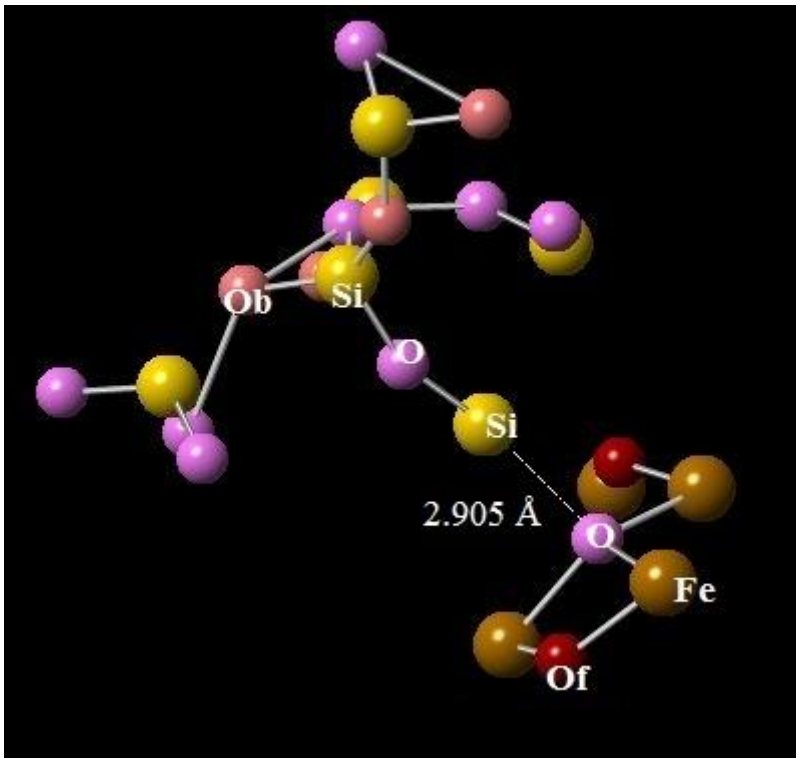

Fig.6. 16: Snapshot of Oxygen atom trapped at the interface of Fe_2O_3 nanoparticle.

In the other hand, Hydrogen atoms are attracted by outsider oxygen atoms of the nanoparticle (Of) (Table 6.3). As we can see from Table 6.5, H—O total coordination number in the C-S-H matrix decreases as the nanoparticle size increases. The Ow-Hw coordination number decreases the most compared to the other O-H coordination types. This indicates that water molecules H_2O of the C-S-H interlayer dissociate to OH- hydroxyl ions and H+ protons in vicinity of the inserted nanoparticle. The hydroxyl ions (OH-) coordinate with Fe atoms on the surface while the protons H+ bind with nearby surface oxygen of the nanoparticle O_f according to the following mechanism:

$$H_2Ow + O_f \rightarrow O_wH + O_fH$$

This bonding mechanism is also accompanied by the formation of hydrogen bonds between O_fH and O_wH as illustrated in Fig.6.17.a where the O_wH is acceptor of the hydrogen bond. The water molecules also interact with the nanoparticle via hydrogen bond, donating the hydrogen bond to surface oxygen O_f of the nanoparticle as shown in Fig.6.17.b.

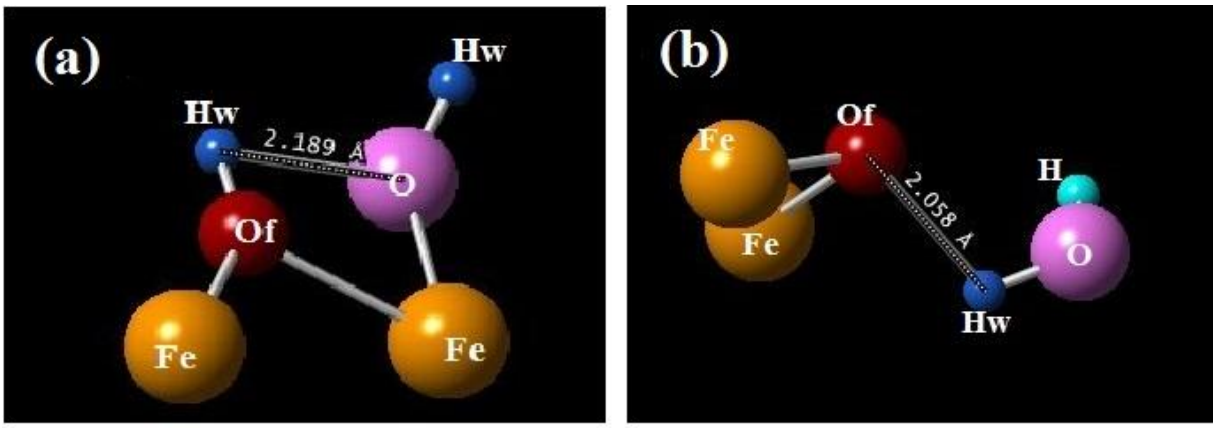

Fig.6. 17: (a) Hydrogen bond between OH_w and O_fH_w where OH_w acts as an acceptor. (b) Hydrogen bond between water molecule and surface Oxygen O_f where water acts as a donator.

6.4. Dynamic properties:

In order to study the effect of the Fe_2O_3 nanoparticle insertion on the molecular mobility of atoms of the C-S-H matrix, the mean squared displacement (MSD) of hydrogen and oxygen atoms of water molecules and hydroxyls was calculated using the following expression:

$$\mathrm{MSD} = \left\langle \frac{1}{N} \sum_{i=1}^{N} (r_i(t) - r_i(0))^2 \right\rangle \quad (6.3)$$

Where N is the total number of atoms, r_i is position vector of particle i and $r_i(t)$ - $r_i(0)$ indicates the (vector) distance traveled by particle i. Then, self-diffusion coefficients of H, Hw, Oh and Ow atoms were deduced using Einstein equation:

$$D = \frac{1}{6} \lim_{t \to \infty} \left\langle \frac{1}{N} \sum_{i=1}^{N} \left(r_i(t) - r_i(0)\right)^2 \right\rangle \quad (6.4)$$

MSD of the considered atoms is depicted in Fig.6.18 We can clearly see that hydrogen and oxygen atoms of water and hydroxyl groups have greater mobility in the Fe_2O_3/C-S-H composites compared to immobile atoms in pure C-S-H with a higher mobility as the particle size increases. This trend is consistent with previous observations related to interfacial interaction energy and interfacial bonding mechanism. The higher mobility of interfacial water molecules for larger nanoparticles results in weaker interfacial adhesion energy.

However, MSD increases slowly with time as MSD values do not exceed 8 $Å^2$ and 3.5 $Å^2$ for water atoms and hydroxyl atoms respectively in 200ps time interval.

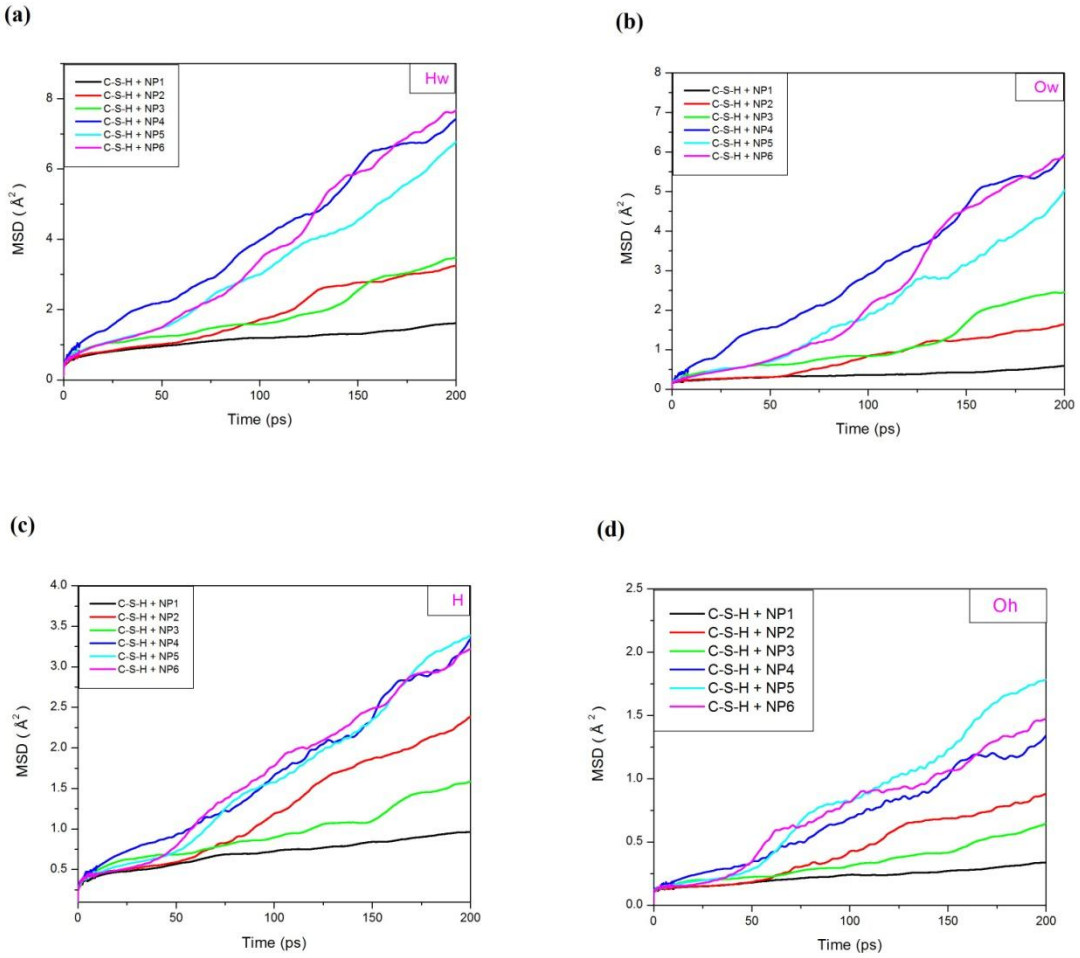

Fig.6. 18: Mean square displacement (MSD) of : (a) Hydrogen atoms of water molecules (Hw), (b) Oxygen atoms of water molecules (Ow), (c) Hydrogen atoms of hydroxyl groups (H) and (d) Oxygen atoms of hydrogen groups (Oh).

Water atoms of C-S-H matrix in the Fe_2O_3/C-S-H composites have the highest average diffusion coefficient with an increase from 1.3 x 10^{-11} to 6.4 x 10^{-11} m²/s for hydrogen atoms (Hw) and from 0.5 x 10^{-11} to 4.9 x 10^{-11} m²/s for oxygen atoms (Ow) as shown in Fig.6.19. The diffusion coefficients of hydroxyl groups atoms (H and Oh) increase at a lower rate as the nanoparticle size increases with a range of 0.8 x 10^{-11} - 2.7 x 10^{-11} m²/s for hydrogen atoms (H) and 0.3 x 10^{-11} - 1.2 x 10^{-11} m²/s for oxygen atoms (Oh) depending on the nanoparticle size.

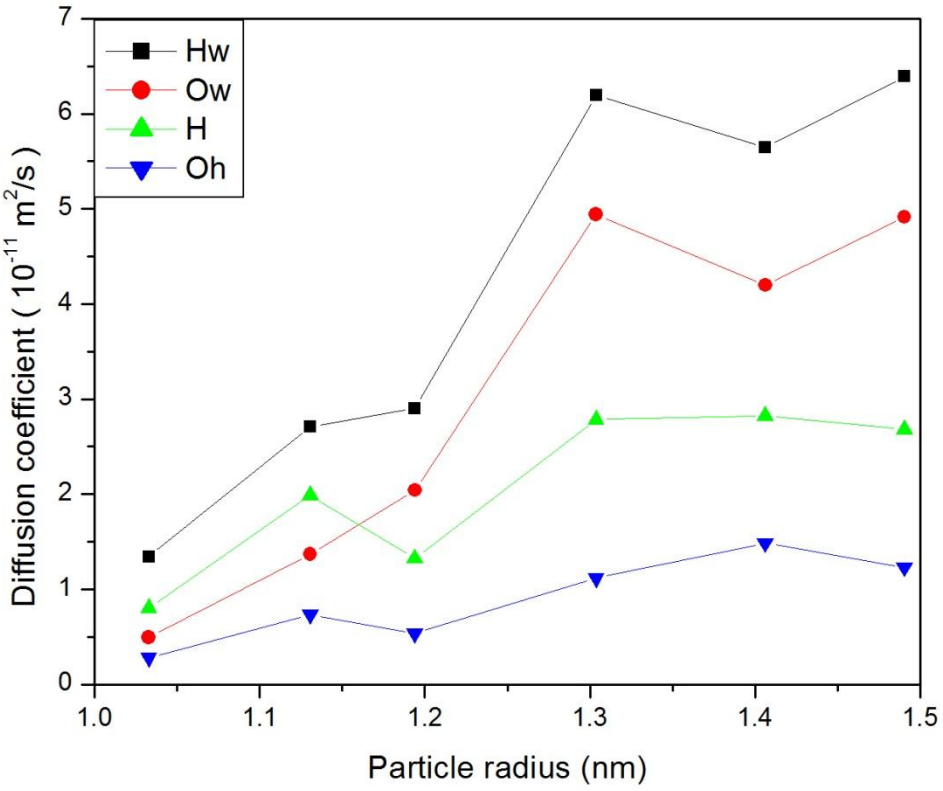

Fig.6. 19: Diffusion coefficients of water and hydroxyl atoms in C-S-H matrix.

6.5. Mechanical Properties

6.5.1. Elastic constants:

The stiffness tensor was calculated according to stress-strain relationship for the six nanomodified structures and compared with that of pure C-S-H in Table 6.6. An overall comparison of the different stiffness tensor components shows that the insertion of Fe_2O_3 nanoparticles visibly reduces the resistance of the C-S-H material to deformation in the elastic regime.

Table 6.6: The elastic constants of pure C-S-H and modified NP/C-S-H structures

	CSH	CSH+NP1	CSH+NP2	CSH+NP3	CSH+NP4	CSH+NP5	CSH+NP6
C_{11} (GPa)	85.74	77.66	77.52	76.41	73.93	72.81	72.37
C_{22} (GPa)	83.18	82.24	77.32	76.00	80.78	72.14	67.86
C_{33} (GPa)	67.80	60.66	59.93	60.02	54.91	51.84	49.53
C_{44} (GPa)	19.04	17.30	15.13	13.13	12.73	11.91	16.31

C_{55} (GPa)	18.72	14.96	13.45	16.71	13.28	14.30	14.59
C_{66} (GPa)	31.27	26.07	24.93	23.89	25.64	24.56	23.05
C_{12} (GPa)	45.31	44.53	41.23	41.53	40.11	36.37	34.99
C_{13} (GPa)	26.49	27.33	25.55	30.22	23.74	22.01	20.69
C_{23} (GPa)	27.01	28.68	26.38	30.23	27.07	25.38	24.44

The elastic tensor can be used to calculate equivalent averaged mechanical properties. The bulk modulus (K) and shear modulus (G) were calculated according to the Voigt-Reuss-Hill approximation [131]. Then, the equivalent isotropic Young's modulus (E) was approximated as follows:

$$E = \frac{1}{\frac{1}{3G}+\frac{1}{9K}} \quad (6.5)$$

Comparing with pure C-S-H, we can see from Fig.6.20 that the calculated elastic moduli (E, K and G) are negatively affected by Fe_2O_3 nanoparticles insertion. Both Young's and bulk moduli decrease as the nanoparticle size increases with a maximum reduction of 23% and 20% respectively obtained with NP5 and the NP6 insertion types. The shear modulus is also reduced, but keeps a constant value around 18GPa for all sizes of Fe_2O_3 nanoparticles. Among the NP/C-S-H structure, the NP1 is found to give the best mechanical properties with reductions of 13%, 3% and 14% reduction of the Young's, bulk and shear moduli respectively compared to pure C-S-H. This is consistent with the interfacial interaction energy variation with respect to nanoparticles size. The interfacial interaction energy and the number of non-bonding pairs between C-S-H and the Fe_2O_3 nanoparticle decrease by increasing the nanoparticle, resulting in a decrease of the mechanical properties with respect to the size of inserted nanoparticles.

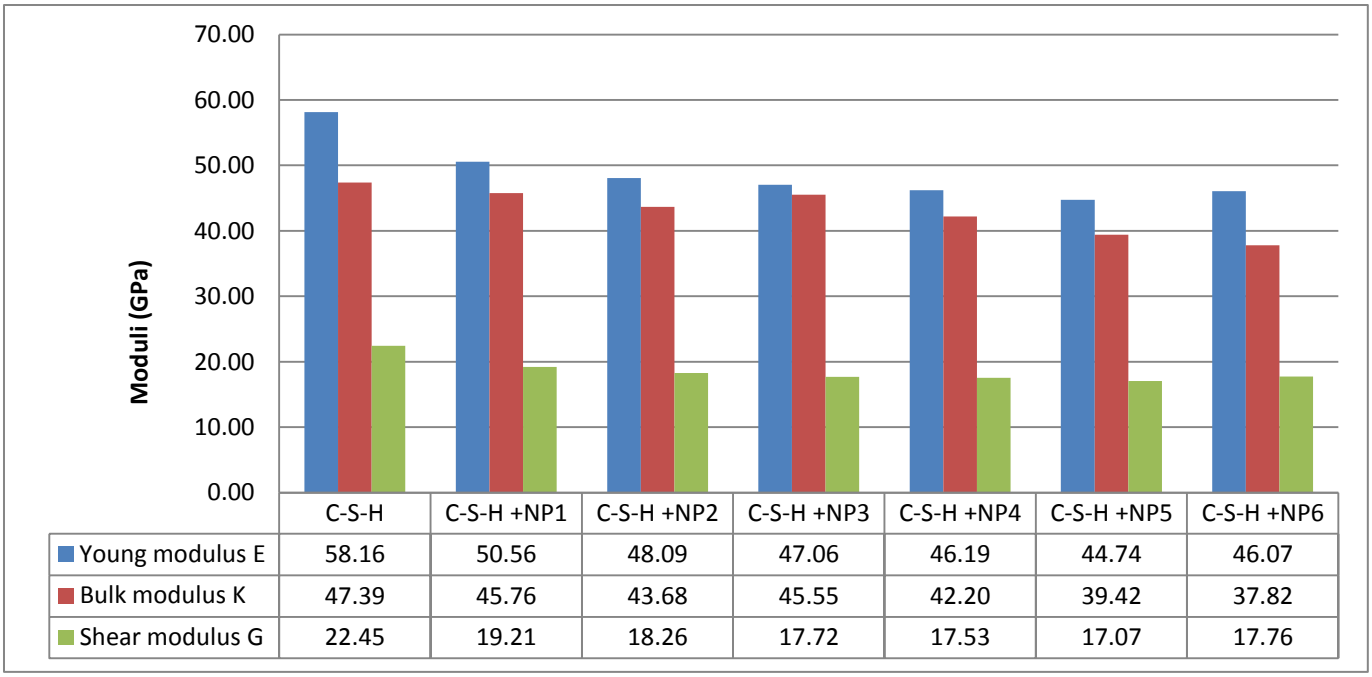

	C-S-H	C-S-H +NP1	C-S-H +NP2	C-S-H +NP3	C-S-H +NP4	C-S-H +NP5	C-S-H +NP6
Young modulus E	58.16	50.56	48.09	47.06	46.19	44.74	46.07
Bulk modulus K	47.39	45.76	43.68	45.55	42.20	39.42	37.82
Shear modulus G	22.45	19.21	18.26	17.72	17.53	17.07	17.76

Fig.6. 20 : The Young's modulus (E), Bulk modulus (K) and shear modulus (G) of pure C-S-H and NP/C-S-H structures.

6.5.2. Ultimate strength:

By tensioning the pure and modified C-S-H structures, the ultimate strength along x, y and z directions were determined and compared in Fig.6.21. We can see that the ultimate strength along the x-direction and y-direction decrease according to the inserted nanoparticle size up to 20% and 21% respectively. However, the ultimate strength along the z direction is clearly enhanced by inserting Fe_2O_3 nanoparticle with a maximum gain of 29% by the NP1 insertion type.

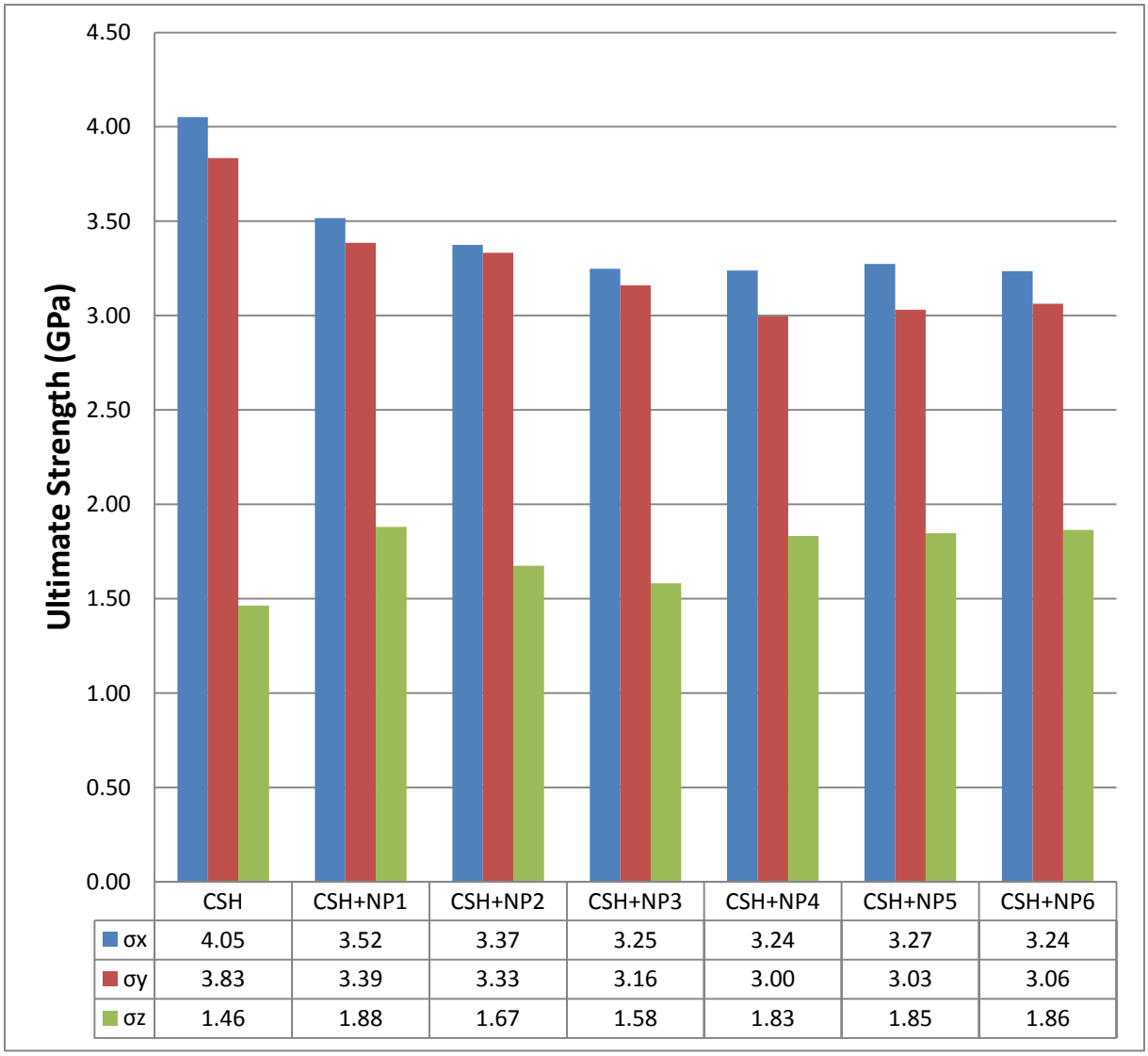

	CSH	CSH+NP1	CSH+NP2	CSH+NP3	CSH+NP4	CSH+NP5	CSH+NP6
σx	4.05	3.52	3.37	3.25	3.24	3.27	3.24
σy	3.83	3.39	3.33	3.16	3.00	3.03	3.06
σz	1.46	1.88	1.67	1.58	1.83	1.85	1.86

Fig.6. 21: The ultimate strengths along the x, y and z direction of pure C-S-H and NP/C-S-H structures

6.5.3. Failure mode:

The molecular structure of 1NP/C-S-H was observed at different stages of deformation in the plastic phase during the stretching process along x,y and z axes.

6.5.3.1. Tensile along x axis:

In the elastic phase, strain is taken up by the calcium and silicate chains that are lengthened along x-direction. After the yield point, defects appear in the interlayer region as we can see at 0.2 Å/Å strain in Fig.6.22.b. The small cracks rapidly propagate into neighboring calcium silicate sheets as it is illustrated at 0.4 Å/Å strain in Fig.6.22.c. Finally, cracks combine together to form the rupture surface that slips through the interface between the nanoparticle and C-S-H matrix as shown in Fig.6.22.d. Consequently, interactions between the Fe_2O_3

nanoparticle and C-S-H matrix are highly weakened, which leads to the separation of the composite into two parts soon after 0.5 Å/Å strain. It is important to see here that the Fe_2O_3 nanoparticle doesn't take up the deformations at the plastic stage as interactions are weakened at the interface zone between C-S-H matrix and the Fe_2O_3 nanoparticle.

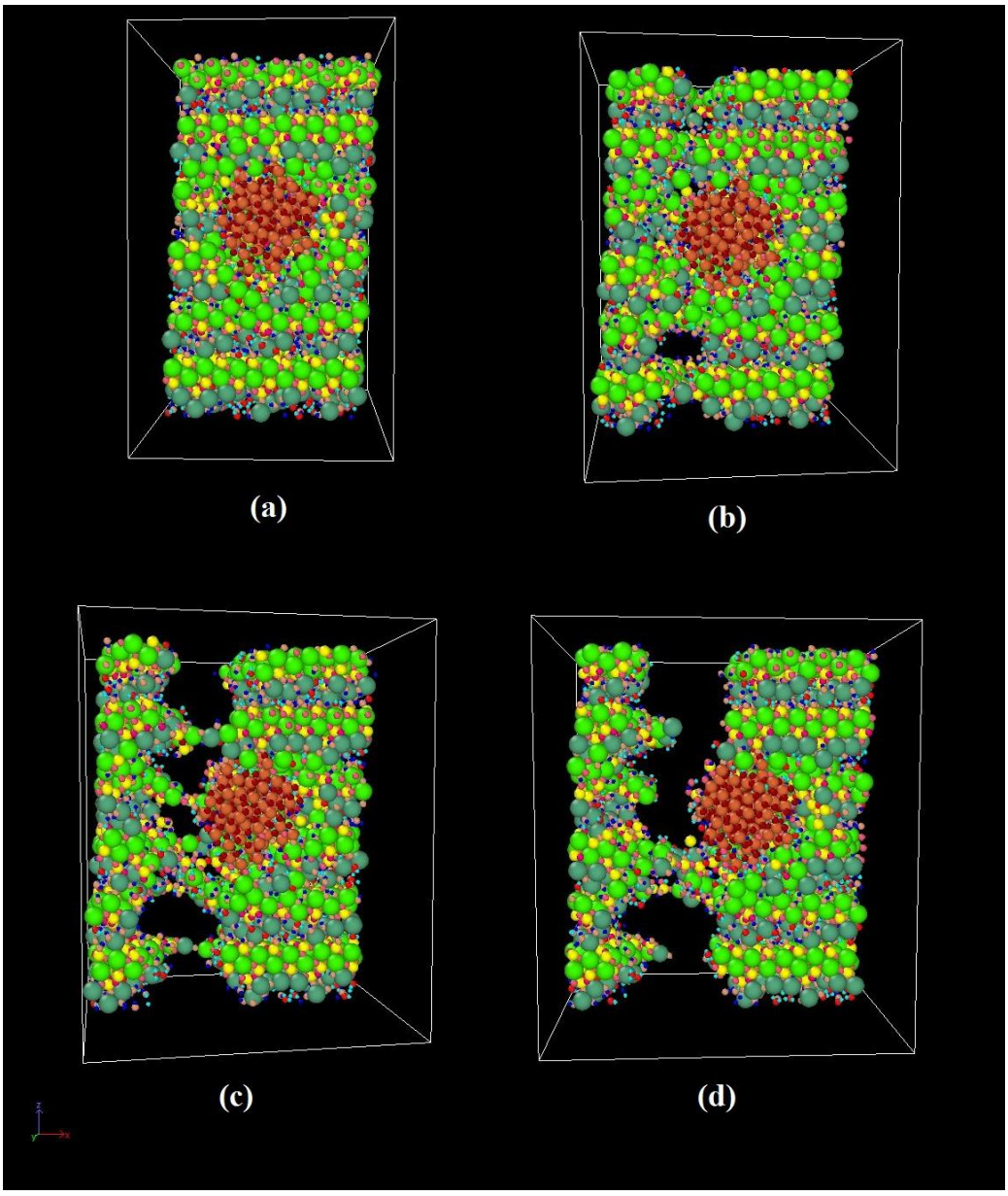

Fig.6. 22: (XZ) slice of 1NP/C-S-H structure tensioned along x direction at : (a) 0 strain, (b) 0.2 Å /Å strain, (c) 0.4 Å /Å strain and (d) 0.5 Å /Å.

6.5.3.2. Tensile along y axis:

The response of 1NP/C-S-H composite to tensile along y direction is similar to that along x direction. Right after the yield point, damage of the structure starts with small defects in the interlayer region, most are located in vicinity of the nanoparticle as we can see at 0.15 Å/Å in

Fig.6.23.b The interactions between Fe_2O_3 nanoparticle and C-S-H are thus weakened and cracks grow in the interface zone as it is illustrated at 0.2 Å/Å in Fig.6.23.c and propagate into neighboring calcium silicate sheets as the strain increases from 0.2 Å/Å to 0.4 Å/Å (Fig.6.23.d) where the total failure of the structure is almost reached. In contrast with tensile along x direction, cracks are mostly initiated in the interface between the nanoparticle and C-S-H matrix as soon as the yield point is reached, leading to a rapid crack propagation with a tangent rupture surface to the nanoparticle surface at the end of the tensile test.

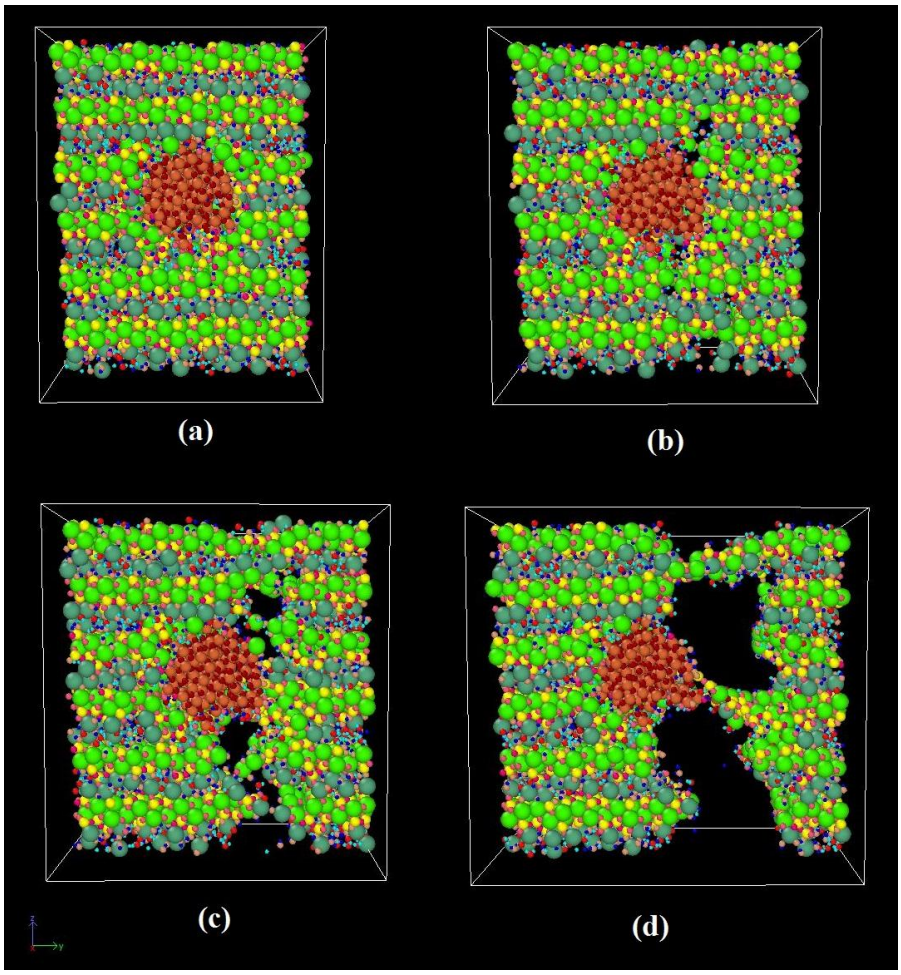

Fig.6. 23: (XZ) slice of 1NP/C-S-H structure tensioned along y direction at: (a) 0 strain, (b) 0.15 Å /Å strain, (c) 0.2 Å /Å strain and (d) 0.4 Å /Å.

6.5.3.3. Tensile along z direction:

For tensile along z-direction, the 1NP/C-S-H exhibits a different failure mode. The defects appear at an early stage of deformation as the yield point corresponds to 0.07 Å/Å strain approximately. Fig.6.24.b shows the small cracks at 0.08 Å/Å strain, initiated in the first interlayer above the nanoparticle position, that immediately propagate in the same interlayer zone as shown in Fig.6.24.c The interaction of the nanoparticle with upper atoms of C-S-H

matrix in vicinity of the crack surface resists to crack propagation which slightly puts off the ultimate failure of the structure as illustrated in Fig.6.24.d. Ultimately, the composite is split into two parts right after 0.17 Å/Å strain.

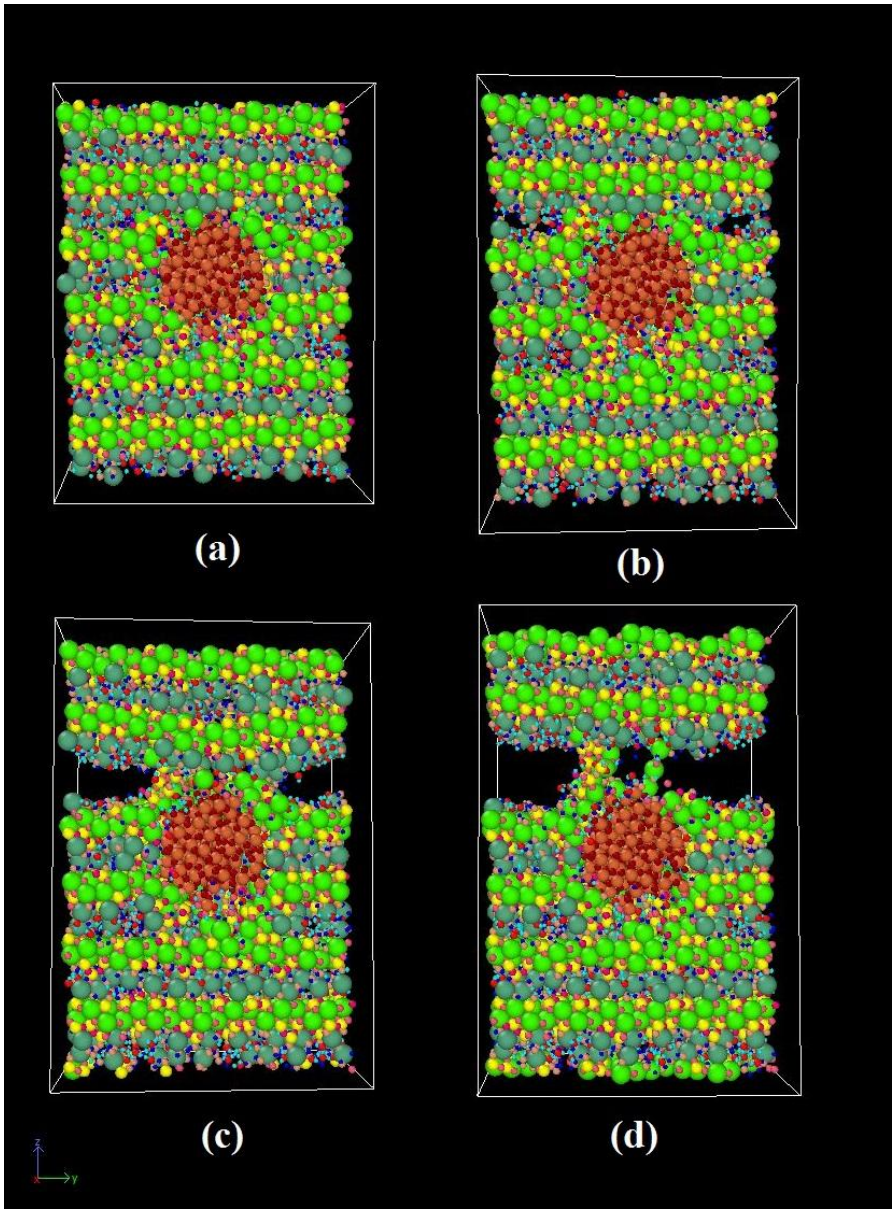

Fig.6. 24: (YZ) slice of 1NP/C-S-H structure tensioned along z direction at: (a) 0 strain, (b) 0.08 Å /Å strain, (c) 0.12 Å /Å and (d) 0.17 Å /Å strain.

It is worth mentioning that in the case of tensile along x and y directions, the interlayer calcium atoms attempt to reconstruct the fractured calcium silicate chains, which slows down the crack propagation and sustains the plastic phase. The crack propagation in response to tensile along z direction, at variance with that along x and y directions, occurs in one interlayer and do not include the calcium silicate sheets region. Thus, the reconstruction mechanism is not observed, which explains the brittle failure mode of the composite along z

direction. However, the interaction of the nanoparticle with surrounding C-S-H atoms slightly holds the structure from attaining the ultimate failure that occurs at about 0.17 Å/Å for 1NP/C-S-H composite against only 0.1 Å /Å for pure C-S-H.

6.6. Conclusion:

The mechanical response of Fe_2O_3/ C-S-H composites is clearly influenced by the Fe_2O_3 nanoparticle size. The best mechanical properties are obtained for the smallest nanoparticle (2.1nm). As the NP1 type insertion gives the best surface interaction energy, the structure is more resistant to tensile along the three directions. The decrease of the effectiveness of Fe_2O_3 nanoparticles in enhancing the mechanical strength of cement by increasing the Fe_2O_3 volume fraction was also reported in the literature [182]. Our results show noticeable enhancement (of 33%) of the ultimate strength along z axis. However, the ultimate strengths along x and y directions are reduced by 13% and 11% respectively and the calculated mechanical properties (Bulk, Young's and shear moduli) of the composites with the NP1 insertion still lower than pure C-S-H. The previous section only considers the size dependency of the mechanical performance of nano-modified C-S-H. The reported reduction of the mechanical properties may be attributed to the "non-uniform distribution" of nanoparticles inside the C-S-H matrix. The nanoparticle is inserted inside only one interlayer while the other interlayers are left non-modified. This creates a local concentration of the Fe_2O_3 nanoparticles and thus an inharmonious distribution which weakens the whole composite structure. The density and the way nanoparticles are dispersed in the C-S-H matrix strongly affect the behavior of the composite. Experimental studies have shown that unsuitable dispersion of nanoparticles causes the reduction of the mechanical strength of cement and mortar [102,103].

Chapter 7: Density effect of Fe_2O_3 nanoparticles inside the C-S-H Matrix

7.1. Introduction:

In the previous chapter, we have only considered the size dependency of the mechanical performance of nano-modified C-S-H. The reported reduction of the mechanical properties may be attributed to the "non-uniform distribution" of nanoparticles inside the C-S-H matrix. The nanoparticle is inserted inside only one interlayer while the other interlayers are left non-modified. This creates a local concentration of the Fe_2O_3 nanoparticles and thus an inharmonious distribution which weakens the whole composite structure. The density and the way nanoparticles are dispersed in the C-S-H matrix strongly affect the behavior of the composite. Experimental studies have shown that unsuitable dispersion of nanoparticles causes the reduction of the mechanical strength of cement and mortar [102,103]. In this chapter, a major emphasis is placed on the effect of the distribution uniformity of the Fe_2O_3 nanoparticles inside the C-S-H matrix on the mechanical response of nano-Fe_2O_3/C-S-H composite

7.2. Model construction:

To study the effect of "well-dispersed" Fe_2O_3 nanoparticles on the mechanical response of the Fe_2O_3/C-S-H composite, we uniformly inserted four nanoparticles in the C-S-H matrix. In this study, we selected the NP1 nanoparticle type as it gives the best adhesion and mechanical properties as we have shown in the previous chapter (Chapter 6). According to experimental studies, excessive nanoparticles content can negatively affect the overall mechanical response of the composite [182]. In order to keep the content of the Fe_2O_3 nanoparticles lower than 5% volume fraction, a larger 5x5x3 C-S-H supercell (65.4 Å x 90.4 Å x 71.1 Å) of 37575 atoms was considered for this type of insertion. Then, we have adopted the same indention method as before to create space for the inserted nanoparticles. To avoid the nanoparticles overlapping and to maximize the distance between the nanoparticles, the four inserted nanoparticles were distributed as follows:

- Two voids were indented in both the 2rd and 4th interlayers of the C-S-H matrix with positions z_2= 19.2 Å and z_4= 43.7 Å.
- In each interlayer, the two nanoparticles are separated by a center-to-center distance of 45 Å along y direction with positions of y_1=22.5 Å and y_2=67.5 Å respectively.
- The nanoparticles occupy the center of the interlayer in x direction with a position x_0=32.7 Å.

Finally, the relaxed structure at room temperature is presented in Fig.7.1

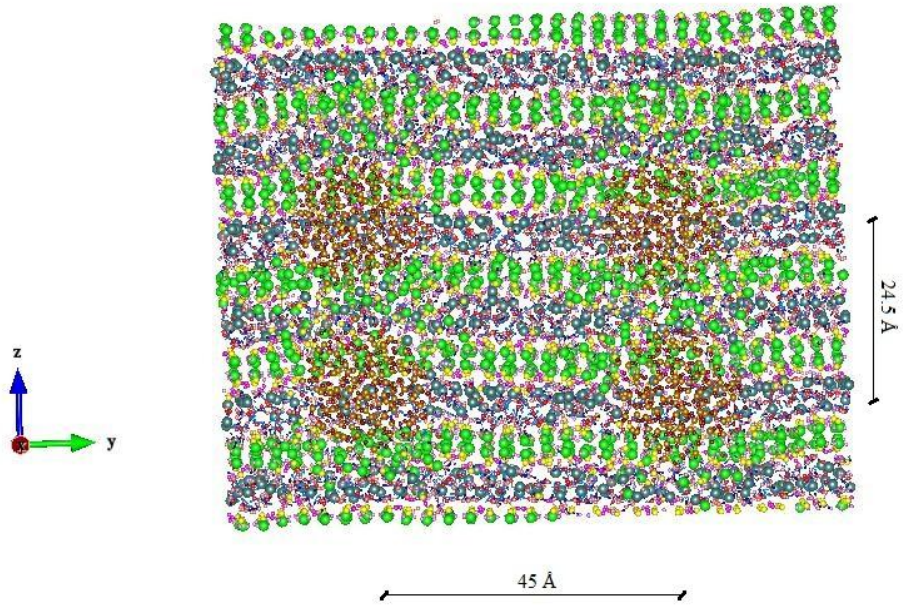

Fig.7. 1: The structure of the C-S-H matrix containing four Fe_2O_3 nanoparticles of type NP1.

7.3. Mechanical properties:

Tensile tests were performed along the three axes (x,y and z) and stress-strain curves were obtained for pure C-S-H, 1NP/C-S-H and 4NP/C-S-H composites that refer for C-S-H modified by one inserted Fe_2O_3 nanoparticle and four inserted Fe_2O_3 nanoparticles respectively. All tensile tests were carried out through gradual elongation at a strain rate of 0.007/ps

7.3.1. Tensile loading:

Fig.7.2 represents the stress-strain evolution in response to uniaxial tensile along x axis. Observing the curves slopes in the elastic phase, we can see that the 4NP1 insertion type clearly enhances the Young's modulus along x axis of the C-S-H matrix, contrary to 1NP1 insertion type that results in a slight reduction of the Young's modulus along x axis. However, the ultimate strength of both 1NP/C-S-H and 4NP/C-S-H composites still lower than that of pure C-S-H with a 13% and 9% reduction respectively. The behavior of the three structures is

quite different in the plastic regime. Compared to pure C-S-H, stress decreases rapidly after the yield point (at about 0.11 Å / Å strain) for 1NP/structure indicating a reduction of the material ductility along x direction. On the other hand, a small reduction of stress is observed after the yield point for 4NP/C-S-H followed by stress landing, which is a clear indication of enhanced ductility of the composite.

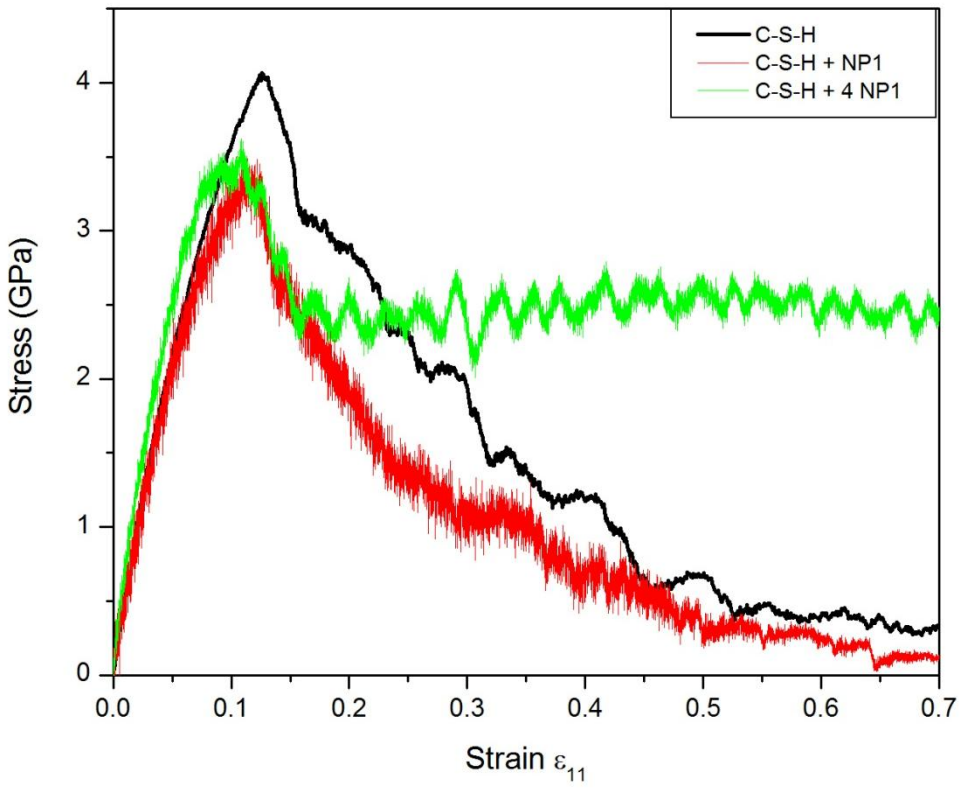

Fig.7. 2: The stress-strain curves of C-S-H, 1NP/C-S-H and 4NP/C-S-H tensioned along x axis.

The stress-strain curves corresponding to tension along y axis are shown in Fig.7.3. By observing the elastic phase, Young's modulus in y direction is the highest for 4NP/C-S-H structure whereas it is slightly reduced by 1NP1 insertion type. However, unlike tension along x axis, 4NP1 gives rise to higher yield point compared to 1NP1 insertion type with almost the same ultimate strength magnitude of pure C-S-H (about 3.85 GPa). After the yield point at 0.11 Å/Å, stress starts to slowly decrease and a large plastic phase is observed, suggesting great ductility of 4NP1/C-S-H in y direction.

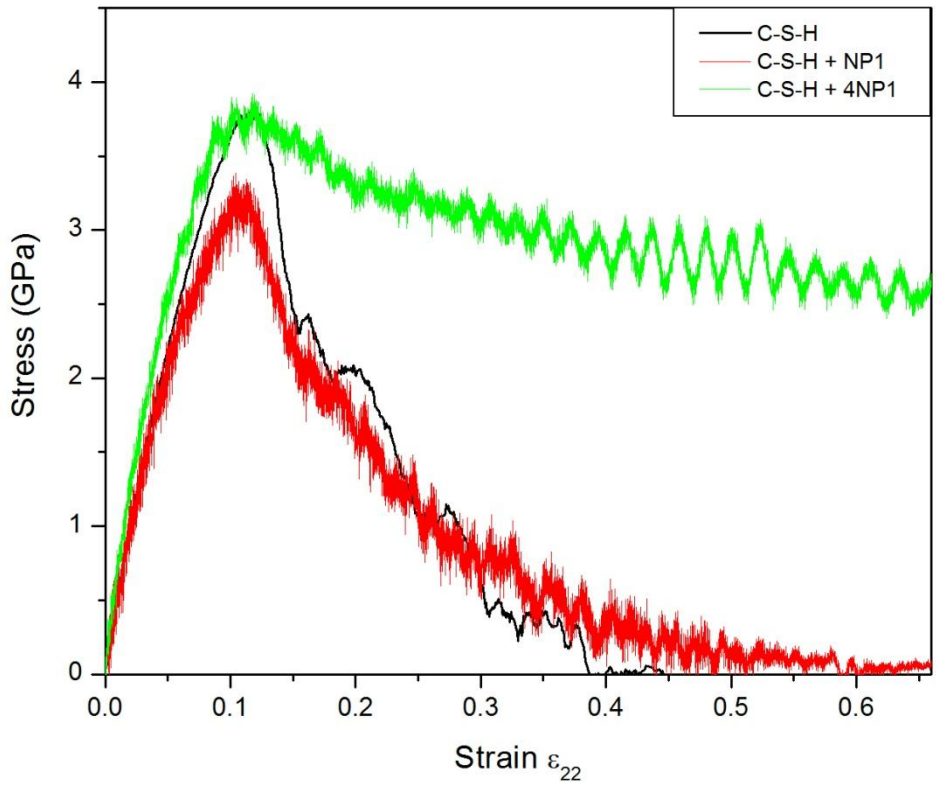

Fig.7. 3: The stress-strain curves of C-S-H, 1NP/C-S-H and 4NP/C-S-H tensioned along y axis.

In z direction, the stress-strain curves corresponding to tensile loading of the three structures are shown in Fig.7.4. Here, we see that both nanoparticle insertion modes enhance the stress strength along z axis by 34% and 110% for 1NP/C-S-H and 4NP/C-S-H respectively compared to pure C-S-H. Nevertheless, the response to tension is quite different comparing 1NP/C-S-H and 4NP/C-S-H composites. Even if stress drops more slowly to zero after reaching the yield point for 1NP/C-S-H compared to pure C-S-H, the structure ductility along z axis remains relatively poor. The 4NP/C-S-H exhibits higher resistance in the elastic phase and remarkable ductility in the plastic phase along z axis. The stress continues to increase after the yield point from 2.38 GPa at 0.09 Å/Å strain to 3.05 GPa at 0.4 Å/Å strain suggesting a structural hardening of the composite. Finally, stress starts to decrease slowly indicating the starting point of the material damage.

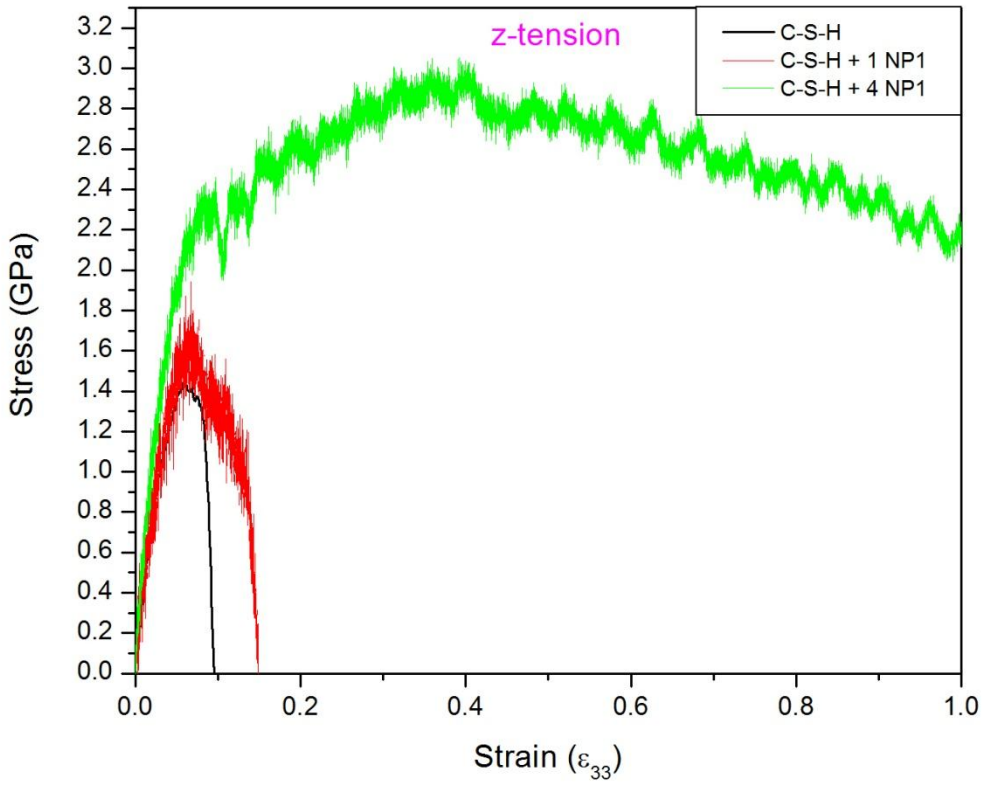

Fig.7. 4: The stress-strain curves of C-S-H, 1NP/C-S-H and 4NP/C-S-H tensioned along z axis.

7.3.2. Elastic Tensor:

According to stress-strain relationships in the elastic phase, components of the elastic tensor of 4NP/C-S-H were determined and compared with those of pure C-S-H in Table 7.1. We can see that all components of the elastic tensor are enhanced with an average of 24% indicating a stiffer composite material. The elastic tensor can be used to calculate equivalent averaged mechanical properties. The bulk modulus (K) and shear modulus (G) were calculated according to the Voigt-Reuss-Hill approximation [141]. Then, the equivalent isotropic Young's modulus (E), indentation modulus and Poisson ratio (ν) were approximated as follows:

$$E = \frac{1}{\frac{1}{3G}+\frac{1}{9K}} \quad (7.1)$$

$$\nu = \frac{1}{2}\left(1 - \frac{3G}{3K+G}\right) \quad (7.2)$$

$$M = 4G.\frac{3K+G}{3K+4G} \quad (7.3)$$

The universal elastic anisotropy index A^u, used to quantify the elastic anisotropy of the composites, is calculated from the Voigt and Reuss upper and lower bounds of bulk and shear moduli [141]:

$$A^u = 5\frac{G^V}{G^R} + \frac{K^V}{K^R} - 6 \quad (7.4)$$

Table 7.1: Elastic constants of 4NP/C-S-H and pure C-S-H.

	C-S-H	C-S-H + 4NP1	Enhancement %
C_{11} (GPa)	85.74	104.13	21.45
C_{22} (GPa)	83.18	106.39	27.90
C_{33} (GPa)	67.8	79.49	17.24
C_{12} (GPa)	45.31	55.85	23.26
C_{13} (GPa)	26.49	38.45	45.15
C_{23} (GPa)	27.01	38.84	43.80
C_{44} (GPa)	19.04	19.84	4.20
C_{55} (GPa)	18.72	23.74	26.82
C_{66} (GPa)	31.27	33.49	7.10

The calculated mechanical properties were deduced from the elastic constants in Table 7.2. All elastic properties of C-S-H were improved by the 4NP insertion. Higher bulk modulus of 4NP/C-S-H means that the composite is about 28% more resistant to uniform pressure. By comparing the Young's modulus, we can see that the composite can also withstand higher uniaxial stress for the same amount of strain, making the 4NP/C-S-H modified material 15% stiffer that pure C-S-H. The larger shear modulus indicates higher rigidity (of about 13%) compared to pure C-S-H. In addition, the enhanced indentation modulus is an indicator of higher hardness of the 4NP/C-S-H composite. The well distributed nanoparticles reduce the anisotropy of C-S-H as the universal anisotropy index [4] decreases from 0.29 for pure C-S-H to 0.23 for 4NP/C-S-H. Finally, the Poisson ratio is almost unaffected by the 4NP insertion mode.

Table 7.2 : : Bulk modulus (K), shear modulus (G), Young's modulus (E), indentation modulus (M), Universal anisotropy index (A^U) and Poisson ratio (ν) of pure C-S-H and 4NP1/ C-S-H composite.

	C-S-H	4NP1/C-S-H	Enhancement (%)
K (GPa)	47,39	60,57	27,81
G (GPa)	22,45	25,4	13,14
E (GPa)	58,16	66,84	14,92
M (GPa)	63,72	74,26	16,54
A^U	0,29	0,23	-
ν	0,3	0,32	-

7.3.3. Crack Development:

During the stretching process, structural changes can be observed as strain increases. For a better understanding of the structure strengthening by the 4NP insertion mode, we analyzed the molecular structure evolution in response to tension along the three directions.

7.3.3.1. Tension along x axis:

Fig.7.5 shows the 4NP/C-S-H tensioned along the x direction at different stages of deformation. The calcium silicate sheets take up the strain by gradually extending in the loading direction at the elastic phase. Once the yield point is reached, small voids start to show only in the interlayer region and grow while increasing strain as illustrated in Fig.7.5.b corresponding to 0.2 Å/Å strain. The appearance of voids in the interlayers corresponds to the stress drop in the stress-strain curve (Fig.7.2) after the yield point. As strain increases, calcium silicate chains are broken, cracks propagate into the calcium silicate sheets and connect together to form bigger cracks as shown in Fig.7.5.c. The rupture of the structure is slowed down by the penetration of interlayer calcium atoms (Cw) in calcium silicate sheets to bridge the broken chains. Nevertheless, the temporal reconstruction mechanism by Cw atoms doesn't stop the crack from propagating in the normal plane to the loading direction as we can see from Fig.7.5.d at 0.5 Å/Å until complete failure of the composite.

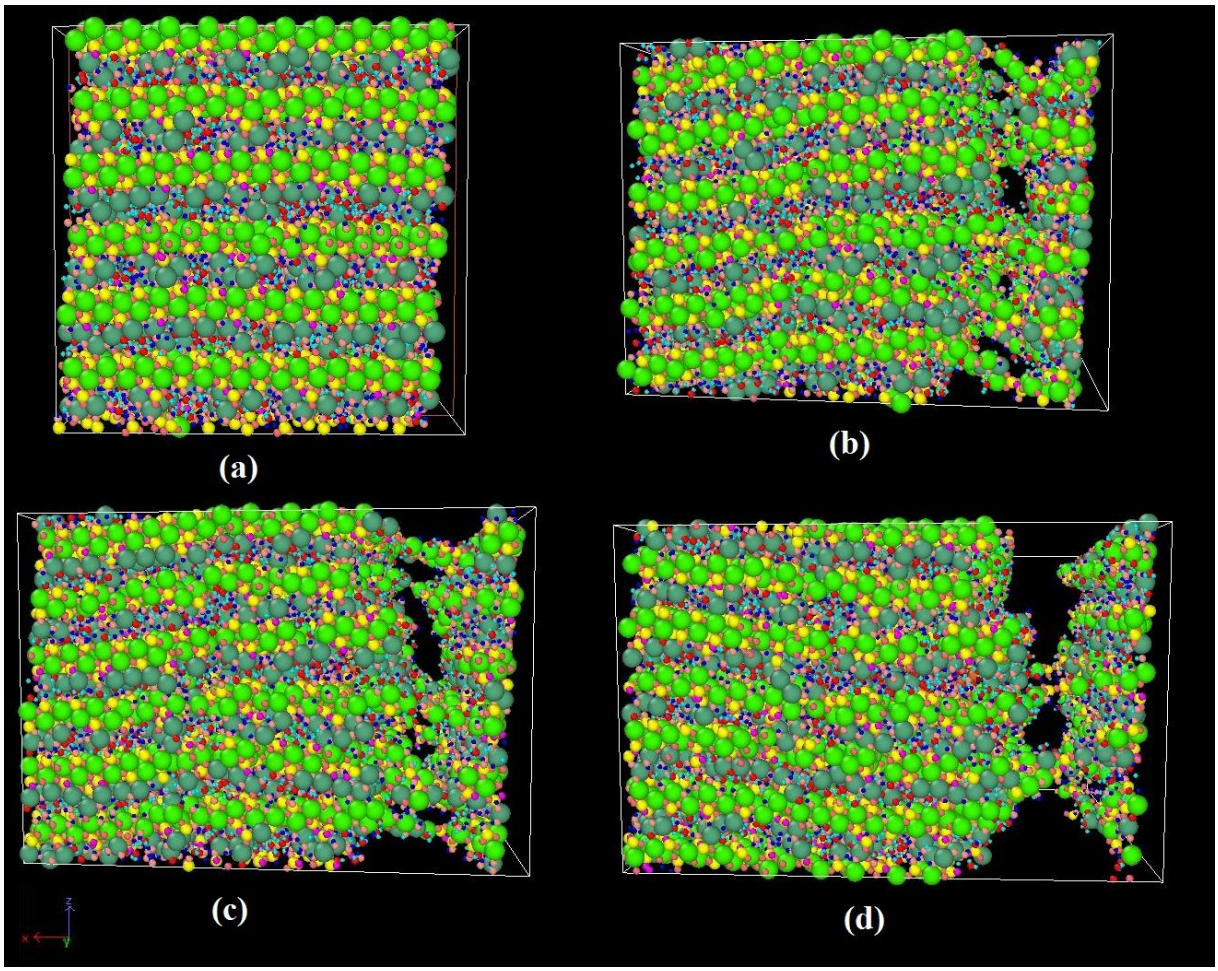

Fig.7. 5: 4NP/C-S-H structure tensioned along x axis at : (a) 0 strain, (b) 0.2 Å/Å strain, (b) 0.4 Å/Å strain and (d) 0.5 Å/Å strain.

It is important to see here that cracks are localized in a small region in x direction that first propagate in the interlayer region along y direction and then, along the z direction by breaking the calcium silicate chains as strain increases. In order to understand the role that plays the inserted nanoparticles in response to tensile loading along x axis, we have observed the (XZ) slice at the first nanoparticles level (y1=22.5 Å) at different strain stages as shown in Fig.7.6. At the beginning of the structure damage (Fig.7.6.a), voids are initiated in the interlayer region close to the composite surface. As strain increases, small cracks grow into neighboring calcium silicate sheets and coalesce to form a rupture surface that is normal to the x direction as shown in figures from Fig.7.6.b to Fig.7.6.f. The reconstruction mechanism by Cw of the broken calcium silicate sheets is demonstrated in Fig.7.6.e The rest of the structure containing nanoparticles is slightly altered. In this region, the strain is carried by the calcium silicate chains reordering and the nanoparticles stretching in the x direction as shown in Fig.7.6.f. The region is then preserved from cracking due to the nanoparticles stiffness and their strong interactions with surrounding C-S-H atoms.

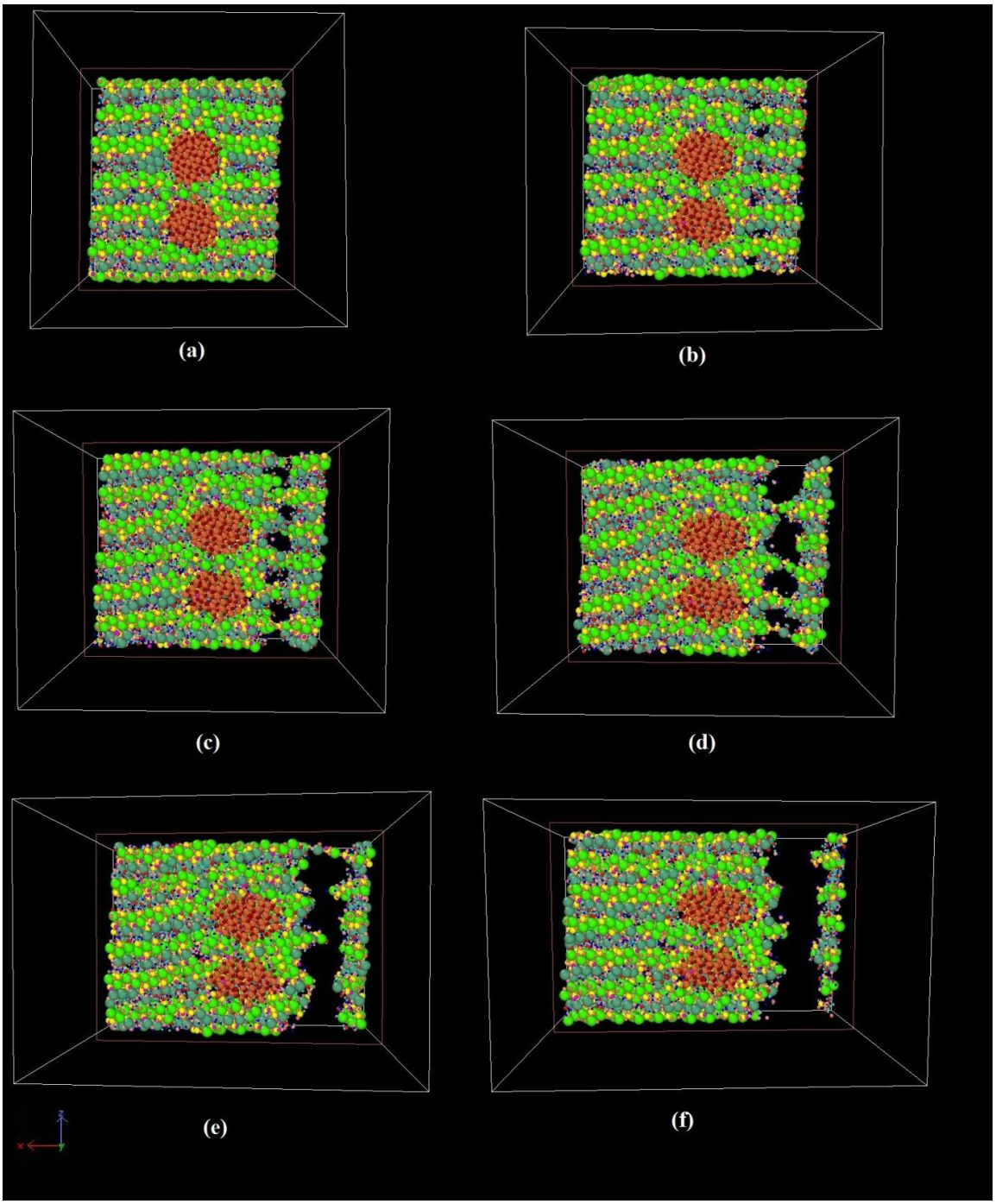

Fig.7. 6: (XZ) slice of 4NP/C-S-H tensioned along x axis at strain: (a) 0 strain, (b) 0.16 Å/Å strain, (c) 0.2 Å/Å strain, (d) 0.33 Å/Å strain, (e) 0.4 Å/Å strain, (f) 0.5 Å/Å strain.

7.3.3.2. Tension along y axis:

Fig.7.7 shows the 4NP/C-S-H at the beginning and at the end of the tensile test along y axis. We can see that the structure exhibits a necking phenomenon, which is a characteristic of ductile materials such as metals. At 1.0 Å/Å strain, the necking region occurs in two cross sections; both correspond to the nanoparticles locations. In each necking zone, the two

nanoparticles are covered by the C-S-H atoms suggesting a very strong adhesion between the nanoparticles and C-S-H matrix that exceeds the stretching work.

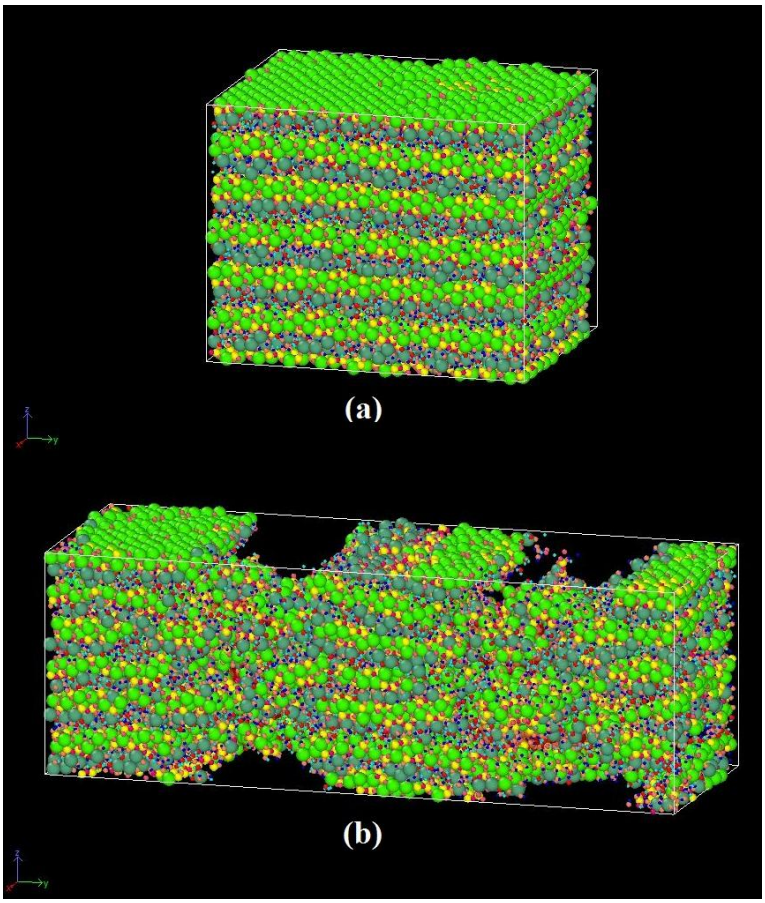

Fig.7. 7: Molecular structure of 4NP/C-S-H tensioned along y axis at: (a) 0 strain; (b) at 1.0 Å/Å strain

In order to get further insights about the structural deformation of the global system and the local nanoparticles neighboring zone, we have examined the (YZ) slice of the structure at different stages of the stretching process as shown in Fig.7.8. Soon after reaching the yield point at 0.11 Å/Å, small defects start to appear in the calcium silicate chains located away from the nanoparticles. Small symmetric voids are observed at 0.2 Å/Å strain located at the farthest calcium silicate chain from the nanoparticles (Fig.7.8.b). The stress reducing in the stress-strain curve after reaching the yield point is accompanied by the crack propagation in nearby calcium silicate sheet as we can see at 0.5 Å/Å strain. The crack growth is slowed down by the atoms rearrangement in the calcium silicate sheets and by the interlayer calcium motion that attempt to bridge the defective chains. The cracks continue to propagate along ±45° from the tension direction towards the center of the structure circumventing the nanoparticles. Finally, Fig.7.8.d shows the final tension stage corresponding to 1.0 Å/Å where

cracks are developed almost symmetrically in calcium silicate sheets to form the necking region as it was noticed before. The nanoparticles are elongated along the y direction and adopt progressively the ellipsoidal shape. The neighboring C-S-H atoms are little affected by the tensioning process as cracks are formed from the outside-in. The geometry of the central region between the two necking zones is altered and interpenetrations between calcium-silicate sheets and interlayer atoms are observed. However, the crack initiation zones and the propagation direction prevent the central calcium silicate chains from dissociation, which holds off the structure from splitting in two halves.

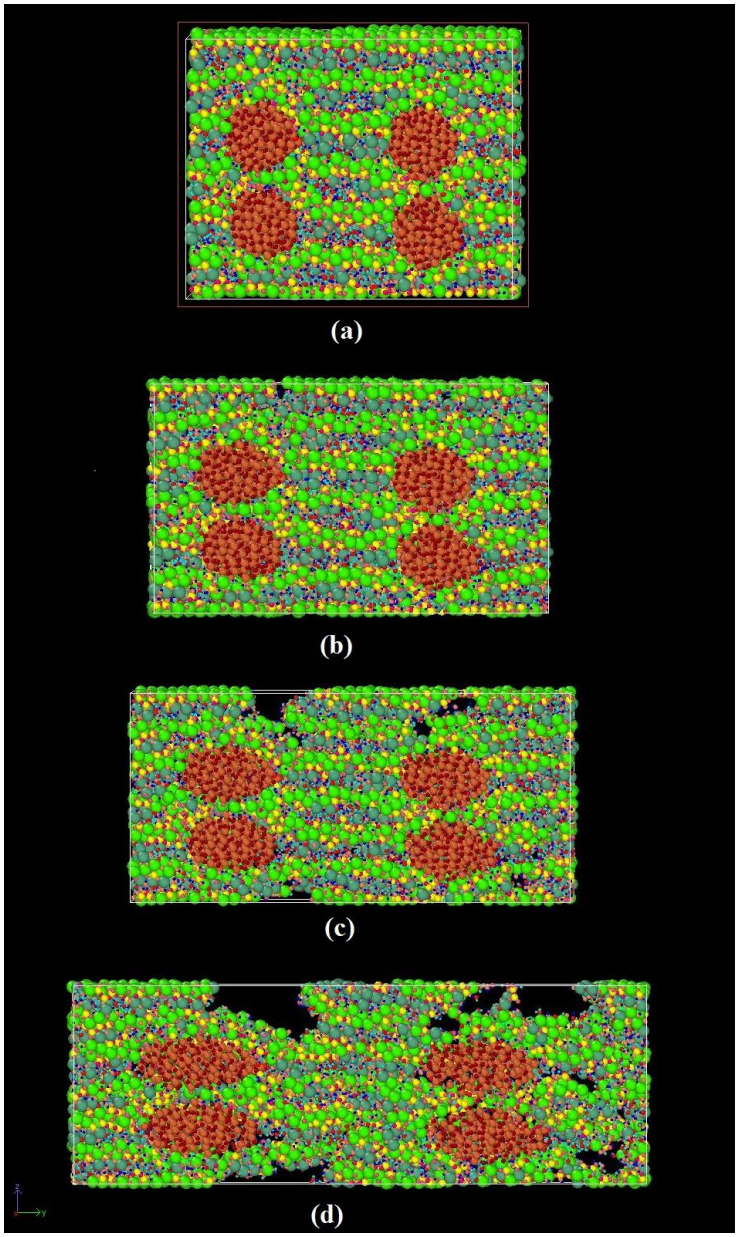

Fig.7. 8: (YZ) Slice of 4NP/C-S-H structure during the tensile along y direction at: (a) 0 strain, (b) 0.2 Å/Å strain, (c) 0.5 Å/Å strain and (d) 1.0 Å/Å strain

7.3.3.3. Tension along z axis:

The structure damage in response to tensile along z direction is quite different from tensile along x and y axes. In the short elastic phase, strain is taken up by calcium silicate chains and nanoparticles. After reaching the elastic limit, small cracks are initiated in the interlayer region as we can see from Fig.7.9.a at 0.2 Å/Å strain generating "the structure opening" at the interlayer where nanoparticles are inserted. The cracks are initiated in the interlayer region outside the nanoparticle neighboring zone as shown in Fig.7.9.a'. As strain increases, Fe ---O bonds of the nanoparticles continue to withstand the strain, resulting in a structural hardening. On the other hand, neighboring Cw---O and hydrogen bonds, with much lower ability to take strain, easily break inducing defects in the interlayer region as illustrated in Fig.7.9.b and Fig.7.9.b'. The generated crack in the two interlayers propagates and the distance in the tensile direction between the separated sheets is increased as shown in Fig.7.9.c and Fig.7.9.c'. However, the structure is held together through the nanoparticles that are tightly bound to the C-S-H neighboring atoms, which prevents the structure from rupture. At this stage of deformation, cracks are also visible in the upper interlayer that start to grow and combine together very fast; which corresponds to the stress decreasing in the stress-strain curve after 0.4 Å/Å strain. Finally, the crack propagation in the upper interlayer results in the structure rupture as illustrated in Fig.7.9.d. It should be noticed that the deformed structure doesn't exhibit a necking effect in the z direction as it was observed for tensile in the y direction. Here, the fracture surface includes also the normal region to the loading direction between nanoparticles as we can see from Fig.7.9.d'; which generates a voided defective region between the nanoparticles. In the case of loading along y direction, the normal region to loading direction between nanoparticles is not fractured, and then the pair of nanoparticles together with surrounding C-S-H atoms form the "neck region" of the final deformed structure. The observed difference is due to the composition of the normal region and to the loading direction between the nanoparticles. In the case of the y direction, this corresponds to the narrow region made of the calcium and silicate chains that strongly interact with the two nanoparticles from each side. For tensile along z axis, the normal region between the pair of nanoparticles in y direction is situated in the "weak" interlayer region where hydrogen bonds and Cw---O bonds are unstable and easy to break.

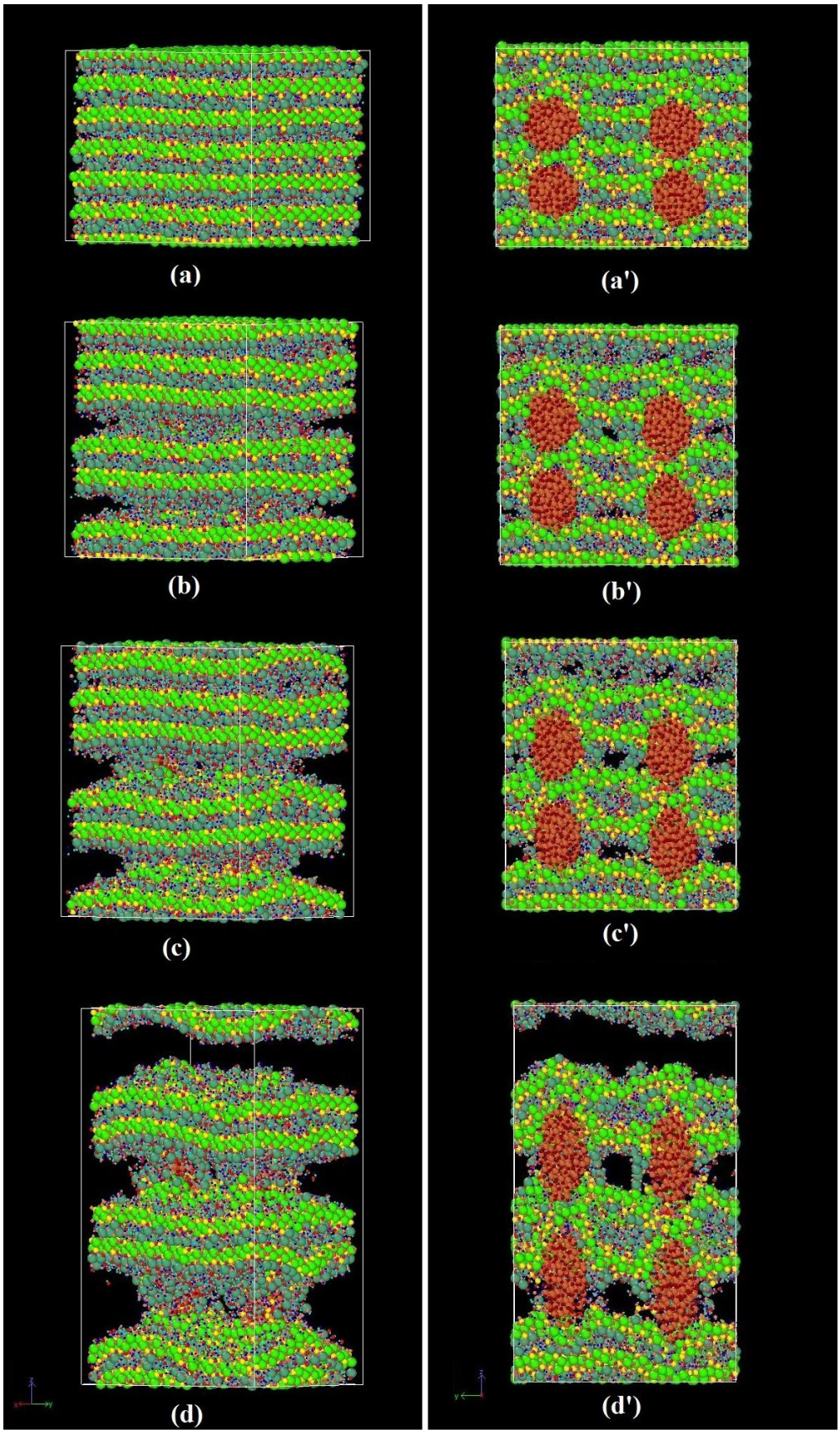

Fig.7. 9: The 4NP/C-S-H structure and the corresponding (YZ) slice tensioned along z axis at: (a) and (a') 0 strain, (b) and (b') at 0.2 Å/Å; (c) and (c') 0.4 Å/Å; (d) and (d') 1.0 Å/Å

7.4. Conclusion:

The 4NP insertion mode has an important influence on the mechanical response to tensile of modified C-S-H by Fe_2O_3 nanoparticles. Not only are the mechanical properties in the elastic phase enhanced by about 24% at average, a great ductility is also observed in the plastic phase. The tensile failure exhibits different failure modes depending on the loading direction. Most remarkably, the necking effect is observed in response to tensile along y axis which is a characteristic of ductile materials such as iron based materials. This is due to the iron oxide nanoparticles distribution in the normal plane to y axis ((XZ) plane). In each level (y_1=22.5 Å and y_2=67.5 Å), the two nanoparticles are fairly close to each other along the z axis, highly interact with each other and with the surrounding C-S-H atoms, which create a very strong region and amplifies the resistance to tensile loading. Thus, the crack propagates only outside the interaction zone "circumventing the nanoparticles". As for z axis tensile, the response is quite different, no necking effect is observed. This can be also explained by the nanoparticles distribution in the normal plane to z axis. At each z level (z_2= 19.2 Å and z_4= 43.7 Å), the two nanoparticles, with a separation distance of 24 Å along the y direction, have separate interaction zones. Moreover, the inter-region between the nanoparticles is situated in the interlayer region that is considered as the most fragile zone of the material towards tensile loading. Consequently, the cracks are initiated in the interlayer region outside each nanoparticle interaction zone and propagate along the normal plane to the loading axis. The cracks, however, cannot grow into the nanoparticles, which prevent the material from a fragile failure as it is the case for pure C-S-H. Finally, for tension along x direction, the failure surface is located close to the structure surface away from the nanoparticles influence zone. The cracks are initiated in the interlayers at the same x level, and gradually propagate into the calcium silicate sheets until complete rupture of the material. However, no crack propagation is observed in the rest of the structure. Again, this is likely due to the nanoparticles distribution. Along the x direction, the four nanoparticles are located at single x level (x_0=32.7 Å), reducing the nanoparticle strengthening region along the x direction. Thus, the farthest region from the nanoparticles quadruplet is found vulnerable towards stretching along the x axis. Subsequently, the insertion of another set of nanoparticles in a second x level may enhance the ductility of the composite along x direction and the necking phenomenon can happen in response to tensile along x direction. This analysis demonstrates that the nanoparticles distribution highly affects the ductility and the failure mode of the material.

General Conclusions

This thesis work presents a theoretical study of modified Calcium-Silicate-Hydrate (C-S-H) by Fe_2O_3 nanoparticles. The driving motivation behind this study is to harness the potential of nanotechnology approaches to develop sustainable cementitious materials with exceptional performance and novel functionalities. According to experimental studies, modification of cement based materials (cement paste, mortar, concrete…) by Fe_2O_3 nanoparticles were found to exhibit superior mechanical properties and "self-sensing" capacities. In this study, we provide an atomic scale study of nanomodified (C-S-H), the main phase of hydrated cement responsible for the strength and durability properties of cement-based materials.

In order to get more insights into the Portland cement main phases (alite and belite) that react with water to form C-S-H, we have used *ab initio* calculations in the framework of the Density Functional Theory within the pseudopotential formalism to study the structural, mechanical and electronic properties along with the reactive sites of alite and belite. First, we have investigated the ground state properties of the predominant cement phase, Tricalcium Silicate C_3S or alite [153]. The performance of the used DFT functional was tested by considering other revised versions of PBE functional. The elastic behavior of alite was characterized according to the tricilinic crystal symmetry of the material. The calculated mechanical properties were found to be in excellent agreement with the experiment and other theoretical studies. In order to characterize the reactive sites under electrophilic and nucleophilic attacks, we have analyzed the Local Density of states (LDOS) of the valence band maximum (VBM) and the conduction band minimum (CBM) using the Fukui function based on the Frontier orbital theory. Results have shown two oxygen types Os and Oc such as Os are potentially unreactive while Oc are expected to be highly reactive under electrophilic attacks, for instance H^+. Moreover, the LDOS analysis of CBM suggests that calcium atoms are susceptible to be active under nucelophilic attacks (e.g. OH- anion). Then, we have studied the second major phase of Portland cement: Dicalcium Silicate C_2S or belite using first-principle methods [183]. Two polymorphic forms were considered, the γ-belite and β-belite. By analyzing the reactive sites distribution under nucleophilic and electrophilic attacks, results showed a noticeable difference between the two belite phases regarding the reactive sites distribution. The uniformly distributed LDOS of VBM may explain the non-reactivity to water of γ-belite; while the highly located LDOS of VBM around four oxygen atoms

(between 16 atoms) indicates high reactivity areas to undergo electrophilic attacks. Our results are in agreement with the observed high water reactivity of β-belite compared to γ-belite. On the other hand, our calculations show very slight effect of the belite polymorphism on mechanical properties. In particular, the elastic behavior of γ- and β-belite shows important similarities regarding the elastic parameters obtained for the two belite phases.

Understanding the C-S-H structural features and the corresponding mechanical behavior at the nanoscale is significantly important in order to efficiently enhance its performance. Thus, we have analyzed the structural and mechanical properties of C-S-H using molecular dynamics methods [184]. The used C-S-H molecular model was based on the "realistic model" by Pellenq et al. that has proven its great capabilities to predict structural and mechanical properties of C-S-H in consistency with the experiment. The REAXFF reactive and polarizable force field was selected to allow water dissociation into hydroxyls and to account for polarization effects using a geometry-dependent charge equilibration scheme. Through analyzing the radial distribution function, we have studied the pair interactions and the coordination patterns between atoms in the interlayer and intralayer regions in order to get more insights into the complex C-S-H nanostructure. Then, elastic properties were evaluated using Stress-Strain relationship and stiffness tensor was completely determined. A particular attention was paid to the characterization of the mechanical response of C-S-H to loading by studying the elastic, plastic and failure behaviors. For the three tensile axes, initial defects are spotted in the interlayer regions. However the crack propagation is rather different depending on the axis of tensile. The cup-and-cone failure surface shows the ductile feature of C-S-H in the x and y directions while the catastrophic rupture mode confirms the brittle feature of C-S-H in the z direction.

After examining the C-S-H structure at the atomic scale, we have prepared the Fe_2O_3 nanoparticles using Electronegativity Equalization Method (EEM), annealing and relaxation techniques. The Fe_2O_3 nanoparticles were therefore inserted by gradually indenting the median C-S-H interlayer without having to change the chemical composition of C-S-H. Interactions were mainly defined through REAXFF force field for transferability issues. The obtained structure was optimized and fully relaxed until convergence was reached. The energy analysis vouches for a favorable interaction between the Fe_2O_3 inserted nanoparticle and the surrounding C-S-H matrix. Nanoparticles with different diameters ranging from 2.1 nm to 3.0 nm were selected to analyze the size effect on interactions between the inserted nanoparticles and C-S-H matrix. Results show that the smallest nanoparticle (NP1) gives the

best adhesion with C-S-H and the highest mechanical performance. Even if the ultimate strength was enhanced by 33% along the z direction via NP1 insertion-type, the calculated mechanical properties (Bulk, Young's and shear moduli) of the composites were still behind those of plain C-S-H. In this thesis part, we have only considered the size dependency of the mechanical performance of nanomodified C-S-H. The density and the way nanoparticles are dispersed in the C-S-H matrix were not taken into account. The reported reduction of the mechanical performance may be then attributed to the "non-uniform distribution" of nanoparticles inside the C-S-H matrix. The nanoparticle was inserted inside only one interlayer while the other interlayers were left non-modified. This creates a local concentration of the Fe_2O_3 nanoparticles and thus an inharmonious distribution which weakens the whole composite structure.

To examine the effect of the distribution uniformity of the inserted Fe_2O_3 nanoparticles inside C-S-H matrix, two insertion modes of nanoparticles inside the C-S-H matrix were compared in order to elucidate how nanoparticles distribution affects the mechanical response of the hybrid composite Fe_2O_3/C-S-H [185]. The structure with "well-dispersed" nanoparticles exhibits remarkable mechanical performance in both elastic and plastic regimes. Mechanical properties were enhanced with at least 24% increase compared to pure C-S-H. The strength of modified C-S-H with uniformly distributed Fe_2O_3 nanoparticles is substantially enhanced along the three directions. In the plastic phase, the "group effect" of inserted nanoparticles gives rise to higher ductility. Finally, the necking phenomenon and structural hardening were both observed in response to tensile loading, indicating a ductile failure mode of Fe_2O_3-reinforced C-S-H, and confirming the strong dependence of the mechanical behavior of nano-Fe_2O_3/C-S-H on the nanoparticles uniformity distribution.

In conclusion, this work provides an atomic scale study of the reinforcing mechanism of embedding Fe_2O_3 nanoparticles in the C-S-H matrix. A major emphasis was placed on the distribution uniformity impact on the mechanical performance of the nano-Fe_2O_3/C-S-H nanocomposite. The "group effect" of the inserted nanoparticles is a key factor for enhancing the overall ductility. The necking phenomenon may emerge as a result of the nanoparticles interconnection and their strengthening effect of the surrounded C-S-H region. Moreover, a suitable dispersion of Fe_2O_3 is required not only to enhance the linear and non-linear mechanical behavior of cement based materials, but also to develop a conductive network inside the matrix material in order to provide cement based materials with self-sensing abilities.

References

[1] USGS - Mineral Commodity Summaries 2020, page 43

[2] Feynman, R., 'There is plenty of room at the bottom', Engineering and Scienees (Feb. 1960).

[3] Taniguchi, N., 'On the basic concept of nanotechnology', Proc.Inter. Conf. on Production Engineering, Tokyo, 1974, 18-23.

[4] Drexler, K.E., 'Engines of Creation: the Coming Era of Nanotechnology' (Anchor/Doubleday, 1986).

[5]Yu, M. F., Lourie, O., Dyer, M. J., Moloni, K., Kelly, T. F., and Ruoff, R. S. (2000). "Strength and breaking mechanism of multiwalled carbon nanotubes under tensile load." Science, 287(5453), 637–640.

[6] Zhou, Z. P., et al. (2009). "Development of carbon nanofibers from aligned electrospun polyacrylonitrile nanofiber bundles and characterization of their microstructural, electrical, and mechanical properties." Polymer, 50(13), 2999–3006.

[7] Li GY, Wang PM, Zhao X. Mechanical behavior and microstructure of cement composites incorporating surface-treated multi-walled carbon nanotubes. Carbon 2005;43(6):1239–45.

[8] Cwirzen A, Habermehl-Cwirzen K, Nasibulina LI, Shandakov SD, Nasibulin AG, Kauppinen EI, et al. Cement composite In: Bittnar Z, Bartos PJM, Nemecek J, Smilauer V, Zeman J, editors. Nanotechnology in construction: proceedings of the NICOM3 (3rd international symposium on nanotechnology in construction). Prague, Czech Republic; 2009. p. 181–5.

[9] Huigang, X., Hui, L., & Jinping, O. (2003). The mechanical and pressure-sensitive properties of cement mortar with nano-particles. International Conferenee on Advances in Concrete and Structures. China. ICACS, 32(1/2), 947-953.

[10] B. J. Alder and T. E. Wainwright, J. Chern. Phys. 27, 1208 (1957)

[11] B. J. Alder and T. E. Wainwright, J. Chern. Phys. 31, 459 (1959).

[12] Van Gunsteren, W. F., & Berendsen, H. J. C. (1977). Algorithms for macromolecular dynamics and constraint dynamics. Molecular Physics, 34(5), 1311-1327.

[13] Grubmüller, H., Heller, H., Windemuth, A., & Schulten, K. (1991). Generalized Verlet algorithm for efficient molecular dynamics simulations with long-range interactions. Molecular Simulation, 6(1-3), 121-142.

[14] S. Nosé, A unified formulation of the constant temperature molecular dynamics methods, J. Chem. Phy. 81(1), 1 July. 1984.

[15] H. J. C. Berendsen, J. P. M. Postma, W. F. van Gunsteren, A. DiNola, and J. R. Haak. Molecular dynamics with coupling to an external bath. J. Chem. Phys., 81:3684, 1984.

[16] H.C. Anderson, Molecular dynamics simulations at constant pressure and/or temperature, J. Chem. Phys, 72(4), 15 Feb. 1980.

[17] Schneider and Stoll, Phys Rev B, 17, 1302 (1978).

[18] M. Parinello and A. Rahman, J. Appl. Phys 52, 7182 (1981)

[19] P. P. Ewald, The calculation of optical and electrostatic grid potential, Ann. Phys. (Leipzig) 64, 253 (1921)

[20] T. Darden, D. York and L. Pedersen, Particle mesh Ewald: An N · log(N) method for Ewald sums in large systems, J. Chem. Phys. 98, 10089 (1993).

[21] Straatsma, T. P., & McCammon, J. A. (1990). Free energy thermodynamic integrations in molecular dynamics simulations using a noniterative method to include electronic polarization. Chemical physics letters, 167(3), 252-254.

[22] Lemkul, J. A.; Huang, J.; Roux, B.; MacKerell, A. D. An Empirical Polarizable Force Field Based on the Classical Drude Oscillator Model: Development History and Recent Applications. Chem. Rev. 2016, 116, 4983−5013.

[23] Rappe, A. K., & Goddard III, W. A. (1991). Charge equilibration for molecular dynamics simulations. The Journal of Physical Chemistry, 95(8), 3358-3363.

[24]D. W. Brenner. Phys. Rev. B, 42:9485, 1990.

[25] D. W. Brenner, O. A. Shenderova, J. A. Harrison, S. J. Stuart, and S. B. Sinnot. J. Phys. Condens. Matter, 14:783, 2002.

[26] S. J. Stuart, A. B. Tutein, and J. A. Harrison. J. Chem. Phys., 112:6472, 2000.

[27]L. Liu, Y. Lu, S. V. Zybin, H. Sun, and W. A. Goddard III. J. Phys. Chem., 115:11016, 2011.

[28] Van Duin, A. C., Dasgupta, S., Lorant, F., & Goddard, W. A. (2001). ReaxFF: a reactive force field for hydrocarbons. The Journal of Physical Chemistry A, 105(41), 9396-9409.

[29] K. Chenoweth, A. C. T. van Duin, and W. A. Goddard III. J. Phys. Chem A, 112:1040, 2008

[30] TOULOUSE, Julien. Introduction to density-functional theory. 2015

[31] Hohenberg, P. and Kohn, W. Inhomogeneous electron gas. Phys. Rev., 136: B864–B871 (1964) .

[32] Kohn, W. and L. J. Sham. Self-consistent equations including exchange and correlation effects. Phys. Rev., 140:A1133–A1138, (1965).

[33] D. M. Ceperley and B. J. Alder, Phys. Rev. Lett. 45, 566 (1980)

[34] P.-F. Loos and P. M. W. Gill, WIREs Comput. Mol. Sci. 6, 410 (2016), doi: 10.1002/wcms.1257

[35] S. J. Vosko, L. Wilk and M. Nusair, Can. J. Phys. 58, 1200 (1980).

[36] J. P. Perdew and Y. Wang, Phys. Rev. B 45, 13244 (1992).

[37] J. P. Perdew, in Electronic Structure of Solids ’91 , edited by P. Ziesche and H. Eschrig (Akademie Verlag, berlin, 1991).

[38] J. P. Perdew, J. A. Chevary, S. H. Vosko, K. A. Jackson, M. R. Pederson, D. J. Singh and C. Fiolhais, Phys. Rev. B 46, 6671 (1992).

[39] K. Burke, J. P. Perdew and Y. Wang, Derivation of a generalized gradient approximation: The PW91 density functional (Plenum, NY, 1997), p. 81.

[40] J. P. Perdew, K. Burke and M. Ernzerhof, Phys. Rev. Lett. 77, 3865 (1996).

[41] P. Ziesche, S. Kurth and J. P. Perdew, Comp. Mat. Sci. 11, 122 (1998).

[42] Yin, M. T., & Cohen, M. L. (1982). Theory of ab initio pseudopotential calculations. Physical review B, 25(12), 7403.

[43] D. Vanderbilt, Phys. Rev. B 41, 7892 (1990).

[44] Blöchl, P. E. (1994). Projector augmented-wave method. Physical review B, 50(24), 17953.

[45] Taylor, H.F.W., (1997) 'Cement Chemistry', 2nd Edition, Thomas Telford, London.

[46] CEMENTS, P. Early-Age Cement Hydration Reactions. TRANSPORTATION RESEARCH RECORD, 1284, 53.

[47] M. Fukuhara et al. Mechanism and Kinetics of C4AF Hydration with Gypsum. Cement and Concrete Research, Vol. 11, 1981, pp. 407-414.

[48]. E. Andreeva and R. Sanzhaasuren. Investigation of the Processes of Chemical Interaction on Aqueous Suspensions ofTetracalcium Aluminoferrite in the Presence of Gypsum Dihydrate (English translation). Colloid Jo1mwl USSR, Vol. 39, 1977, 197-202.

[49]. J. Bensted. The Hydration of Portland Cement. In Advances in Cement Technology (S. D. Ghosh ed.), Pergamon Press, New York City, 1983, pp. 307-347

[50] Mindess S., Young J.F., and Darwin D., (2002) ' Concrete', 2nd Edition, Prentice Hall, Upper Saddle River, NJ, USA

[51] Powers T.C. and Brownyard T.L., (1948) 'Studies of the Physical Properties of Hardened Portland Cement Paste', PCA Bulletin 22.

[52] Feldman R.F. and Sereda P.J., (1970) "A new model of hydrated cement and its practical

implications," Engineering. Journal Canada 53, pp. 53-59.

[53] Wittmann, F.H., (1974) 'Bestimmung physikalischer Eigenschaften des Zementsteins', Deutscher Ausschuss fuer Stahlbeton, Heft 232, W. Ernst & Sohn, Berlin, Germany, 1-63 (in German).

[54] Tennis, P.D. and Jennings, H.M., (2000) 'A model for two types of calcium silicate hydrate in the microstructure of portland cement pastes', Cement and Concrete Research, 30(6),

855-863.

[55] Jennings, H. M., (2004) 'Colloid model of C-S-H and implications to the problem of creep and shrinkage', Materials and Structures (Special issue of Concrete Science and Engineering), Vol. 37 (265), 59-70,.

[56] Thomas, J. J., Jennings, H. M., & Allen, A. J. (1998). The surface area of cement paste as measured by neutron scattering: evidence for two CSH morphologies. Cement and Concrete Research, 28(6), 897-905.

[57] Jennings, H. M., (2000) 'A model for the microstructure of calcium silicate hydrate in cement paste', Cement and Concrete Research, 30 (1), 101-116.

[58] J.A. Gard, H.F.W. Taylor, The crystal structure of foshagite, Acta Crystallogr. 13 (1960) 785–793.

[59] Y.-S. Dai, J.E. Post, Crystal structure of hillebrandite: a natural analogue of calcium 5 silicate hydrate (CSH) phases in Portland cement, Am. Mineral., 80 (1995) 841–844.

[60] A. Alberti, E. Galli, The structure of nekoite, Ca3Si6O15·7H2O, a new type of sheet silicate, Am. Mineral. 65 (1980) 1270–1276.

[61] J.D.C. McConnell, The hydrated calcium silicates riversideite, tobermorite, and plombierite, Mineral. Mag., 30 (1954) 293–305.

[62] S. Merlino, E. Bonaccorsi, T. Armbruster, The real structures of clinotobermorite and tobermorite 9 Å: OD character, polytypes, and structural relationships, Eur. J. Mineral. 12 (2000) 411–429.

[63] Taylor, H. F. (1986). Proposed structure for calcium silicate hydrate gel. Journal of the American Ceramic Society, 69(6), 464-467.

[64] E. Bonaccorsi, S. Merlino, Modular microporous minerals: cancrinitedavyne group and C-S-H phases, Rev. Min. Geochem., 57 (2005) 241–290.

[65] Bonaccorsi, E., Merlino, S., & Taylor, H. F. W. (2004). The crystal structure of jennite, Ca9Si6O18 (OH) 6· 8H2O. Cement and Concrete Research, 34(9), 1481-1488

[66] Allen AJ, Thomas JJ, Jennings HM (2007) Composition and density of nanoscale calcium-silicate-hydrate in cement. Nat Mater 6:311–316.

[67] H.F.W. Taylor, J.W. Howison, Relationships between calcium silicates and clay minerals, Clay Miner. Bull. 3 (1956) 98–111.

[68] I.G. Richardson, Tobermorite/jennite-and tobermorite/calcium hydroxide-based models for the structure of C-S-H: applicability to hardened pastes of tricalcium silicate, beta-dicalcium silicate, Portland cement, and blends of Portland cement with blast-furnace slag, metakaolin, or silica fume, Cem. Concr. Res. 34 (2004) 1733–1777.

[69] Ayuela A, et al. (2007) Silicate chain formation in the nanostructure of cement-based materials. J Chem Phys 127:164710.

[70] Brough, A. R., Dobson, C. M., Richardson, I. G., & Groves, G. W. (1994). In situ solid-state NMR studies of Ca 3 SiO 5: hydration at room temperature and at elevated temperatures using 29 Si enrichment. Journal of Materials Science, 29(15), 3926-3940.

[71] Pellenq, R. J. M., Kushima, A., Shahsavari, R., Van Vliet, K. J., Buehler, M. J., Yip, S., & Ulm, F. J. (2009). A realistic molecular model of cement hydrates. Proceedings of the National Academy of Sciences, 106(38), 16102-16107

[72] Allen AJ, Thomas JJ, Jennings HM (2007) Composition and density of nanoscale calcium-silicate-hydrate in cement. Nat Mater 6:311–316.

[73] Bauchy, M., Qomi, M. A., Ulm, F. J., & Pellenq, R. M. (2014). Order and disorder in calcium–silicate–hydrate. The Journal of chemical physics, 140(21), 214503.

[74] Manzano, H.; Moeini, S.; Marinelli, F.; van Duin, A. C. T.; Ulm, F.-J.; Pellenq, R. J. M., Confined Water Dissociation in Microporous Defective Silicates: Mechanism, Dipole Distribution, and Impact on Substrate Properties. J. Am. Chem. Soc. 2012, 134 (4), 2208-2215

[75] Constantinides, G. (2006). Invariant mechanical properties of calcium-silicate-hydrates (CHS) in cement-based materials: instrumented nanoindentation and microporomechanical modeling (Doctoral dissertation, Massachusetts Institute of Technology).

[76] Constantinides, G., & Ulm, F. J. (2004). The effect of two types of CSH on the elasticity of cement-based materials: Results from nanoindentation and micromechanical modeling. Cement and concrete research, 34(1), 67-80.

[77] Irie, H., Sunada, K., Hashimoto, K.: Recent developments in TiO2 photocatalysis:

Novel applications to interior ecology materials and energy saving systems. Electrochem.

72(12), 807–812 (2004)

[78] Kontos, A.I., Kontos, A.G., Tsoukleris, D.S., Vlachos, G.D., Falaras, P.: Superhydrophilicity and photocatalytic property of nanocrystalline titania sol-gel films. Thin Sol.

Films 515(18), 7370–7375 (2007)

[79] Li, G.Y.: Properties of high-volume fly ash concrete incorporating nano-SiO2. Cement Concrete Res. 34(6), 1043–1049 (2004)

[80] Sobolev, K., Gutierrez, M.F.: How nanotechnology can change the concrete world. Am. Ceram. Soc. Bull. 84, 16–20 (2005)

[81] Eftekhari M, Mohammadi S. Multiscale dynamic fracture behavior of the carbon nanotube reinforced concrete under impact loading. Int J Impact Eng 2016;87:55–64

[82] Srivastava D, Wei C, Cho K. Nanomechanics of carbon nanotubes and composites. Appl Mech Rev 2003;56:215–30.

[83] Musso S, Tulliani J-M, Ferro G, Tagliaferro A. Influence of carbon nanotubes structure on the mechanical behavior of cement composites. Compos Sci Technol 2009;69(11–12):1985–90.

[84] Eftekhari M, Hatefi Ardakani S, Mohammadi S. An XFEM multiscale approach for fracture analysis of carbon nanotube reinforced concrete. Theoret Appl Fract Mech 2014;72:64–75.

[85] Veena Choudhary and Anju Gupta (August 17th 2011). Polymer/Carbon Nanotube Nanocomposites, Carbon Nanotubes - Polymer Nanocomposites, Siva Yellampalli, IntechOpen, DOI: 10.5772/18423. Available from: https://www.intechopen.com/books/carbon-nanotubes-polymer-nanocomposites/polymer-carbon-nanotube-nanocomposites

[86] Yu, M.-F., Files, B. S., Arepalli, S., & Ruoff, R. S. (2000). Tensile loading of ropes of single wall carbon nanotubes and their mechanical properties. Phys. Rev. Lett., Vol. 84, pp. 5552-5555, ISSN 0031-9007

[87] Vert, M., Doi, Y., Hellwich, K.-H., Hess, M., Hodge, P., Kubisa, P., Rinaudo, M., Schué, F., 2012. Terminology for biorelated polymers and applications (IUPAC Recommendations. Pure Appl. Chem. 84 (2012), 377–410

[88] Ruzer, L.S., 2013. Unattached fraction of radon progeny as an experimental tool in the assessment of the risk of nanoparticles. In: Ruzer, L.S., Harley, N.H. (Eds.), Aerosol Handbook: Measurement, Dosimetry, and Health Effects, second ed. CRS Press, Taylor & Francis Group, Baca Raton, FL, pp. 415–438.

[89] B.W. Jo, C.H. Kim, G.H. Tae, J.B. Park, Characteristics of cement mortar with nano-SiO2 particles, Constr. Build. Mater. 21 (2007) 1351–1355.

[90] L. Senff, D. Hotza, W.L. Repette, et al., Mortars with nano-SiO2 and micro-SiO2 investigated by experimental design, Constr. Build. Mater. 24 (2010) 1432–1437.

[91] Najigivi A, Rashid SA, Aziz FNA, Saleh MAM. Investigations on the permeability properties development of binary blended concrete with nano-SiO2 particles. J Compos Mater 2010;45(19):1931–8.

[92] Gaitero JJ, Campillo I, Guerrero A. Reduction of the calcium leaching rate of cement paste by addition of silica nanoparticles. Cem Concr Res 2008;38(8–9):1112–8.

[93] Y. Murata, H. Tawara, H. Obata, K. Takeuchi, Air purifying pavement: development of photocatalytic concrete blocks, J. Adv. Oxid. Technol. 4 (1999) 227–230.

[94] Cárdenas C, Tobón Jorge I, García C, Vila J. Functionalized building materials: photocatalytic abatement of NOx by cement pastes blended with TiO2 nanoparticles. Constr Build Mater 2012;36:820–5.

[95] Vallee F, Ruot B, Bonafous L, Guillot L, Pimpinelli N, Cassar L, et al. Cementitious materials for self-cleaning and depolluting facade surfaces. In: RILEM proceedings 2005. PRO 41 RILEM international symposium on environment-conscious materials and systems for sustainable development; 2004. p. 337–46.

[96] M. Zhang and H. Liu // Construction and BuildingMaterials 25 (2011) 608.

[97] T. Meng, Y.Yu, X. Qian, S.Zhan and K. Qian// Construction and Building Materials 29 (2012) 241.

[98] A. Nazari and S. Riah // Materials Science and EngineeringA 528 (2011) 2085.

[99] Z. Li, H. Wang, S. He, Y. Lu, M. Wang, Investigations on the preparation and mechanical properties of the nano-alumina reinforced cement composite, Mater. Lett. 60 (2006) 356–359.

[100] S. Barbhuiya, S. Mukherjee, H. Nikraz, Effects of nano-Al2O3 on early-age microstructural properties of cement paste, Constr. Build. Mater. 52 (2014) 189–193.

[101] Li, H., Xiao, H. G., Yuan, J., & Ou, J. (2004). Microstructure of cement mortar with nano-particles. Composites Part B: Engineering, 35(2), 185-189

[102] Soltanian, H., Khalokakaie, R., Ataei, M., & Kazemzadeh, E. (2015). Fe2O3 nanoparticles improve the physical properties of heavy-weight wellbore cements: A laboratory study. Journal of Natural Gas Science and Engineering, 26, 695-701.

[103] Khoshakhlagh, A., Nazari, A., & Khalaj, G. (2012). Effects of Fe2O3 nanoparticles on water permeability and strength assessments of high strength self-compacting concrete. Journal of Materials Science & Technology, 28(1), 73-82.

[104] Oltulu, M., & Şahin, R. (2011). Single and combined effects of nano-SiO2, nano-Al2O3 and nano-Fe2O3 powders on compressive strength and capillary permeability of cement mortar containing silica fume. Materials Science and Engineering: A, 528(22-23), 7012-7019.

[105] Riahi, S., & Nazari, A. (2011). Physical, mechanical and thermal properties of concrete in different curing media containing ZnO2 nanoparticles. Energy and Buildings, 43(8), 1977-1984.

[106] Nazari, A., & Riahi, S. (2012). Optimizing mechanical properties of binary blended concrete utilizing CuO nanoparticles. International Journal of Damage Mechanics, 21(1), 81-96

[107] Liu, X., Chen, L., Liu, A., & Wang, X. (2012). Effect of nano-CaCO3 on properties of cement paste. Energy Procedia, 16, 991-996.

[108] Chang T-P, Shih J-Y, Yang K-M, Hsiao T-C. Material properties of Portland cement paste with nano-montmorillonite. J Mater Sci 2007;42(17):7478–87.

[109] Kuo W-Y, Huang J-S, Lin C-H. Effects of organo-modified montmorillonite on strengths and permeability of cement mortars. Cem Concr Res 2006;36(5):886–95.

[110] Morsy MS, Aglan HA, Abd El Razek MM. Nanostructured zonolite cementitious surface compounds for thermal insulation. Construct Build Mater 2009;23(1):515–21.

[111] Li, H., Xiao, H. G., Yuan, J., & Ou, J. (2004). Microstructure of cement mortar with nano-particles. Composites Part B: Engineering, 35(2), 185-189.

[112] Liu, J., Li, Q., & Xu, S. (2015). Influence of nanoparticles on fluidity and mechanical properties of cement mortar. Construction and Building Materials, 101, 892-901.

[113] H.F.W. Taylor Cement chemistry (2nd ed.), Thomas Telford Edition, London (1997).

[114] Velez, K., Maximilien, S., Damidot, D., Fantozzi, G., Sorrentino, F. Determination by nanoindentation of elastic modulus and hardness of pure constituents of Portland cement clinker. Cem. Concr. Res., 31, 555-561 (2001).

[115] Manzano, H., Dolado, J. S., Ayuela, A., Elastic properties of the main species present in Portland cement pastes. Acta Mater., 57, 1666-1674 (2009).

[116] Tavakoli, D., Tarighat, A., Molecular dynamics study on the mechanical properties of Portland cement clinker phases. Comput. Mater. Sci., 119, 65-73 (2016).

[117] Cygan, R. T., Liang, J. J., Kalinichev, A. G., Molecular models of hydroxide, oxyhydroxide, and clay phases and the development of a general force field. J. Phys. Chem. B, 108, 1255-1266 (2004).

[118] H. Heinz, T. J. Lin, R. K. Mishra, F. S. Emami, Thermodynamically consistent force fields for the assembly of inorganic, organic, and biological nanostructures: the INTERFACE force field. Langmuir, 29, 1754-1765 (2013).

[119] R. K., Mishra, A. K. Mohamed, D. Geissbühler, H. Manzano, T. Jamil, R. Shahsavari, et al., cemff: A force field database for cementitious materials including validations, applications and opportunities. Cem. Concr. Res., 102, 68-89 (2017).

[120] Durgun, E., Manzano, H., Pellenq, R. J. M., Grossman, J. C., Understanding and controlling the reactivity of the calcium silicate phases from first principles. Chem. Mater., 24, 1262-1267 (2012).

[121] Kresse, G., Hafner, J., Ab initio molecular dynamics for liquid metals, Phys. Rev. B, 47 , 558 (1993).

[122] Kresse, G., Furthmüller, J.. Efficient iterative schemes for ab initio total-energy calculations using a plane-wave basis set. Phys. rev. B, 54, 11169 (1996).

[123] Zhang, Y., Yang, Y, W., Comment on Generalized Gradient Approximation Made Simple. Phys. Rev. Lett., 80, 890−890 (1998).

[124] Perdew, J. P., Burke, K., Ernzerhof, M., Perdew, burke, and ernzerhof reply. Phys. Rev. Lett., 80, 891 (1998).

[125] Monkhorst, H. J., Pack, J. D., Special Points for Brillouin-zone Integrations. Phys. Rev. B, 13, 5188−5192 (1976).

[126] Golovastikov, N. I., Matveeva, R. G., Belov, N. V., Crystal structure of the tricalciumsilicate 3CaO·SiO2=C3S, Sov. Phys. Crystallogr., 20, 441–445 (1975).

[127] Hammer, B. H., L. B., HANSEN, Lars Bruno, et NORSKOV, Jens Kehlet. Improved adsorption energetics within density-functional theory using revised Perdew-Burke-Ernzerhof functionals. Phys. Rev. B, 59, 7413 (1999)

[128] Y., Zhang, W., Yang, Comment on “Generalized gradient approximation made simple”. Phys. Rev. Lett., 80, 890 (1998)

[129] G., Angeles, R. N., De Vera, A. J., Cuberos, M. A., Aranda, Crystal structure of low magnesium-content alite: Application to Rietveld quantitative phase analysis. Cem. Concr. Res., 38, 1261-1269 (2008).

[130] E. Pustovgar, R. K. Mishra, M. Palacios, J. B. D. E. de Lacaillerie, T. Matschei, A. S. Andreev, et al. Influence of aluminates on the hydration kinetics of tricalcium silicate. Cem. Concr. Res., 100, 245-262 (2017).

[131] Hill, R., The elastic behaviour of a crystalline aggregate. Proc. Phys. Soc. 65, 349 (1952).

[132] Nye, J. F., Physical Properties of Crystals (Oxford: Oxford University Press) (1985).

[133] Bigare, M., Guinier, A., Mazieres, C., Regourd, M., Yannaquis, N., Eysbl, W., Woermann, E., Polymorphism of tricalcium silicate and its solid solutions. J. Am. Ceram. Soc., 50, 609-619 (1967).

[134] R. K., Mishra, R. J. Flatt, & H. Heinz, Force field for tricalcium silicate and insight into nanoscale properties: cleavage, initial hydration, and adsorption of organic molecules. J. Phys. Chem. C, 117, 10417-10432 (2013).

[135] Bader, R. F., Atoms in molecules. Acc. Chem. Res., 18, 9-15 (1985).

[136] T., Ngo, D., Schwarzenbach, Acta Crystallogr., Sect. A: Cryst. Phys., Diffr., Theor., Gen. Crystallogr., 35, 658-664 (1979)

[137] J., Lewis, D., Schwarzenbach, Acta Crystallogr., Sect. A: Cryst.Phys., Diffr., Theor., Gen. Crystallogr., 38, 733-739 (1982)

[138] H., Heinz, U. W., Suter Atomic charges for classical simulations of polar systems. J. Phys. Chem. B, 108, 18341-18352 (2004)

[139] Pauling, L., Nature of the Chemical Bond. Cornell University Press. pp. 88–107 (1960).

[140] Parr, R. G., Yang, W. Density functional approach to the frontier-electron theory of chemical reactivity. J. Am. Chem. Soc., 106, 4049-4050 (1984).

[141] S. I. Ranganathan, M. Ostoja-Starzewski, (2008). Universal elastic anisotropy index. Physical Review Letters, 101(5), 055504.

[142] A.G. De la Torre, A.J.M. Cuberos, G. Alvarez-Pinazo, A. Cuesta, M.A.G. Aranda, In situ powder diffraction study of belite sulfoaluminate clinkering, J. Synchrotron Radiat.18 (2011) 506–514.

[143] F. M. Lea, P. C. Hewlett, Lea's Chemistry of Cement and Concrete,.4th ed.; Elsevier Butterworth-Heinemann: Oxford, U.K., 1998; p 1053.

[144] Z. Mao, Z. Lu, J. Chen, B. D. Fahlman, & D. Wang, (2015). Tunable luminescent Eu 2+-doped dicalcium silicate polymorphs regulated by crystal engineering. Journal of Materials Chemistry C, 3(36), 9454-9460.

[145] J. Bensted, γ-Dicalciumsilicate and its hydraulicity, Cem. Concr. Res. 8 (1978) 73–76.

[146] P. Rejmak, J. S. Dolado, M. A. Aranda and A. Ayuela. First-Principles Calculations on Polymorphs of Dicalcium Silicate—Belite, a Main Component of Portland Cement. The Journal of Physical Chemistry C, 123(11), 6768-6777(2019).

[147] C.-J. Chan, W. M. Kriven, and J. F. Young, "Analytical Electron Microscopic Studies of Doped Dicalcium Silicates," J. Am. Ceram. Soc., 71 [9] 713–19 (1988).

[148] G.-C. Lai, T. Nojiri, and K.-I. Nakano, "Studies of the Stability of Ca2SiO4 Doped by Minor Ions," Cem. Concr. Res., 22, 743–54 (1992).

[149] K. Fukuda, H. Taguchi, Hydration of α′L- and β-dicalcium silicates with identical concentration of phosphorus oxide, Cem. Concr. Res. 29 (1999) 503–506.

[150] Y. M. Kim and S. H. Hong, (2004). Influence of minor ions on the stability and hydration rates of β-dicalcium silicate. Journal of the American Ceramic Society, 87(5), 900-905.

[151] Q. Wang, H. Manzano, Y. Guo, I. Lopez-Arbeloa, and X. Shen, (2015). Hydration Mechanism of Reactive and Passive Dicalcium Silicate Polymorphs from Molecular Simulations. The Journal of Physical Chemistry C, 119(34), 19869-19875.

[152] W. Kurdowski, Cement and Concrete Chemistry, Springer Science & Business, 2014.

[153] M. Laanaiya, A. Bouibes and A. Zaoui. Understanding why Alite is responsible of the main mechanical characteristics in Portland cement. Cement and Concrete Research, 126, 105916 (2019).

[154] J. P. Perdew, A. Ruzsinszky, G. I. Csonka, O. A. Vydrov, G. E. Scuseria, L. A. Constantin, X. Zhou, and K. Burke, Phys. Rev. Lett. (2008), 100(13):136406.

[155] D. K. Smith, A. M. A. L. Majumdar, and F. Ordway, (1965). The crystal structure of γ-dicalcium silicate. Acta Crystallographica, 18(4), 787-795.

[156] T. Tsurumi, Y. Hirano, H. Kato, T. Kamiya, M. Daimon, Crystal structure and hydration of belite Locality: synthetic Ceramic Transactions, (1994), 40, 19-25.

[157] F. Murnaghan, Proc. Nat. Acad. Sci. USA 30 (1944) 24.

[158] R. Czaya, Refinement of the Structure of γ-Ca2SiO4. Acta Crystallogr., Sect. B: Struct. Crystallogr. Cryst. Chem. 1971, B27, 848−849

[159] Z. Mao, Z. Lu, J. Chen, B. D. Fahlman, and D. Wang, (2015). Tunable luminescent Eu 2+-doped dicalcium silicate polymorphs regulated by crystal engineering. Journal of Materials Chemistry C, 3(36), 9454-9460.

[160] F. M. Lea, P. C. Hewlett, Lea's Chemistry of Cement and Concrete,.4th ed.; Elsevier Butterworth-Heinemann: Oxford, U.K., 1998; p 1053.

[161] C. M. Midgley, Acta Crystallogr 1952;5:307.

[162] F. Mouhat, and F. X. Coudert, (2014). Necessary and sufficient elastic stability conditions in various crystal systems. Physical Review B, 90(22), 224104.

[163] F. Marinelli, A. Lichanot, (2003). Elastic constants and electronic structure of alkaline-earth chalcogenides. Performances of various hamiltonians. Chemical physics letters, 367(3), 430-438.

[164] K. Velez, S. Maximilien, D. Damidot, G. Fantozzi, F. Sorrentino, Cem. Concr. Res. (2001);31:555.

[165] P. Acker, In: Ulm F-J, Bazant ZP, Wittmann FH, editors. Creep,shrinkage and durability of concrete and other quasi-brittle materials.Amsterdam: Elsevier; (2001).

[166] W. C. Olivier, GM. Pharr, J. Mater. Res. (1992);7:613.

[167] Ji Q, Pellenq RJM, Van Vliet KJ. Comparison of computational water models for simulation of calcium–silicate–hydrate. Comput Mater Sci 2012;53(1):234–40.

[168] Murray, S., Subramani, V., Selvam, R., & Hall, K. (2010). Molecular dynamics to understand the mechanical behavior of cement paste. Transportation Research Record: Journal of the Transportation Research Board, (2142), 75-82.

[169] Dingwell, D. B.; Webb, S. L. Eur. J. Mineral. 1990, 2, 427−449.

[170] Manzano, H., Pellenq, R. J., Ulm, F. J., Buehler, M. J., & van Duin, A. C. (2012). Hydration of calcium oxide surface predicted by reactive force field molecular dynamics. Langmuir, 28(9), 4187-4197.

[171] Plimpton, S. J. Comput. Phys. 1995, 117, 1−19.

[172] Manzano, H., Pellenq, R. J., Ulm, F. J., Buehler, M. J., & van Duin, A. C. (2012). Hydration of calcium oxide surface predicted by reactive force field molecular dynamics. Langmuir, 28(9), 4187-4197.

[173] Constantinides, G.; Ulm, F. J. J. Mech. Phys. Solids 2007, 55, 64−90

[174] Hou, D., Zhao, T., Wang, P., Li, Z., & Zhang, J. (2014). Molecular dynamics study on the mode I fracture of calcium silicate hydrate under tensile loading. Engineering Fracture Mechanics, 131, 557-569.

[175] M. J. A. Qomi, M. Bauchy, F.-J. Ulm, and R. J.-M. Pellenq,J. Chem. Phys.140, 054515 (2014).

[176] Qomi, M. A., Krakowiak, K. J., Bauchy, M., Stewart, K. L., Shahsavari, R., Jagannathan, D., ... & Ulm, F. J. (2014). Combinatorial molecular optimization of cement hydrates. Nature communications, 5(1), 1-10

[177] Blake, R. L., Hessevick, R. E., Zoltai, T., & Finger, L. W. (1966). Refinement of the hematite structure. American Mineralogist: Journal of Earth and Planetary Materials, 51(1-2), 123-129.

[178] Mortier, W. J., Ghosh, S. K., & Shankar, S. (1986). Electronegativity-equalization method for the calculation of atomic charges in molecules. Journal of the American Chemical Society, 108(15), 4315-4320.

[179] Aryanpour, M., van Duin, A. C., & Kubicki, J. D. (2010). Development of a reactive force field for iron− oxyhydroxide systems. The Journal of Physical Chemistry A, 114(21), 6298-6307.

[180] Rappé, A. K., Casewit, C. J., Colwell, K. S., Goddard III, W. A., & Skiff, W. M. (1992). UFF, a full periodic table force field for molecular mechanics and molecular dynamics simulations. Journal of the American chemical society, 114(25), 10024-10035.

[181] Wu, T., Wang, Q., Yu, C., & He, S. (2016). Structural and viscosity properties of CaO-SiO2-Al2O3-FeO slags based on molecular dynamic simulation. Journal of Non-Crystalline Solids, 450, 23-31.

[182] Nazari, A., Riahi, S., Riahi, S., Shamekhi, S. F., & Khademno, A. (2010). Benefits of Fe2O3 nanoparticles in concrete mixing matrix. Journal of American Science, 6(4), 102-106.

[183] M. Laanaiya, A. Bouibes and A. Zaoui: “Comparative study of Belite polymorphs and structural stability behind water reactions.” Solid States Ionics (Submitted)

[184] M. Laanaiya and A. Zaoui: “Piezoelectric response and failure behavior of cement paste under external loading.” Cement and Concrete Research (Submitted)

[185] M. Laanaiya and A. Zaoui: “Preventing concrete degradation by inserted Fe2O3 nanoparticles.” Composites Part B (Submitted)